Title
Novel Electro-textile Antenna Designs Supporting Magnetic Resonance Imaging and Communication Systems

Author
Zhang, Daisong

Publication Date
2018

Peer reviewed|Thesis/dissertation

UNIVERSITY OF CALIFORNIA

Los Angeles

Novel Electro-textile Antenna Designs Supporting Magnetic Resonance Imaging and Communication Systems

A dissertation submitted in partial satisfaction
of the requirements for the degree
Doctor of Philosophy in Electrical and Computer Engineering

by

Daisong Zhang

2018

ABSTRACT OF THE DISSERTATION

Novel Electro-textile Antenna Designs Supporting Magnetic Resonance Imaging and Communication Systems

by

Daisong Zhang
Doctor of Philosophy in Electrical and Computer Engineering
University of California, Los Angeles, 2018
Professor Yahya Rahmat-Samii, Chair

Electro-textile materials have the advantage of seamlessly integrating electronics with the human clothes and are favorable in both medical imaging and communication systems. Magnetic Resonance Imaging (MRI) is one of the most powerful imaging modality used clinically. Radio Frequency (RF) coils serving as the 'eyes' of MRI scanners to receive RF magnetic signals are the fundamental limiting factor to render high quality images. It is an increasing demand that RF coils provide more comfortable patient experience, are applied to more imaging anatomies, offer high-quality images, and decrease error rate in order to benefit patients, physicians and hospitals. The electro-textile MRI RF coil array systems are shown in the research to satisfy all the above requirements. In this research, the high strength and highly conductive electro-textiles are used to fabricate multi-layer RF coil array systems for neck imaging. The dissertation proposed and implemented a systematic approach to design, fabricate and characterize electro-textile RF coil arrays overcoming the difficulties of sensitive frequency tuning, input impedance matching, mutual coupling and the integration with the MRI scanners. The Signal to Noise Ratio (SNR) using electro-textile RF coil for both phantom and cadaver show one order of magnitude SNR improvement compared with conventional scanners. The applications

of electro-textiles are extended to antenna designs for body relevant communication systems such as Ultra-wideband (UWB) and microstrip patch antennas integrated with garments and deliver high quality communications.

The dissertation of Daisong Zhang is approved.

Sam Emaminejad

Holden H Wu

Ethan Wang

Yahya Rahmat-Samii, Committee Chair

University of California, Los Angeles

2018

To my parents

who give me love and all the best they can offer,

who support me under all circumstances, encourage me during my difficult times,

and rejoiced with me in my accomplishments

TABLE OF CONTENTS

LIST OF FIGURES

LIST OF TABLES

ACKNOWLEDGMENTS

I am sincerely grateful to Professor Ethan Wang, Prof. Holden Wu and Prof. Sam Emaminejad for their time and energy spent as part of my thesis committee. I am also forever indebted to Professor Yahya Rahmat-Samii's support, guidance, wisdom, and time given towards furthering my education and teaching me how to become a better researcher.

I would like to thank Ricardo M. Matias for the insightful discussions and help.

I would like to acknowledge and thank Professor Holden Wu, Dr. Le Zhang, and Dr. Ashley Prosper for the collaboration of MRI research, various scanning trials and clinical perspective of the acquired images. I would like to acknowledge and thank Lingnan Song from the UCLA Antenna Research, Analysis, and Measurement Laboratory for the research collaboration.

VITA

1990	Born in Pinghu, Zhejiang, China.
2012	B.S. in Electrical Engineering, University of Michigan, Ann Arbor B.S. in Electrical and Computer Engineering, Shanghai Jiao Tong University
2014	M.S. in Electrical Engineering, University of California, Los Angeles
2015-2018	Graduate Student Researcher in Antenna Research, Analysis, and Measurement Laboratory, University of California, Los Angeles
2015	National Academies of Science, Engineering and Medicine, IEEE MTT Student Design Competition 2nd Place
2016	Antenna System Design Engineer at the Apple Inc., Cupertino, CA
2017	National Academies of Science, Engineering and Medicine, IEEE AP-S/URSI - USNC-URSI Student Paper Competition Finalist
2017	National Academies of Science, Engineering and Medicine, URSI Student Paper Competition 2nd Place
2018	USPTO non-provisional patent No. 16/018,704 submitted

PUBLICATIONS

D. Zhang and Y. Rahmat-Samii, "Top-Cross-Loop Improving the Performance of the UWB Planar Monopole Antennas ," *Microwave and Optics Technology Letters*

D. Zhang and Y. Rahmat-Samii, "A Novel Flexible Electro-textile 3T MRI RF Coil Array for Stroke Prevention: Design, Characterization and Prototyping," *Transaction on Antennas and Propagation, Special issue Wireless Healthcare Biotechnology*, Nov. 2018

D. Zhang and Y. Rahmat-Samii, "Integration of Electro-textile RF coil Array with Magnetic Resonance Imaging (MRI) System: Design Strategies and Characterization Methods," *International Workshop on Antenna Technology (iWAT)*, March 5th., 2018

L. Song, **D. Zhang** and Y. Rahmat-Samii, "Towards Embroidered Textile Antenna Systematic Design and Accurate Modeling: Rectangular Patch Antenna Case Studies," *IEEE Antenna and Propagation Society International Symposium*, 2018

D. Zhang and Y. Rahmat-Samii, "Flexible RF Coil Array System Utilizing Electrotextiles for 3T MRI Carotid Artery Imaging," *IEEE Antenna and Propagation Society International Symposium*, July 12th, 2017 (accepted and selected as the Finalist for the Student Paper Competition)

D. Zhang and Y. Rahmat-Samii, "Electro-textiles as Potential Candidate of Flexible MRI RF coil for Stroke Prevention," *Proceedings of the United States National Committee of URSI National Radio Science Meeting (USNC-URSI NRSM)*, January 2017, pp. 1-2.

D. Zhang, and Y. Rahmat-Samii, "An Ergonomic Design for 3Tesla MRI Neck Coil," *Proceedings of the IEEE Antenna and Propagation Society International Symposium*, July 2016, pp. 463-464.

CHAPTER 1

Introduction

1.1 The Demands for Flexible Electronics

Since the introduction of iPhone in 2007, the smart phone has been emerging as the data acquisition and computing center in place of personal computers (PC). It is worth noting that it was not until 1995 when Windows 95 was introduced that the PCs stepped into the daily life of the general public. 10 years after the introduction of iPhone, we are at the dawn of an era for a new computing platform. It is not known whether it would be a computing device better integrated with our daily activity or a de-centralized network such as Internet of Things (IoT). It is expected, however, that the electronics will be better integrated into people's daily life and more hugely impact our life. Flexible electronics are one of the technologies needed to realize the goal. It is also desired not only for personal use, but also in medical, military, sports, and other industries where flexible electronics operate in more complex scenarios.

In the medical field, Magnetic Resonance Imaging (MRI) is an important application of flexible electronics because it has large demands in being more ergonomic and high image quality. The flexible electronics is a good candidate to meet the demand.

Other applications include Wireless Body Area Network (WBAN), personal com-

munication [5], radio frequency identification (RFID) cards [6], medical imaging [7], military positioning and combat system [8], solar cells [9] and many more. It is estimated that the flexible electronics market will be over $13.2 Billion by 2020 and over $87.2 billion by 2028 [10], with an annual compound rate of growth of 26.6%. In particular, the body-worn flexible electronics are getting increasing recognition. Design examples such as [11] [12] [13] [14] [15] is also found in the literature. They have huge potential in supporting a population with increasing life expectancy and can be used to ensure a safe and independent life style for the elders, increasing survival rates of long-term care of chronic illnesses, and expediting patient discharge after surgery. Additionally, wearable and flexible electronics have wide use for general public, athletes, soldiers and first responders such as firefighters.

Flexible electronics require collaborative efforts by researchers in many areas depending on the specific applications of interest. They include antennas, RF circuits, biosensors, biocompatible materials, integrated circuits, systems, ergonomics and many more. The fact that antenna radiation efficiency is largely dependent on its electrical size requires that antenna occupies a large portion of the area in the electronics. Many examples of designs can be found in [16] [17] [18] [19]. As a result, antennas are inherently critical components in flexible electronics that need careful study and design.

1.2 The Challenges for the Antenna Designs in MRI and Communication Systems

In this dissertation, the major focus will be put on the application of electro-textile antenna in MRI and body centric communication systems.

MRI is one of the most powerful clinically used imaging modalities. RF coil system is an integral part of the MRI scanning system used for receiving and trans-

mitting RF signals. It is a special type of antenna that collects high frequency magnetic field signals. The performance of RF coil system fundamentally limits the quality of MRI images. It is demanded that the RF coils are flexible to fit into varying curvatures of the human body and produce high quality images. Systematic design procedure is required for innovative flexible RF coil systems that meet all the requirements of the MRI scanners and overcome the difficulties such as sensitive frequency tuning, input impedance matching and mutual coupling.

In addition to MRI RF coil systems, flexible antennas designed for novel communications such as ultra-wideband (UWB) systems will also be studied. UWB systems have gained increasing interest in body-centric wireless communications due to their inherent potential of large data rates over short distance, robustness against multipath, and low probability of cross talk. The high data rate advantage lay the foundation for future data hungry applications such as imaging and video transmission. Its robustness against multipath makes it possible to support line of sight communications on body. The inherent advantage of low power spectral density and low total power makes it attractive for applications with high security requirements and high user density. Novel flexible antennas support high quality of service (QoS) when they are conformally placed on multiple locations on the human body and realize large apertures on the body wearable platform to overcome the restriction of the handheld devices. UWB antennas require low loss and linear phase over wide range of frequencies (3.1 GHz - 10.6 GHz). These specific requirements make the design of high quality textile UWB antennas challenging.

Besides the large potential for flexible antennas, many challenges shared among the above two categories are involved in designing high quality antennas. The major difficulty lies in the reliable performance in complex scenarios resulting from both human body and external environment. The antenna performance may vary in different areas of the body, with each individual and gesture (shadowing effect

for example). Other factors such as humidity and temperature change because of sweating and external environment may also influence the antenna performance. Other critical features such as lightweight, miniaturization, flexibility, low cost and high durability should also be taken into careful consideration during the design process. The combined requirements make the flexible antenna design challenging.

1.3 State of the Art Flexible Antennas in MRI and Communication Systems

1.3.1 State of the Art Flexible Materials and Technologies

The design of the flexible antenna systems starts from the selection of the materials for conductive media and the dielectric substrate. These materials are selected based on the different manufacturing technologies. They generally fall into two major categories: printing and embroidery technologies.

Printing technology recently has gained significant attention because of their potential application in areas such as large area printed pressure sensors, radio frequency identification (RFID) cards, solar cells, light emitting diodes (LED) and transistors [20]. Among them, screen printing, inkjet printing and slot die printing technologies have received the most attention because of their distinct capabilities in being simple, affordable, fast, waste effective and accurate [20] [21] [22]. Screen printing is the most popular and mature printing technology as it has been practiced in electronics industry for quite some time to print metallic interconnects on printed circuit boards. Ink-jet printing is a rapidly emerging technique that deposits solution based conducting materials for patterning [23]. In the literature many design examples using traditional printing technologies are also found in [24] [27] [29] [30].

Another type of technology is based on the embroidery method. The major

parameters of interest include the conductivity, the strength and the fitness for embroidery fabrication. As is compared in [4], silver and copper are the two major candidates with highest conductivity. However, their tensile strength are two orders of magnitude lower than other types of carbon based textiles such as Kevlar and Zylon [4]. Combining the highly conductive metals with the high strength textiles by depositing layers of conductors on the fibers is one of the most attractive methods to produce the appropriate electro-textiles for the embroidery fabrication. The electro-textiles typically used for antenna and RF applications have large variations of linear resistivity depending on the applications. In [28], Shieldex (multifilament thread 110f34 dtex 2-ply HC) with linear resistivity of 500 Ω/m was used to design RFID patch antenna for body centric applications. In [5], 332-strand silver-coated Amberstrand fibers with linear resistivity of around 3 Ω/m was used to produce multi-band body-worn antennas for GSM/PCS/WLAN communications. Both of the antennas achieve performances that satisfy the needs of the applications, therefore can potentially be used in our future research. Additionally, it is important to find the thread that is the most appropriate for embroidery fabrications. Due to the differences in diameter, the thread strength, the thread flexibility, the weight, and the filament count for each thread, the embroidered pattern may be compromised if the embroidery machine is set to fit a standard thread instead of the metallic thread available. Some commercial companies such as Brother and Husqvarna Viking have been reported to offer high performance embroidery machines that achieve high accuracy [28]. Because of the rapid development in the conductive thread industry, electro-textiles with higher conductivity, higher strength, as well as similar thickness and flexibility to the normal clothes are being invented. All these factors contribute to the better fitness of the electro-textiles to the embroidery.

Besides the metal coated electro-textiles mentioned above, several other types of textile antenna fabrication methods are also proposed. In [36], hybrid metal-fabric

antenna textiles are studied. The major disadvantage lies in the metal fatigue and rupture after repetitive bending. In [37], conductive carbon fibers as alternatives to metals were used as the conducting medium and braided with the clothes. Although enough fiber strength is reported for this fibers, the electrical conductivity is three order of magnitude lower than the metals. As a result, their applications are limited unless major improvement in conductivity is made. A third method integrated the printing technology with the textiles. In [38], ink-jet printed method is used to construct components on textiles. In [39], ink-jet printed pattern is built on top of screen-printed layers used to connect the textile and the conductive pattern. In the literature, some designs with different fabrication method and diverse applications are found in [32] [33] [34] [35]. The major disadvantage is the limited conductivity and the potential rupture after flexing and stretching due to low strength of the conductive surface. In summary, these methods lack either the durability or the conductivity and are therefore not suitable for our applications.

1.3.2 State of the Art Flexible Antennas in MRI and Communication Systems

After the selection of the appropriate conductive materials, it is critical to integrate them into the antenna designs in MRI and communication systems. Flexible MRI Radio Frequency (RF) coils have the fundamental advantage of increasing the signal to noise ratio (SNR) from the traditional coils, and as a result render higher image quality. Many trials have been made using printing technology, embroidery technology and many more. The first flexible RF coil was reported in [40] using neither printing nor embroidery technology. A mercury filled flexible coil was used to get images in region of temporomandibular joint. Despite its flexibility advantage, the mercury filled coil had the concern of usability with different scanners, long term effectiveness and stability. Although this method imposed several concerns, it may

still bring possibility to our future design using less hazardous liquid metal for improvement. In [40] and [41], flexible MRI RF coil arrays are screen printed and are reported to have similar SNR as the conventional RF coils in some areas. In [42], an MRI receiving coil is ink-jet printed directly on a flexible substrate. Some exemplary images are shown to prove its functionality. In [43], stretchable coil arrays using copper braids are proposed for knee imaging under varying flexion angles. The SNR was 20% lower than the coil arrays using traditional rigid materials. In summary, the flexible MRI RF coils reported in the literature has large room to be improved in terms of image quality, ergonomic benefit, versatility in imaging anatomies etc. Details will be talked about in Chapter 3.

Besides the MRI systems, the flexible antennas find their wide applications in communication systems. The recent electro-textile based flexible antennas are concentrated on body relevant applications and from UHF to higher end of UWB frequency bands as listed in table 1.1. The researches on the textile antennas for the communication systems are concentrated on wireless body area network (WBAN) with various types of antennas targeting different frequency bands. The frequencies as low as 860 MHz and as high as 10.6 GHz has been explored for communication applications of antenna design. It should also be noted that the electro-textile antennas for UWB applications has not been fully studied or characterized in terms of efficiency and loss. The loss caused by the surface roughness of the electro-textile antennas is critical. With the increase of frequency, the electro-textiles are more prone to performance degradation compared with conventional lithography fabrications due to the increase of electrical size of surface roughness. Patch antennas are one of the most popular types of textile antennas for communication systems due to its robustness in performance and low sensitivity to human effects. Other types of single layer textile antennas are also proposed due to their advantages such easy-to-fabricate, more flexibility and low loss, as long as the performance variation near

Table 1.1: Comparison of electro-textile antennas in frequency bands, applications, and antenna type

	Frequency Bands	Applications	Antenna Type
[44]	UWB: 3.1GHz - 10.6 GHz	WBAN	Monopole and slot
[28]	UHF: 860MHz - 960 MHz	body centric RFID	Patch
[45]	UWB: 0.6GHz - 6GHz	Body-worn communications	Slot spiral
[46]	UWB: 3.26 GHz - 4.7GHz	WBAN	SIW array
[47]	ISM: 2.39 GHZ - 2.47 GHz	Body centric communications	Dual mode circular patch
[48]	ISM: 2.38 GHz - 2.48 GHz	WBAN	SIW
[5]	GSM: 850 MHz - 900 MHz	Body-worn antenna	Loop loaded dipole

human body is well controlled and tuned. The major difficulties in the fabrication is the high accuracy. It has been improved to be similar to normal PCB fabrication accuracies [29] with the adoption of high quality electro-textiles and appropriate embroidery fabrication process. Unfortunately, this is realized by using thin metal based threads that are easy to break.

As a summary, the state of the art electro-textiles have not reached an efficient and accurate manufacture process suitable for mass production. Additionally, textile antennas still lack systematic approaches for characterization and good balance between accuracy and reliability. More efforts are needed to push the reliability and accuracy limit of the embroidery process as well as more systematic approach to characterize antenna patterns with different processes.

In summary, reasonable flexible antenna designs in both MRI and communications are found in the literature. However, the flexible MRI RF coils reported in the literature has large room to be improved in terms of image quality, ergonomic benefit, versatility in imaging anatomies etc. Details will be talked about in Chapter 3. A systematic approach for material selection and characterization, electro-textile antenna design, fabrication and measurement throughout the microwave frequencies is missing.

1.4 Achieved Objectives

This dissertation discusses the systematic design, fabrication and characterization of the electro-textile RF coil array systems for MRI scanners, electro-textile UWB and micro-strip patch antennas supporting wireless communication systems. The objective is to lay the foundations for solving the critical problems in electro-textile antennas for the afore-mentioned applications at frequencies as low as 100 MHz and as high as 10.6 GHz.

In particular, the dissertation makes the following three major contributions:

(1) Appropriately integrated electro-textiles with high accuracy fabrication processes such as computerized embroidery machine and laser cutting technology.

Several trade-offs such as conductivity, tensile strength and flexibility of the electro-textiles are considered together to find the optimum solution. In order to have a reliable process with fast design cycle, a careful selection of embroidery machine and electro-textiles guidance is provided. Some other considerations involving laser cutting and soldering are also taken into consideration and are discussed in Chapter 3 in detail.

(2) Accurately predict the performance of the electro-textile MRI RF coils and antennas through simulations and measurements.

A systematic method is developed to characterize the effective conductivity of the electro-textiles including both the conductive thread pattern and conductive cloth pattern as low as 100 MHz and as high as 10 GHz. This method is further complemented by accurately modeling the embroidered patch antenna by considering the physical structural change due to the embroidery processes.

(3) Achieved robust coil and antenna performance in constrained design requirement.

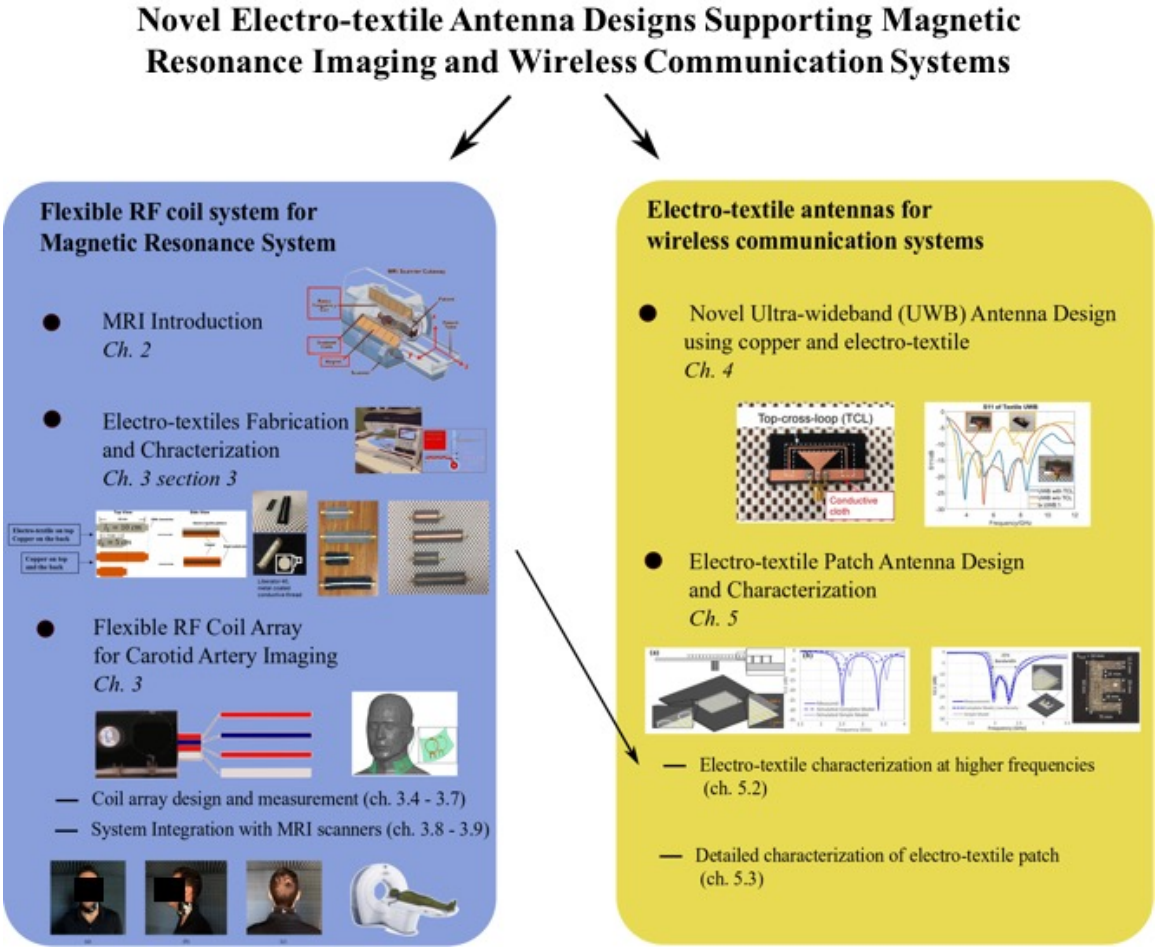

Figure 1.1: The organization of the dissertation. It should be noted that the model showing how it looks to wear the electro-textile neck coil was not scanned in the MRI scanner.

Taking RF coil for example, the accurate tuning needs to be maintained in different bending situations, and subject sizes. Additionally, the SAR needs to be satisfied for transmission RF coils. Some system level considerations involving the integration of the RF coil with scanning system such as Noise Figure (NF) and gain requirements are also taken into consideration.

The organization of the dissertation is shown in Fig. 1.1. It is split into two major areas: electro-textile RF coils supporting MRI and the electro-textile antenna designs supporting communication systems. The part of the antenna designs sup-

porting MRI is shown on the left side of Fig. 1.1. Chapter 2 briefly introduces the MRI backgrounds essential for a MRI RF coil designer. This serves as a starting point for a deeper understanding of the MRI aspect of the design and characterization process. Chapter 3 talks about the flexible RF coil array for carotid artery imaging. In this chapter, a systematic roadmap is laid out and implemented starting from the design of RF coils using lithography methods on rigid substrates, then moving towards the design of flexible MRI RF coil arrays, finally completing system integration with the MRI scanners. Deliberate considerations involving system level performances are taken from the beginning of the design process to achieve better performance than the conventional RF coils. An effective method to characterize the electro-textile effective conductivity as low as 120 MHz and as high as 10 GHz are used to facilitate the design process. This method is the foundation for the design of MRI RF coils and antennas for communication applications. The high performance RF coil is also integrated with MRI scanner after implementing effective transmission decoupling circuitry, common mode rejection device (cable trap), and pre-amplifiers. The part of the antenna designs supporting the communication systems is shown on the right side of Fig. 1.1. A novel topology of single layer UWB antenna is proposed and implemented using conventional fabrication method in Chapter 4. This design is further implemented using electro-textiles. In Chapter 5, the electro-textile characterization method proposed in Chapter 3 is extended to higher frequency range and are complemented by a more detailed model for the patch antenna. This method of accurate modeling is further utilized to design conventional microstrip patch antenna and E-shape patch antenna.

Another perspective to look at the topics of this dissertation is to observe throughout the frequency spectrum shown in Fig. 1.2. Electro-textile antennas from frequencies as low as around 120 MHz and as high as 10.6 GHz are studied. Many wide-band designs are attempted for in the literature [25] [26]. The electro-textile

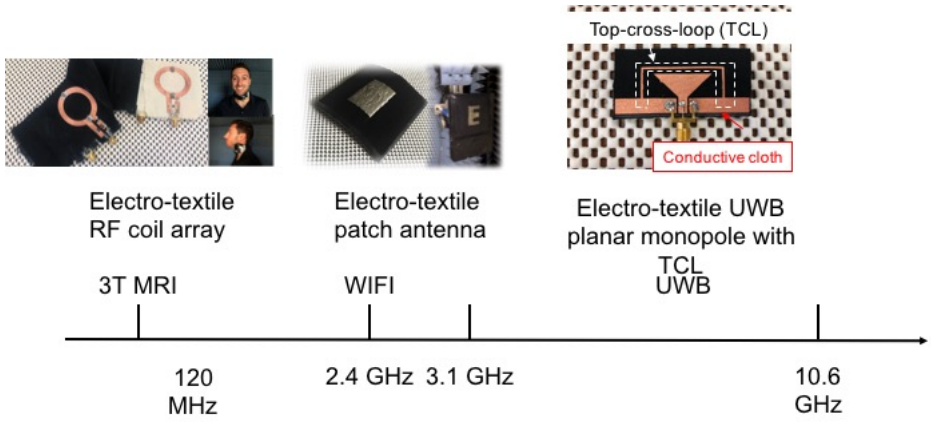

Figure 1.2: The applications of electro-textile antenna designs in this dissertation over the frequency spectrum

performance has substantial variations throughout the frequency and as a result needs to be studied across the frequency spectrum for the effectiveness of design strategies for different applications.

In summary, the goal of the dissertation of laying out the foundations for solving the critical problems in electro-textile antenna designs has been achieved. The dissertation presented a systematic approach for the design, fabrication and characterization of the electro-textile RF coil array systems for MRI, the electro-textile UWB and microstrip patch antennas.

CHAPTER 2

Introduction of Magnetic Resonance Imaging for RF coil designers

2.1 MRI basics

The primary purpose of this chapter is to provide a brief overview and background of MRI for the RF and antenna engineers. For a more complete description, please refer to [49] and [50]. An overview of electromagnetics in MRI is given in [51], and discussed in more detail in [52].

Magnetic Resonance Imaging (MRI) was developed in the 1970s, and widespread clinical use of MRI started in the 1980s. Today, more than 20,000 MRI scanners are available worldwide, and more than 70 million magnetic resonance (MR) scans are performed every year [49]. It is one of the most powerful imaging modalities. First, MRI is non-invasive, and it does not use ionizing radiation. Second, MR is capable of imaging any arbitrary scan plane or 3D volume. Last, MR offers flexible contrast mechanisms: it provides excellent differentiation between soft tissues in anatomical images, and it can also give access to biophysical and biochemical tissue properties (e.g., neuronal activity, neural connectivity, flow, diffusion).

MRI stems from the application of nuclear magnetic resonance (NMR) to radiological imaging. The adjective *magnetic* refers to the use of an assortment of magnetic fields and *resonance* refers to the need to match the (radio) frequency of

an oscillating magnetic field to the *precessional* frequency of the spin of a certain nucleus (hence the *nuclear*) of interest.

A rigorous and accurate description of the basic MR physics requires quantum mechanics; however, in most cases, a classical treatment is amply describing the macroscopic behavior. Atoms with an odd number of protons or neutrons possess a nuclear spin angular momentum, and therefore exhibit the NMR phenomenon. Qualitatively, these nuclei can be visualized as spinning charged spheres that give rise to a small magnetic moment. We will often refer to these MR-relevant nuclei as simply spins. Hydrogen with a single proton is the most abundant (the body consists largely of H_2O), the most sensitive and by far the most studied in biomedical MRI. The angular frequency of the electromagnetic fields ω_r is given by the Larmor equation 2.1

$$\omega_r = \gamma B_0, \tag{2.1}$$

where B_0 denotes the strength of the static magnetic field, and γ is known as the *gyromagnetic* ratio. For protons, $\gamma/2\pi$=42.58 MHz per Tesla. The nature of MR is based on the interaction of the spins with three types of magnetic fields: 1) main field B_0, 2) radio frequency field B_1, and 3) linear gradient fields G. An MRI scanner is shown in Fig. 2.1. The MRI scanner cutaway exhibits 1) the main magnet that produces B_0 field in z direction, 2) the radio frequency coil that produces B_1 field in xy plane typically, and 3) the gradient coils that add incremental difference in the strength of the B_0 along the z direction, with linear dependence on the x, y or z directions, to encode the spatial information into the signal received.

When the B_0 is applied to the human body, the hydrogen nucleus begin to precess along the z direction in the lab frame. In other words, the magnetization vector (M) points towards z direction. After the B_1 field is applied, the magnetization

vector is rotated from the z direction to the xy plane in the rotating frame (the frame of reference that rotate with Larmor frequency). However, after the application of the B_1 field, the M is gradually relaxed to its equilibrium position along the z direction. During this process, magnetic flux changes caused by the precessing spins induce voltage changes in receiver coils. The receive RF coils at this point are used to detect the RF magnetic signals. These magnetic signals are subsequently transformed into anatomic images. The gradient coils are critical in making this transformation step possible by encoding the spatial information into the data acquisition process. Detailed encoding process requires an understanding of the MR pulse sequence design, where the application time point, duration and waveform of the transmitted B_1 field, gradient field, and received B_1 field are carefully designed. The basic steps involve the use of B_1 and gradient fields to excite a specific imaging plane, the read out by the receive coils and repeat the process to get the data in different locations in the k space (2-D Fourier transform spatial frequency domain). The image in the spatial domain is obtained by using Fourier Transform from the data the the k-space. More details on the pulse sequence design and MR imaging from the signal processing perspective can be found in [49] and [50].

2.2 MRI aspects affecting RF coil designers

In this section, the impact of surface RF coil performance towards the SNR of the image will be studied. Surface coils are localized coils that are coupled to a limited region of the body. Although they may operate as transmit/receive coils, they are often used in receive mode only owing to their highly nonuniform B_1 distribution. Surface coils are appropriate for imaging superficial structures such as eyes, spine, extremities and carotid arteries. Compared to using a head coil or body coil as the receiver coil, surface coils achieve a better SNR in superficial regions because

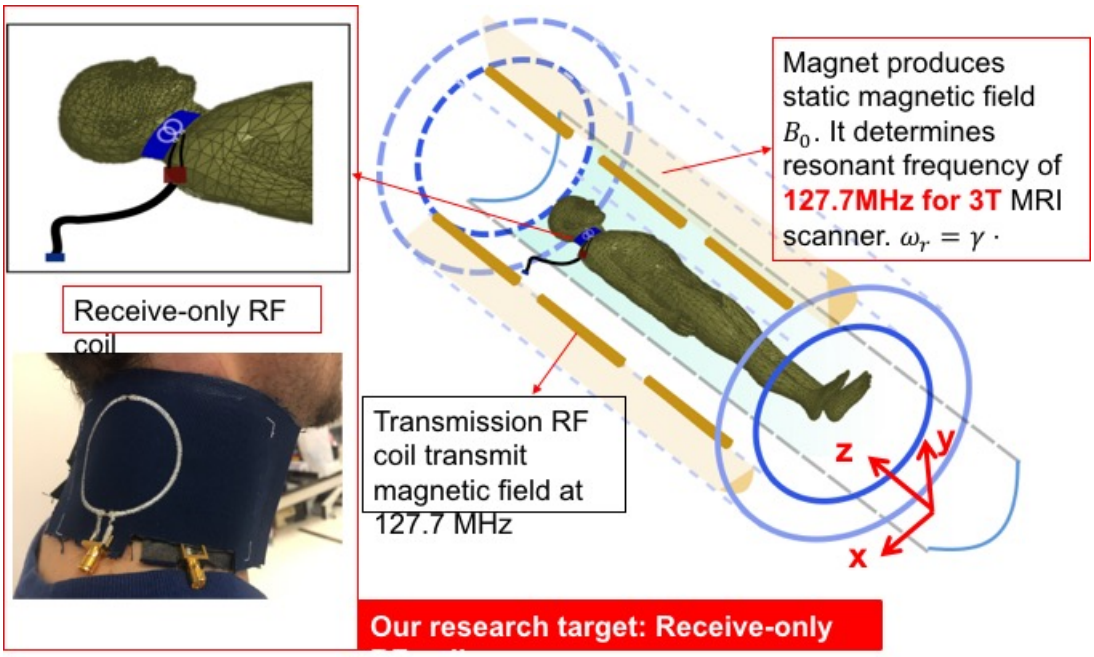

Figure 2.1: 3T MRI scanner is shown. After the patients lie on top of the MRI bench, technician puts RF coil around the patient's neck. Uncomfortable RF coils use heavy and rigid material around the neck. Patients move due to low comfort level. This may lead to low image quality and increase clinic time. The MRI scanner cutaway exhibits 1) the main magnet that produces B_0 field in z direction, 2) the radio frequency coil that produces B_1 field in xy plane typically, and 3) the gradient coils to encode the spatial information.

of a higher image-volume to noise-volume ration. However, simple single-element surface coils are less suitable for imaging deep-lying structures because of the falloff of sensitivity with depth. For a circular surface coil of radius a situated at x=0, the B_1 sensitivity of the RF field a distance x along the main axis away from the coil is

$$B_1(x, a) \propto \frac{a^2}{(a^2 + x^2)^{3/2}}; \tag{2.2}$$

For x=a, the B_1 sensitivity falls off by a factor of 0.35 relative to its sensitivity at x=0. A detailed discussion on the surface coil technology is given by [53]. While a single surface coil provides higher SNR in a localized region, surface coil arrays are commonly used because they extend the available Field of View (FOV) while

retaining the high SNR advantages [54]. Coil arrays are also useful for scan acceleration. Simplistically, imaging with each coil in the array requires fewer phase encodes because of the smaller FOV seen by the coil. The full-FOV image can be pieced together through appropriate processing of the outputs from the individual coils in the array.

It is discussed above that the SNR advantage of the surface coil array makes it the dominant type of RF receiving coil. It is therefore important to characterize how the RF coils affect the SNR of an image. The performance of a coil can be predicted using Equation 3.4, where SNR_0 is the total available (or intrinsic) SNR described in [55]

$$SNR = SNR_0\sqrt{1 - \frac{Q_{loaded}}{Q_{unloaded}}} \tag{2.3}$$

The noise of the RF coil arrays come from two sources: the human body and the imperfect conductivity of the material used. The common parameter of interest is the ratio between the unloaded and the loaded quality factor,

$$Ratio_{quality factors} = \frac{Q_{unloaded}}{Q_{loaded}}, \tag{2.4}$$

A quick rule of thumb for a quick estimate is whether the Q ratio of over 5. When the quality factors ratio is 5, the SNR=0.9 SNR_0. However, the contribution to the loss from the two sources varies with different coil diameters and frequencies as shown in [41]. In practice, it is usually time consuming and inaccurate to measure the loaded quality factor. In [56], a practical method is introduced to quickly measure the loaded and unloaded quality factors ratio without directly measuring the loaded quality factor. This method can be used in the characterization of the coils to be

discussed in Chapter 3;

CHAPTER 3

Flexible MRI RF Coil Array for Carotid Artery Imaging

In this chapter, we will talk about the flexible MRI RF coil array design for carotid artery imaging. We proposed and implemented a systematic roadmap to design the flexible RF coil array. We will also talk about the major difficulties involved in the design of electro-textile RF coil array and the strategies to solve them. Several design examples and their performances will be presented.

3.1 Motivations and challenges

In U.S. stroke happens around every 40 seconds and someone dies of stroke every four minutes. Stroke is the No. 5 cause of death in the United States, killing nearly 130,000 people a year (128,978). That is one in every 20 deaths [57]. Among these stroke cases, one out of four is related to carotid artery diseases [58]. Carotid arteries are two major vessels near neck. Pieces of plaque can break free, travel to the brain, and block blood vessels in the brain, neck and face shown in 3.1. Patients with substantial carotid narrowing are at large risk for a major stroke, however, the degree of stenosis alone is a relatively poor prediction of neurological events [59]. The clinical standard for measuring disease severity is the overall luminal stenosis, which is not enough for accurate prediction. The carotid artery provides an excellent location for imaging arterial plaques and the study of disease progression [59]. Mag-

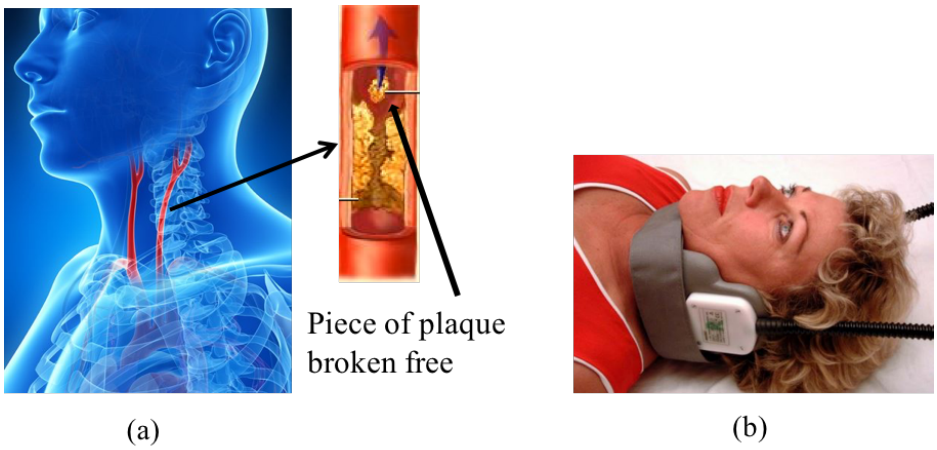

Figure 3.1: (a) The carotid arteries are the two major vessel near neck. Pieces of plaque can break free, travel to the brain, and block blood vessel that supply blood to the brain (figure from [1]). (b) Uncomfortable RF coils use rigid material near neck. Patients move due to low comfort level. This may lead to low image quality and increase clinic time (figure from [2]).

netic Resonance Imaging (MRI) of the carotid arteries are not only critical clinically, but also important for the research of the "vulnerable plaque" mechanisms. As a result, a reliable in vivo image method monitoring the components of the plaques is needed. The RF coil is the fundamental limiting factor for a high performance image that provide both high Signal to Noise Ratio (SNR), high resolution and additional information about the plaque components.

Radio Frequency (RF) coils are integral part of the MRI scanners for transmission and reception of RF magnetic signals. When the imaging area is not the entire human body, surface RF coils are preferably used due to its advantageous signal to noise ratio (SNR). They spatially reject noise from parts of the human body that are not imaged and as a result inherently have higher SNR than whole body coils. Current RF coils however have the disadvantage of not being comfortable to wear. Due to the comparatively long imaging time needed for MRI than other imaging modalities, this disadvantage may consequently lead to other problems such as repetitive imaging trials, MRI image motion artifact etc. Additionally, the high

curvature of the neck area makes it hard to place the RF coils near it. As a result, flexible MRI RF coils are desired.

Flexible RF coils not only are more ergonomic but also bring another chance to increase SNR, which is a fundamental limiting factor of MRI image quality. The SNR of surface RF coils is very sensitive to the placement of the coil relative to the tissue for imaging. When the coil is placed near the tissue, an increase in signal sensitivity is expected . The noises in MRI come from two different sources: human tissue and coils along with its relevant circuitry. For most clinical applications of RF surface coils, noises from human tissue is much larger or at least comparable to those from coils and circuitry. This observation brings an opportunity to the various materials to be used in flexible MRI RF coils. A slight increase in losses by coils and circuitry is offset by the advantage of ergonomic consideration and potential higher SNR of flexible RF surface coils. Flexible MRI RF coils were studied using screen printing in [41], ink-jet printing in [42] and copper braid in [60]. The substrate of the first two methods has limited flexibility compared with normal clothes. Additionally the second method is limited by the thickness of the conductor it can print. As a result its conductivity is limited at interested frequencies. The third method uses meandered copper braid and as a result may be worn out over the time. In this chapter electro-textiles are explored and used to buid flexible MRI RF coils. Electro-textiles have the advantages of being highly conductive, as flexible as normal cloth and also enduring over the time.

Several challenges need to be overcome to design high quality electro-textile flexible RF coils. First of all the current literature lacks a systematic approach to design MRI RF electro-textile RF coils. Secondly the combined subtleness of the electro-textiles and the high accuracy requirement for the resonant tuning makes it difficult to get high SNR in the specified 127.7 MHz near human body for 3T MRI scanners. Thirdly, the trade off between the coverage area and the single coil SNR

performance requires the use of RF coil array. Some specific difficulties are involved in the design of RF coil array system. They include the minimization of the mutual coupling between different coil elements, the integration of the coil elements into the multi-layer coil array and the system integration between the RF coils and the MRI scanner.

In our work, the systematic steps are proposed to explore the potential of electro-textiles for MRI RF coils. We will start with the design and analysis of RF coil using rigid materials, then proceed to the single coil element with electro-textiles, and finally come to the multi-layer RF coil array using electro-textiles and resonant at exactly 127.7 MHz near the human neck.

3.2 Roadmap of MRI RF Coil Array Design

An innovative 3-step systematic approach is proposed for the coil array design in this paper. The major design challenges lie in the collective subtleness of different parameters for resonant tuning and impedance matching in both the coil element and the coil array design. The roadmap of the RF coil array system design is divided into 3 steps shown in Fig. 3.2: In step 1, the coil element using normal lithography etching methods is designed and serves as a reference for later prototypes; In step 2, electro-textiles are utilized to design the coil element; In step 3, the coil array with the electro-textiles is designed.

3.3 Fabrication and characterization of electro-textiles

3.3.1 Conductive textile threads

Conductive textile threads used for the MRI RF coil arrays are the metal coated textiles to achieve a balance between conductivity, tensile strength, and flexibility,

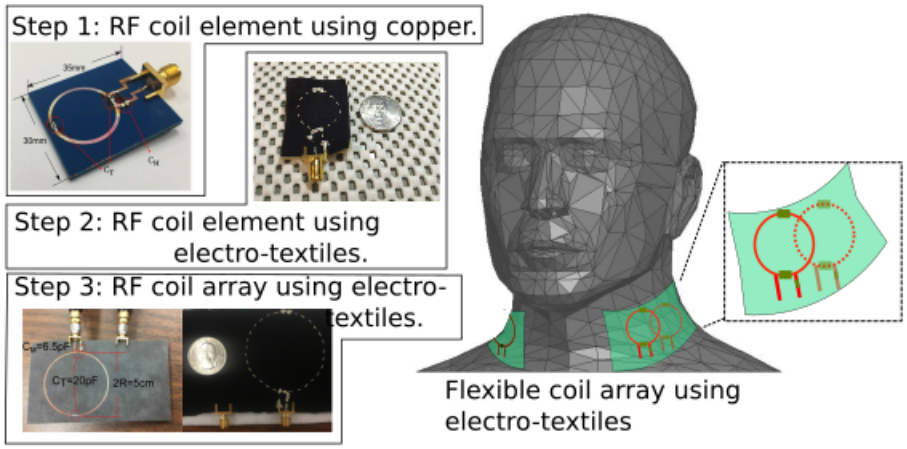

Figure 3.2: The roadmap to design RF coil array system using electro-textiles. Two coil elements are positioned in the front and back of the supporting layer.

which was discussed in Chapter 1. An illustrative micro-scale electro-textile is shown in the Fig. 3.3 and the Fig. 3.4. Two kinds of electro-textiles used include Shieldex 110f34 dtex 2-ply HC found in and Liberator 40. Shieldex thread is created from two strands of raw yarn initially used by [28] for UHF RFID. Two of its major advantages are the appropriate diameter and flexibility. It has the diameter of 0.2mm, which is very similar to the standard cotton based threads used for embroidery machines. Because of the fact the core of the thread is Nylon, the flexibility of the thread is close to a standard thread nylon based threads, making it suitable for embroidery machine integration. Despite the diameter and the flexibility advantage, the major disadvantage is the conductivity. As will be talked about in 3.5, the high and varied DC linear resistivity of 500 $\Omega/m \pm 100\ \Omega/m$ leads to difficulty in impedance matching and resonant tuning, as well as the quality factor performances. The second type of electro-textile used is the Liberator 20 and Liberator 40 made of 40 filaments of Kururay Vectran fiber coated with 3 μm silver or copper layers in [61] used in [4]. The big advantage of good balance between conductivity, tensile strength, diameter and flexibility allowed us to build high quality electro-textile antennas and was widely used in the later designs. The DC linear resistivity is 3

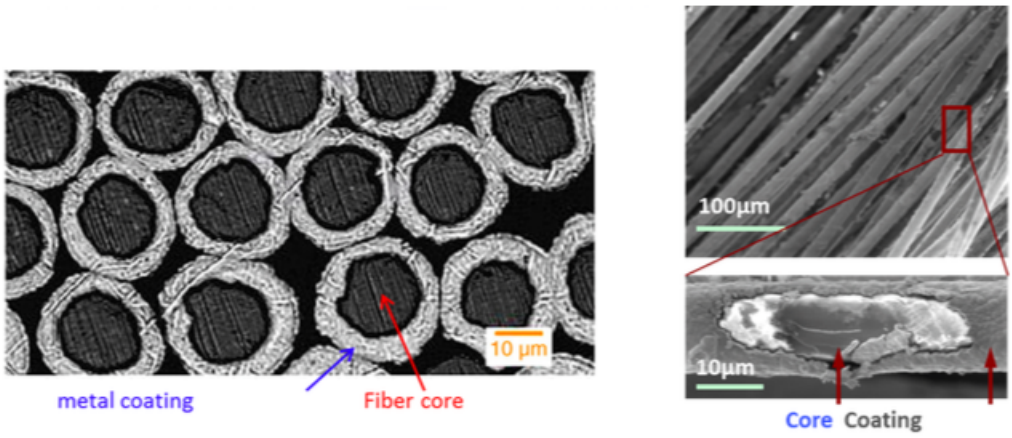

Figure 3.3: The illustrative micro-scale image of the electro-textile from [3]

Ω/m with diameter of around 0.5mm. The polymer based Vectran fiber has a large tensile strength of 3 GPa, more than four times the strength of Nylon. Although its flexibility is not as high as the Shieldex, its high tensile strength makes it less vulnerable to be broken than the other electro-textiles.

3.3.2 Characterization of electro-textiles

The details to characterize the effective conductivity of the embroidered pattern will be discussed in detail in Section 3.4. The current electro-textile RF coils are constructed using the single thread, instead of the embroidered patterns. For the cases of single thread characterization, effective conductivity is no longer useful. We instead adopt the linear conductivity of the conductive thread to estimate the effective resistance and optimize our design in Advanced Design System (ADS). The other performances can further be predicted in High Frequency Simulation System (HFSS) using the equivalent conductor width of the conductive material. We will talk about it in more detail in Section 3.5.

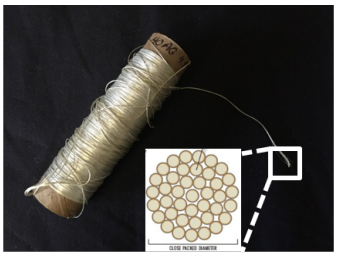

Liberator 40, metal coated conductive thread

Shieldex 235-34, silver coated thread

Figure 3.4: Liberator 40 and Shieldex are both electro-textiles. Liberator 40 is used in this project due to its excellent performance in conductivity and tensile strength.

3.4 Electro-textile characterization

It is critical that electro-textiles are characterized and the performance is accurately predicted using software simulation tools. Several researchers have made efforts in characterizing electro-textile patterns or threads using effective conductivities (different definitions for different papers) and surface resistance. In [4] a microstrip line based method to get effective conductivity at 0 - 6 GHz was proposed, where the surface roughness is taken into consideration. Although this method include the frequency from very low to 6GHz, the major applications are focused on lower GHz range. The surface roughness factor was taken under the assumption that the surface roughness is much larger than the skin depth, which may no longer hold for low frequency applications such as MRI at 3 Tesla (3T). The second disadvantage is that the loss in theory is lower in lower frequencies than the higher frequencies and bring more error using this method. [62] combined the strip line and Method of

Moment (MOM) method to get the effective conductivities for different stitch types and embroidery methods. However this method was limited to the single thread property characterization in RF frequencies. Additionally it had the difficulty to model dimensionally small conductor undulation for MOM simulation. In [36], a systematic method to characterize the electrical properties of electro-textiles at high frequency is applied using both the waveguide cavity method and the microstrip resonator method. This method is effective in high frequency applications but not as convenient for the low frequency application such as MRI because the size of the cavity and resonator may be really big in around 127 MHz range. In [28], an experimental method was proposed to get the complex sheet impedance that has both resistive and reactive part. This method is effective for the RFID development. However its biggest advantage was that it took several iterations to get the accurate values of sheet impedance and was time consuming. Since these electrical properties depends on the stitch strategies, stitch densities, type of pattern and type of electro-textiles, it is critical that we have rapid characterization methods. Although, the above characterization methods are effective in some applications, there is a missing part in characterizing the electrical properties of both the single thread and the electro-textile pattern.

Here we propose a modified method to get the effective conductivity of the electro-textile antenna pattern based on the method proposed in [4]. The major steps and equations are included in Fig. 3.5. In step one, microstrip lines with different length fabricated with the copper and the electro-textiles are constructed. In step two, the total attenuation constant of these microstrip lines are calculated based on the measured S_{21}. It is noted that the S_{21} information is de-embedded from the loss and perturbation of the connectors using S-matrix or ABCD matrix de-embedding methods in [4] and [63]. In step three, the conductivity attenuation constant of the electro-textile patterns are separated from the the dielectric and the

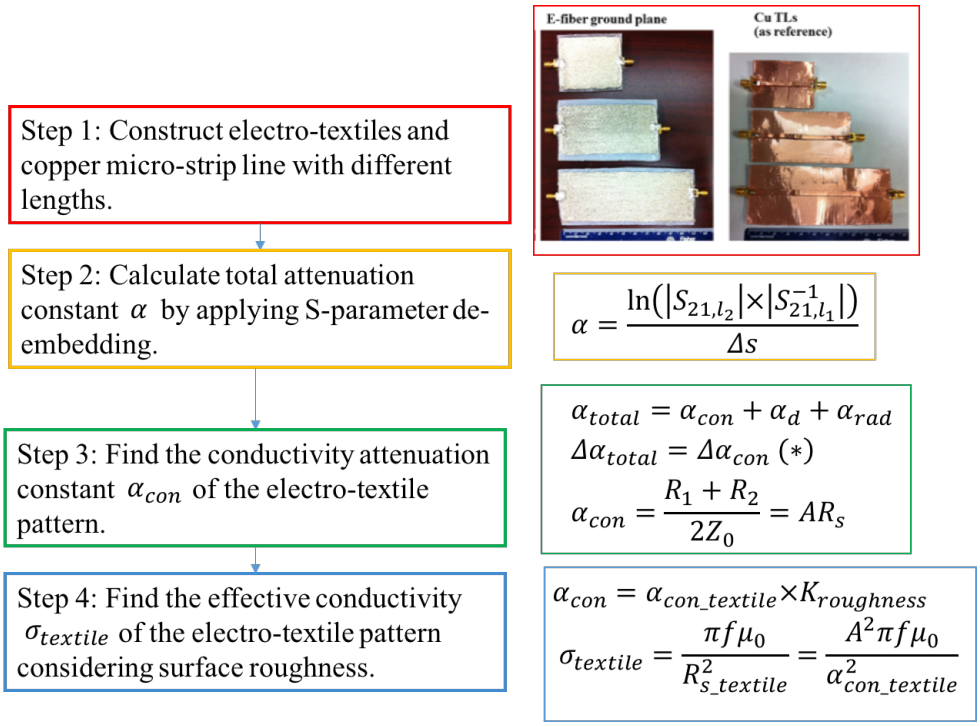

Figure 3.5: The steps to get the effective conductivities of the electro-textile patterns using microstrip line method

radiation losses. In the step four, the effective conductivity is extracted considering the surface roughness. The effective conductive loss that accounts for the loss due to surface roughness is used. The surface roughness constant $K_{roughness}$ is used in Eq. 3.1 and Eq. 3.2 from [64] and [65] to relate the effective attenuation constant and the ordinary attenuation constant derived based on "smooth" metallic surface.

$$\alpha_{cond-eff} = \alpha_{cond} \times K_{roughness} \tag{3.1}$$

where $\alpha_{cond-eff}$ is the effective conductivity, α_{cond} is the ordinary conductivity, and $K_{roughness}$ is the surface roughness constant. The surface roughness constant is

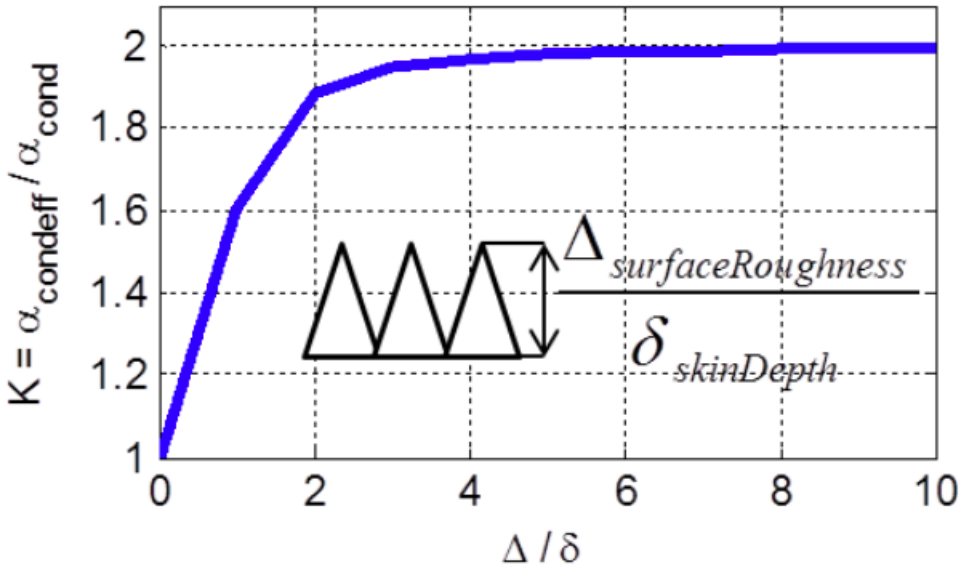

Figure 3.6: K factor as a function of surface roughness from [4]

calculated in Eq. 3.2:

$$K_{roughness} = 1 + \frac{2}{\pi} tan^{-1}(1.4 \frac{\Delta_{surface\ roughness}}{\delta skin\ depth}) \tag{3.2}$$

where $\Delta_{surface\ roughness}$ is the height of the rough surface triangle from the bottom to the top shown 3.6. The surface roughness constant $K_{roughness}$ is plotted in3.6 based on the Eq. 3.2. It can be observed that when the surface roughness is greater than 6, the $K_{roughness}$ begins to be plateau. In [4], surface roughness constant $K_{roughness}$=2 is used considering the large surface roughness compared with the skin depth. In our application, this assumption may no longer hold because of the skin depth increase at the lower frequency. At the frequency of 127 MHz, the skin depth of the copper is around 6 μm, in order for the K factor to be 2, the surface roughness needs to be greater than 36 μm, which is not always the case for the electro-textile pattern especially when the stitch density is high.

More measurements are needed to determine an accurate effective conductivity

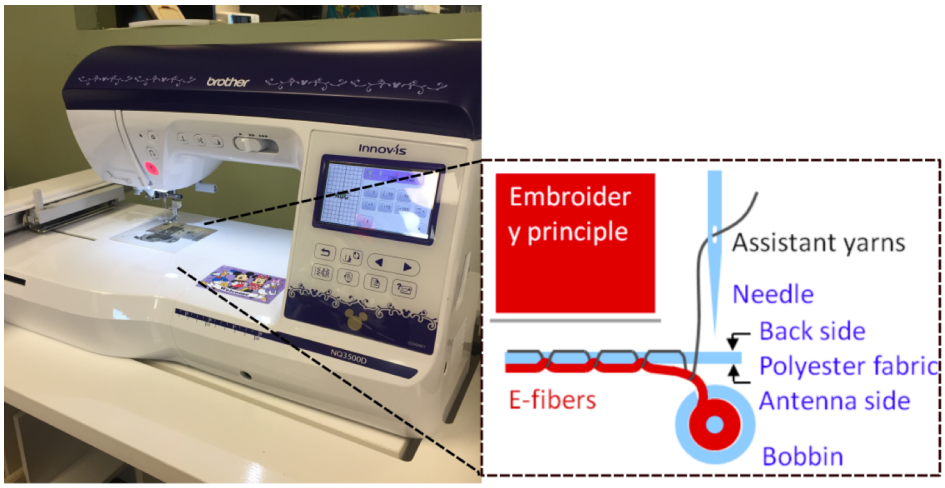

Figure 3.7: The embroidery machine Brother NQ1400 is shown above with embroidery size of 6"×10". The close up shows that the electro-textile is used as the bobbin thread and the normal thread goes through the assistant needle to help the embroidery process.

prediction model according to different stitching strategies, stitching densities, and the kinds of the electro-textiles used. This method will be used in our future research to explore high performance RF coils and the UWB antennas.

Additionally, the embroidery machine needs to be chosen with care. An photo and its close-up figure showing its working mechanism is in the Fig. 3.7. The embroidery machine Brother NQ1400 is shown above with embroidery size of 6"×10". The close up shows that the electro-textile is used as the bobbin thread and the normal thread goes through the assistant needle to help the embroidery process.

3.5 Design of single element MRI RF coils

3.5.1 RF coil element using rigid materials

Single loop coil is fundamental for the study of electro-textile material potential for RF coils. Our proposed RF coil is designed to operate efficiently at the frequency of 127.74MHz for 3T MRI systems. The proposed coil can be used in transmit/receive

Table 3.1: The design parameters of the single element RF coil with FR4 as substrate

Parameter	substrate width, W	substrate length, L	Loop radius, r
Value	30 mm	35 mm	10 mm
Parameter	Loop width, d	C_T	C_M
Value	1 mm	83.5 pF	7 pF

coil systems. It can evolve in subsequent steps as receiving only coil and coil arrays as described in 3.2. Position of the proposed RF coil relative to human neck and its design parameters are shown in Fig. 3.9. The values of the parameters in Fig. 3.9 including tuning capacitors are listed in Table 3.1. The RF coil is placed 10mm away from human neck. The coil is connected to edge mount SMA connector with 50Ω. The proposed coil shown in Fig. 3 is fabricated with photolithography on FR4 substrate with $\epsilon_r = 4.4$, $\tan\sigma = 0.02$ and thickness of 0.4mm.

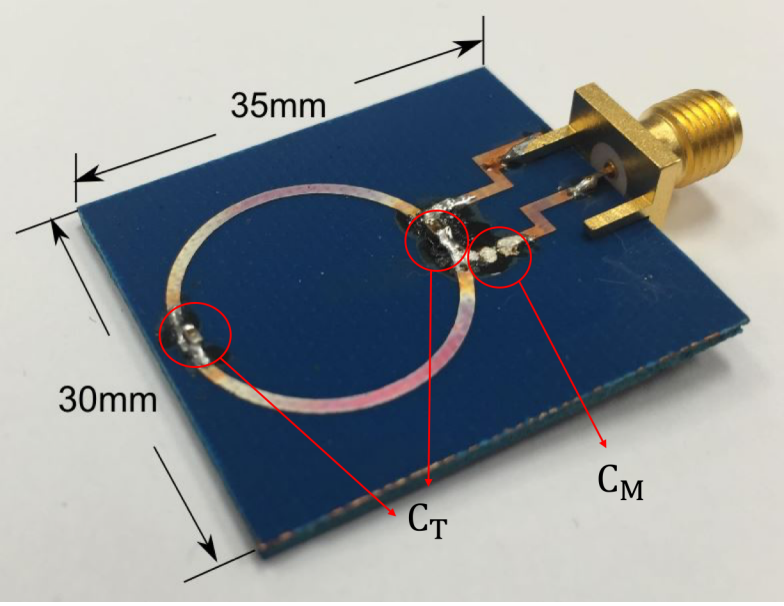

Figure 3.8: The fabricated neck RF coil with resonant frequency at 127.7MHz.

One critical procedure for coil analysis is to evaluate its performance near human body. In [51] the interaction of RF fields with human body is reviewed. In recent

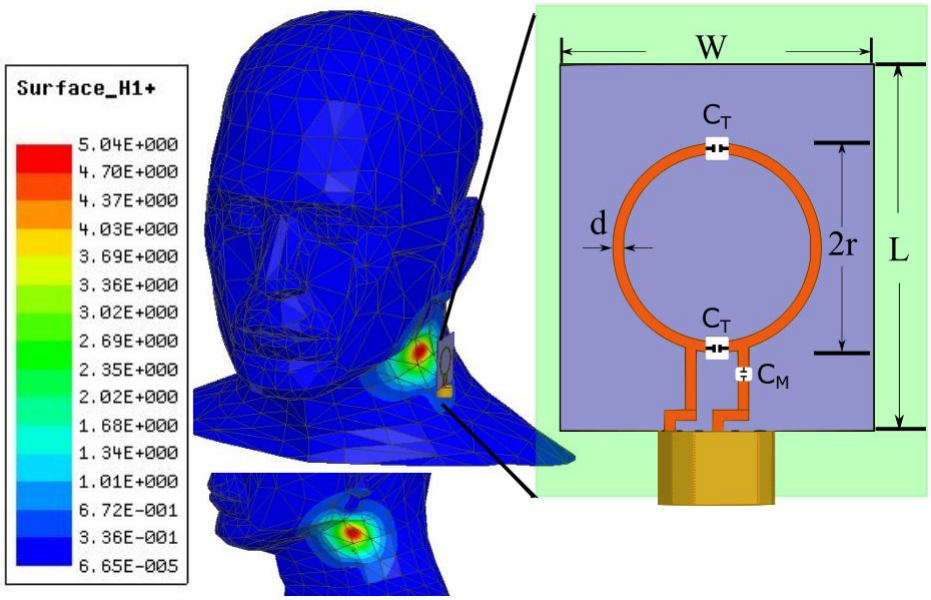

Figure 3.9: RF coil position relative to human neck and its structure including tuning capacitors. Surface H_1+ field distribution is also presented.

years, numerical methods has been used to study the effect of the human body on coil performance. In our study, performance near simplified model and anatomical human head model are both evaluated. As first step, we design the coil by tuning its resonant frequency at 127.7MHz in free space. In the second step, we simulate the coil performance near simplified human model of cylinder consisting of fatty tissue with $\epsilon_r = 6.65$, $\tan\sigma = 0.02$. Finally, the results in step 2 are validated with anatomical human model provided by HFSS.

The reflection coefficients in different environments shown in Fig. 3.9 are critical parameters. The resonant frequencies are rather close and can be readily tuned for actual clinical applications comparing the simulated (128.7MHz) and measured results (116.8MHz). The resonant frequency near human head is identical to that in the air, with slight difference in quality factor. The H_1 field distribution is critical for SNR and is shown in Fig. 3.9 with maximum of 5.04 A/m with input power of 1W. Maximum Specific Absorption Rate (SAR) averaged over 1g is 0.06 W/kg with

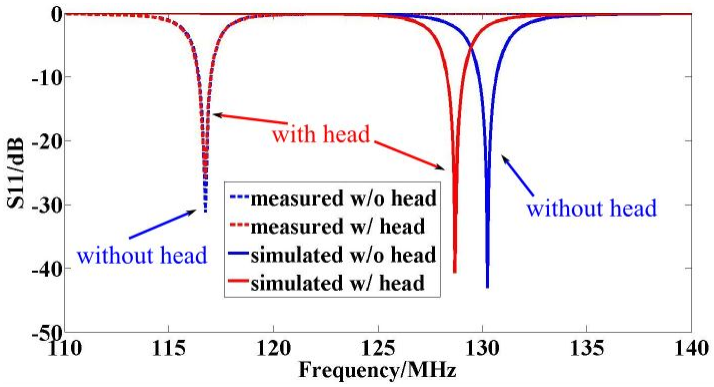

Figure 3.10: Simulated and measured S_{11} with and without human head nearby. Note a shift of about 15 MHz that could be readily tuned.

input power of 1 W.

The effect of deformation when the coil is conformal to human neck is studied by simulation in HFSS. It is shown in Fig. 3.12 that the larger deformation curvature leads to deeper signal penetration depth (larger H_1+ field) when the input is 1 W. Simulation also shows that the resonant frequency is shifted only by 1.1 MHz when the coil is conformal to cylinder with radius of 30 mm.

3.5.2 RF coil element using conductive thread

Following the design strategies for RF coils made of rigid materials. We proceed to step two in the roadmap. A single coil using electro-textiles is designed, fabricated and measured. Liberator 40 from Syscom Advanced Materials [61] is used as the electro-textile due to its high conductivity (linear conductivity of around 3Ω/m) and superior strength. Silver epoxy is used to connect capacitors, SMA port and the coil. The coil is simulated in HFSS near the 4mm accuracy human neck model before being sewed on cotton cloth. The design and detailed parameters is seen in Fig. 3.12 and Table 3.2.

The simulated and measured S_{11} is shown in Fig. 3.12. The S_{11} of the simulated coil near human neck model is -27.5 dB at 128.1MHz. The S11 of the fabricated coil

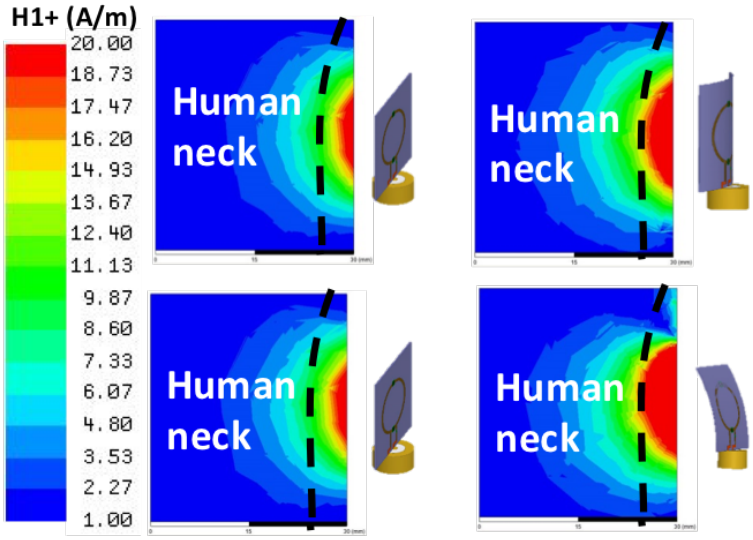

Figure 3.11: H_1+ distribution of 30 mm×35mm cut 10mm away from the coil center

Table 3.2: The design parameters of the single element RF coil using electro-textiles

Parameter	substrate width, W	substrate length, L	Loop radius, r
Value	30 mm	35 mm	10 mm
Parameter	Loop width, d	C_T	C_M
Value	1.26 mm	60 pF	10 pF

using electro-textiles is -19.8 dB at 122 MHz. The small shift in resonant frequency can be tuned back with varable capacitors or tuning kit. There is no significant shift in resonant frequency comparing S_{11} measured in open air, near human neck and on human neck for the coil diameter of 10 mm. Apparent shift in resonant frequency and degradation of impedance matching can be observed when the diameter increases to 50 mm.

Fig. 3.13 shows the effect of two exemplary parameters on S_{11}. The difficulty of collective subtleness in the coil size, touch resistance, series resistance of different components and linear resistance of the electro-textiles in the coil array design is

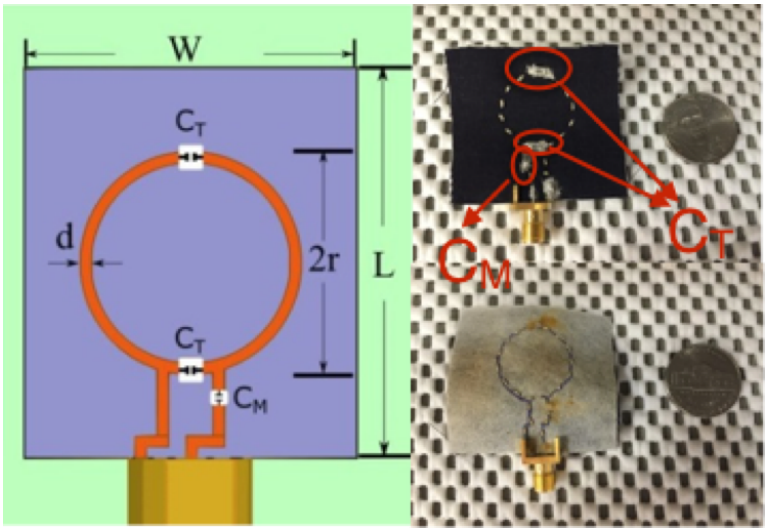

Figure 3.12: The structure and the fabricated RF coil using electro-textiles

overcome by tunable circuitry and the accurate full wave simulation. As an example, it is observed in Fig. 3.13 that when the coil diameter is changed by 5%, the resonant frequency is shifted by around 10 MHz.

3.5.3 RF coil element using conductive cloth

The previous section discusses the coil element design using conductive thread. An alternative method is to integrate conductive cloth with normal cotton cloth. In Fig. 3.15, the electro-textile coil element using conductive cloth SHIELDIT Super. The coil element pattern is laser cut and attached to the cotton cloth using adhesive material. The electronic components are soldered onto the surface with controlled temperature.

It should be noted that during the system performance characterization process, the coil element and coil array with conductive cloth are used due to its advantage of being easy to fabricate. The dimension details are shown in Fig. 3.16. The dimensions of the element used for array design and system performance characterization remain the same. The capacitor and inductors values may vary a little.

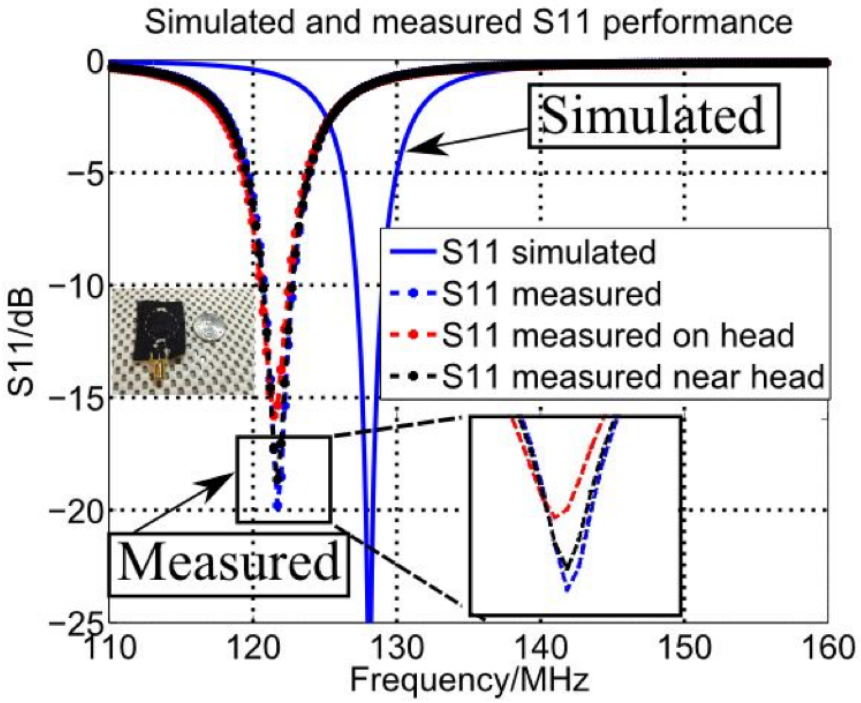

Figure 3.13: The simulated (together with cylindrical human neck model) and measured S_{11} in the open air, near the human neck and on the human neck.

3.5.4 RF coil element using tunable circuitry

One of the key difficulties of the coil element design using electro-textiles at 3T is to accurately tune the resonant frequency exactly at 127.7 MHz due to the narrow bandwidth of the coil and the RF transmission signal, as is shown in [60]. The conventional methodology involves a lengthy trial and error process near human phantom, which is impractical when using electro-textiles. We propose a tunable circuitry with varactors and variable capacitors shown in Fig. 3.17 to accurately tune the resonant frequency exactly at the designated frequency. PELCO opropanol-graphite-based paint is used for DC bias. It should also be noted that the series resistance associated with the varactors needs to be considered in full wave simulation for accurate modeling. The measured S_{11} of the fabricated tunable RF coil element is -24.5 dB at exactly 127.7 MHz in Fig. 3.18. It can be seen that the sim-

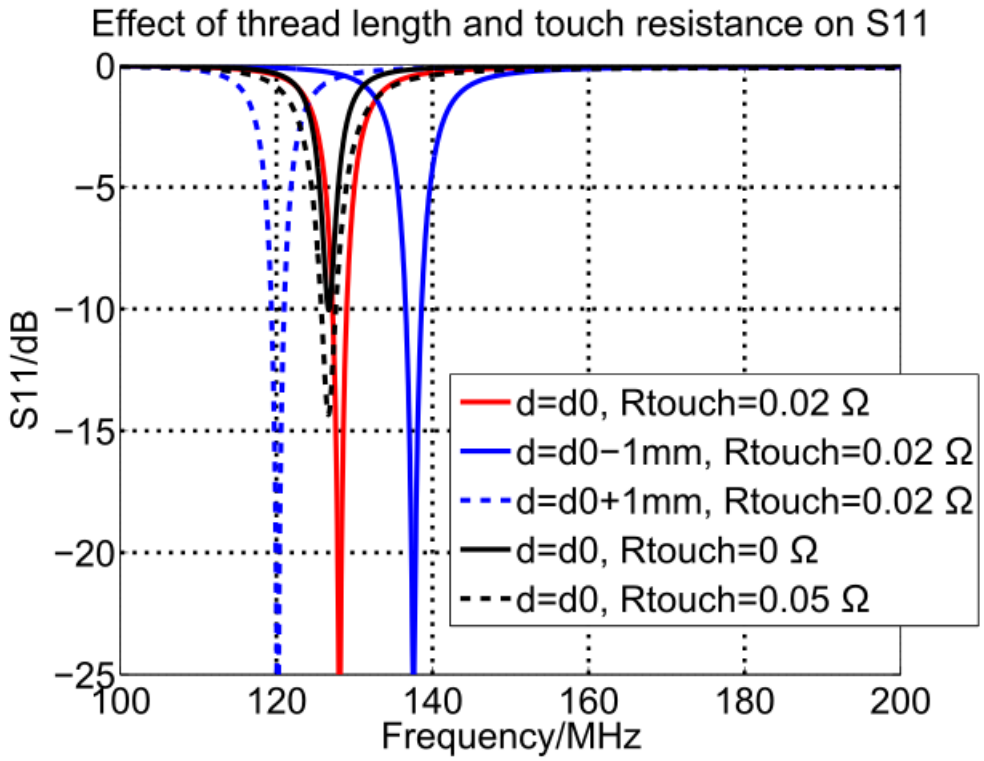

Figure 3.14: The effect of coil element diameter d and the touch resistance R_{touch} on the simulated S_{11} of the coil elements. The diameter of the coil element is 2 cm.

ulation result agree well with the measured result. Additionally, when the serious loss of the capacitors are not included, the impedance matching is degraded.

3.6 Design of MRI RF coil arrays

The major design challenge for high SNR coil array is low mutual interaction between each coil elements. In our design, two overlapped (zeroing the mutual flux) circular coil elements are designed to achieve low mutual coupling. In our design, 12 mm (around 0.48 radius) overlap is used to achieve the lowest coupling. The radius of the coil element in the coil array is 25 mm as shown in Fig. 3.19 to achieve large covering area. It is necessary that the human model used in full wave simulation

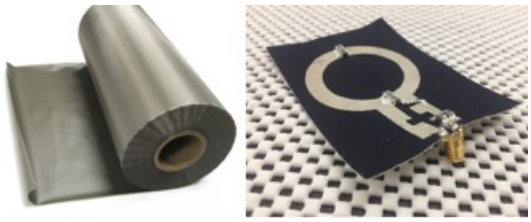

Figure 3.15: The electro-textile coil element using conductive cloth SHIELDIT Super. The coil element pattern is laser cut and attached to the cotton cloth using adhesive material. The electronic components are soldered onto the surface with controlled temperature.

for the coil of this size. A detailed method for simulation with human model can be found in [3]. In order to reduce the influence of human body, the direct touch of human body and the coil is avoided by adding the cotton cushion at the bottom as is shown in Fig. 3.19. The highly conductive electro-textile of Liberator 40 by Syscom Advanced Materials with linear resistance of around 3Ω/m is used.

The RF coils with lithography method and electro-textiles are simulated and measured. As shown in Fig. 3.20, S_{11} performance is tuned to exactly 127.7 MHz with the minimum of -18 dB, which agrees well with the simulated value. Additionally, the measured S_{12} has a maximum of around -16 dB, which is within the acceptable range. It is also found that the S_{11} and S_{12} would change dramatically if the overlap distance is smaller than 12 mm or larger than 14 mm. S11 minimum is shifted by 1.1 MHz when the coil with the radius of 10mm is conformal to the cylinder with the radius of 30 mm, which can be tuned back using tunable circuitry. The detailed B_1+ (left hand circularly polarized magnetic signal emanated from hydrogen nuclei) simulation with the human model of 2 mm accuracy shows that the conformal surface coil penetrates the human body deeper than the flat coils, which implies higher SNR.

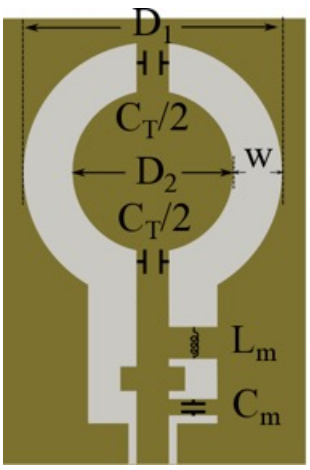

D_1	D_2	w
36 mm	50 mm	7 mm
C_T	C_m	L_m
88.4 pF	8.4 pF	35.1 nH

Figure 3.16: The dimension details of the RF coil element using conductive cloth. The dimensions of the element used for array design and system performance characterization remain the same. The capacitor and inductors values may vary a little.

3.7 Coil SNR Performance Characterization

It was discussed that flexible RF coil has the advantage of higher SNR than the normal surface coils. It is therefore important to characterize how the RF coils affect the SNR of an image.

A commonly used preliminary method to predict the effect of RF coil on the SNR performance is to measure the quality factor ratio with Eq. 3.3. Q_{loaded} and $Q_{unloaded}$ denotes the quality factor of the RF coil with and without human loading respectively. The noise of the RF coil comes from two sources: the human body, and the RF coil material used. The noise from the human body is mainly associated with the distance from the coil to the human body and the human loading, once the coil size is determined. The latter noise source consists of the loss of conductive material, substrate material, and the electric components. The Q factor ratio quantifies how dominant the loss from the human loading is among the total loss. Meanwhile, it should be noted that the contribution to the loss from the two sources varies with different coil diameters and frequencies as shown in [41]. As a result, a fair

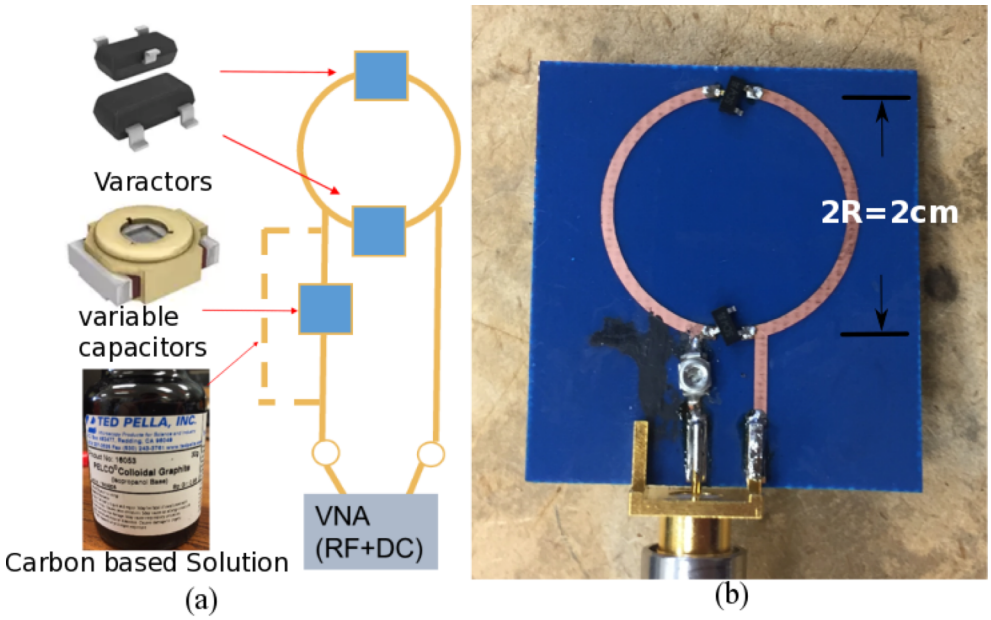

Figure 3.17: The tunable circuitry: (a) The components and the design of the coil element with accurate resonant frequency. (b) The fabricated coil element with tuning circuitry.

comparison of the Q ratio requires a fixed coil size, frequency and measurement setup. It is measured that the designed RF coil in copper and electro-textile with a diameter of 5 cm has Q ratio of 2.1 and 1.5 at 127.7 MHz respectively, using the measurement setup that will be discussed later in this section. It indicates the the copper coil is less lossy compared with the electro-textile coils as expected.

$$QRatio = \frac{Q_{unloaded}}{Q_{loaded}}, \tag{3.3}$$

In order to directly link the loss of RF coil material to SNR of the coil, the relationship between the total available SNR and Q ratio is shown in Eq. 3.4, where SNR_0 is the total available (or intrinsic) SNR described in [55].

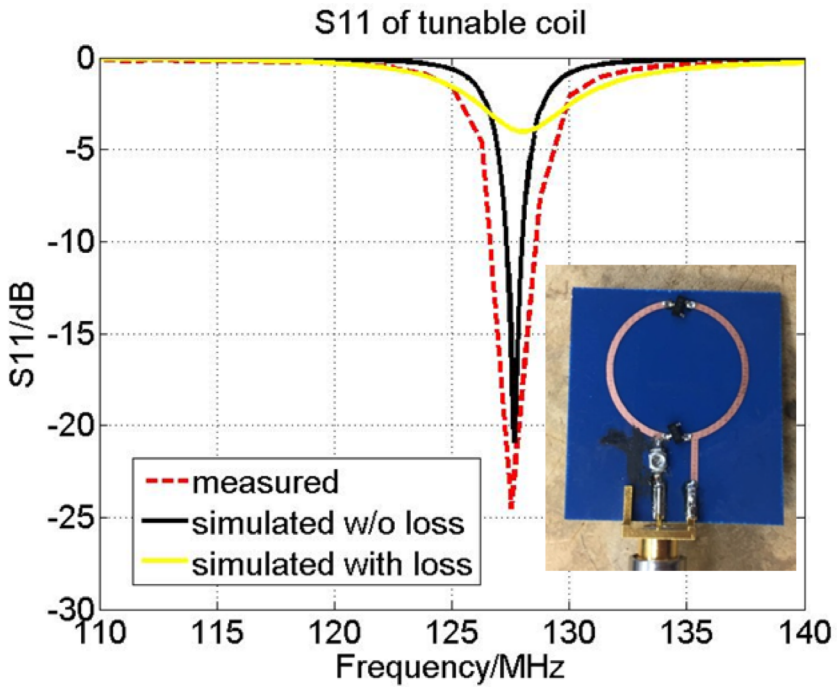

Figure 3.18: The measured S_{11} of the fabricated tunable RF coil element is -24.5dB at exactly 127.7MHz. It can be seen that the simulation result agree well with the measured result. Additionally, when the serious loss of the capacitors are not included, the impedance matching is degraded.

$$SNR = SNR_0\sqrt{1 - \frac{Q_{loaded}}{Q_{unloaded}}} \tag{3.4}$$

Additionally, it can also be derived that the SNR is linearly proportional to $\sqrt{Q_{loaded}}$ under the condition that the same phantom loading is used. As a result, $\sqrt{Q_{loaded}}$ indicates how much RF coil noise impacts the total available SNR. In order to compare the performance of RF coil made with electro-textile and copper, relative SNR can be defined in Eq. 3.5 [56]. Utilizing the Q_{loaded} measured using the setup in Fig. 3.21, we find that the relative SNR of the electro-textile copper coil is 40% of that using copper and dielectric substrate.

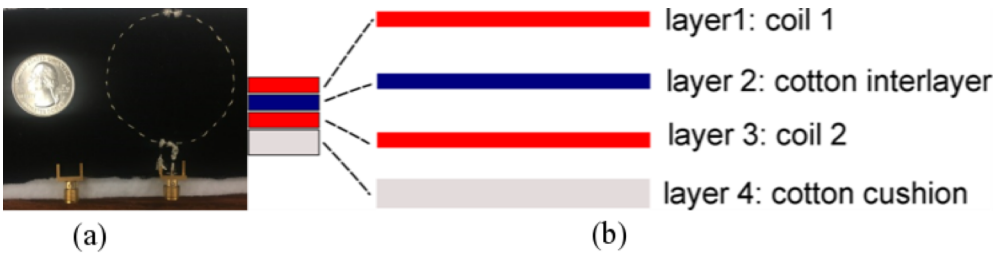

Figure 3.19: The coil array structure: (a) The front view of the fabricated coil array with electro-textiles. One coil element is in the front, and the other coil element is in the back. (b) The side view of the 4-layer coil array structure with electro- textiles. The overall thickness is 1.88mm. Note the location of the front and back coils are shown in red.

$$SNR_{relative} = \sqrt{Q_{loaded}} \tag{3.5}$$

The Q factor measurement is conducted at UCLA Antenna Research Analysis and Measurement lab. The measurement setup is shown in Fig. 3.21. The two broadband RF probes built in UCLA ARAM lab are separated by 14 cm and connected with two ports in Vector Network Analyzer (VNA) HP 8753E. The S_{21} is measured to observe the quality factor of the RF coil under test. The cylindrical standard phantom is used. The phantom is filled with 1900 ml solutions (per 1000g H_2O dist.: 3.75g $NiSO_4 \times 6H_2O$+5 g NaCl). The conductivity is 1.109 S/m and the relative permittivity is 72.84 at 127 MHz. The RF coil under test is placed 1 cm away from the outer perimeter of the phantom.

3.8 System integration of MRI RF coil arrays with MRI scanners

A commonly used method to estimate the performance of the RF coils is discussed in the Section 2.2. This method is effective in the design phase of the MRI RF

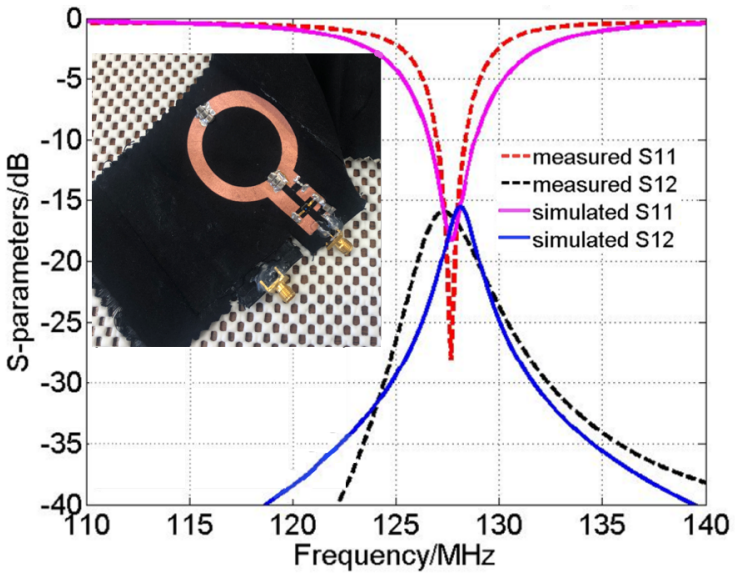

Figure 3.20: The simulated and measured S_{11} and S_{12} of the fabricated coil array. Note that one coil is in the front and one coil is in the back.

coils. In order to get a more accurate description of the RF coil array performances, the RF coils need to be integrated with the MRI scanners. The system integration process not only helps to characterize the RF coil arrays by extracting the SNR information, but also helps to show the system performance improvement with the electro-textile RF coil array.

In the Fig. 3.22, the mock-up is shown to illustrate the composition of the necessary components of RF coil array when integrated to the MRI scanners. The RF coil array and transmission decoupling circuitry are connected with coaxial cables. The transmission decoupling circuitry is further connected with the MRI scanners using coaxial cables. The coil array and transmission decoupling circuitry are separated by some distance for two reasons. Firstly, it minimizes the effect of high current during the transmission mode on the imaging area. Secondly, it minimizes its presence for the patient and as a result is more ergonomic. One of the most critical components is the transmission decoupling circuitry. It should be noted that the pre-amplifier is regarded as part of the transmission decoupling circuitry in the figure 3.22. The

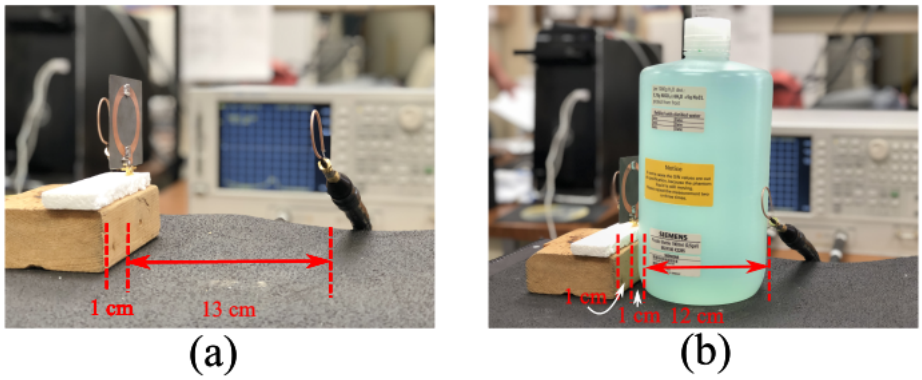

Figure 3.21: The quality factor measurement setup (a) $Q_{unloaded}$ measurement setup. The two broadband RF probes are separated by 14 cm to guarantee that they are weakly coupled. (b) Q_{loaded} measurement setup. The RF coil under test is placed 1 cm away from the outer perimeter of the phantom. The phantom is filled with 1900 ml solutions (per 1000g H_2O dist.: 3.75g $NiSO_4 \times 6H_2O$+5 g NaCl). The conductivity is 1.109 S/m and the relative permittivity is 72.84 at 127 MHz.

transmission decoupling circuitry is used to show high impedance when the MRI scanner is working in the transmission mode. As is mentioned in Chapter 2, in the transmission phase, the transmission coils usually embedded in the MRI scanners are turned on and the hydrogen spins are excited to the xy plane. To keep the homogeneity of the static magnetic field and the desired effect by the gradient coils, receive-only coils should be shut down at this time. The transmission-decoupling circuitry is turned on at this time to shut down the receive-only coil.

One of the most commonly used transmission decoupling circuit is shown in the Fig. 3.23. The PIN diode serves as a switch that is turned on in the transmission mode and is turned off in the receiving mode. When the diode is turned on, the decoupling branch consists of C_m, L_m and $C_T/2$ resonates and shows high impedance when looking from the coil to the right. As a result, minimum current will be observed in the coil area, thus no hot spot on the imaging area.

There are two major requirements: 1. The decoupling branch needs to resonate at 127.7 MHz. 2. The input impedance looking to the left needs to be matched at

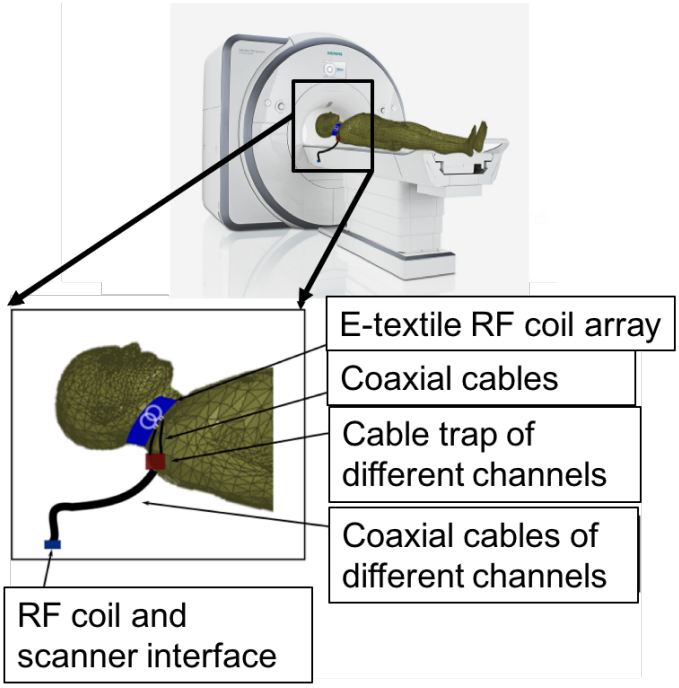

Figure 3.22: RF coil array integrated with the MRI Scanners. The RF coil array and transmission decoupling circuitry are connected with coaxial cables. The transmission decoupling circuitry is further connected with the MRI scanners using coaxial cables

50Ω at 127.7 MHz. In step 1, we estimate value of C_m and L_m. Since we already have the design for receive-transmission coils talked about in the Section 3.5.2, we can fix the value of C_T and find the value of C_m and L_m using the circuits shown in the Fig. 3.23. In step 2, the resistance and the inductance of the coil is incorporated to validate the accuracy of the design proposed in step 1. In the step 3, the dimensions of the variable inductor L_M is calculated according to the design in step 2. Alternatively, an MRI compatible inductor is selected at this stage. The inductors are variable to tune exactly at the 127.7 MHz for a specific loading being measured on-site. It is noted that the capacitors, the SMA connectors, and the PIN diodes for the MRI applications should be non-magnetic. The PIN diode is usually used because of the superb power handling capability, high quality factor, and small switching time. It can be shown in Fig. 3.24 (b) that the PIN diode is used to

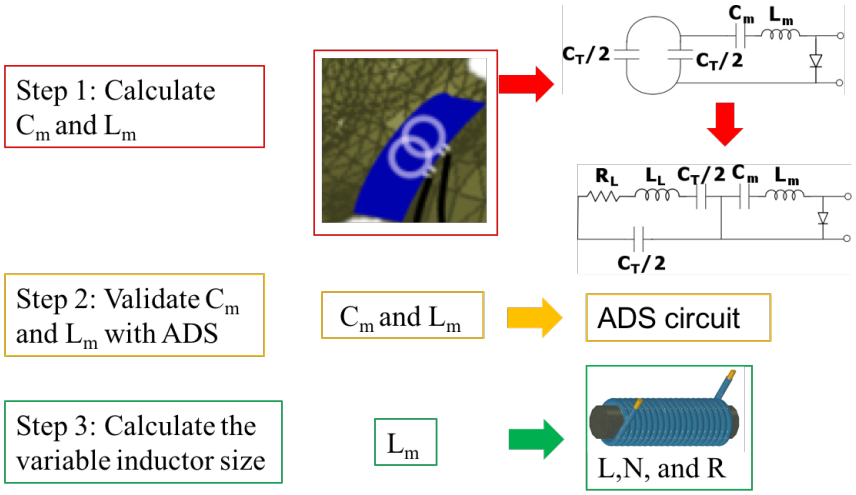

Figure 3.23: The transmission decoupling circuitry is designed following three steps (1) Calculate C_m and L_m to tune the circuit to resonate at 127.7MHz and match the 50Ω input impedance (2) Validate the C_m and L_m values through ADS (3) calculate the actual size of the variable inductor (L is the length of the inductor, N is the number of turns, the R is the radius of the inductor)

form large impedance in the resonant loop. The RF coil array is shown in Fig. 3.24 (a) with 4 channels and optimized overlap distances. There are 2 channels on the left and right sides of the human neck respectively. Since they are far apart, small mutual coupling is observed. It is simulated in HFSS that S_{21} is lower than -20 dB.

The right side of the circuit shown in the Fig. 3.23 are connected to a pre-amplifier. If any coaxial cable is used between the decoupling circuits and the pre-amplifier, balun (or cable trap) is necessary to prevent the common mode RF signals from entering the transmission decoupling circuitry. One potential candidate is LC parallel network balun where an inductor is connected to the outer metal layer of the coaxial cable and a capacitor is connected to the core of the coaxial cable. The common mode RF signal is reduced by the inductor and is further minimized at the 127.7 MHz when the capacitor and the inductor are resonant at this frequency. It can be shown in Fig. 3.24 (b) that the balun or RF common mode rejection choke is also implemented to increase the SNR and safety level.

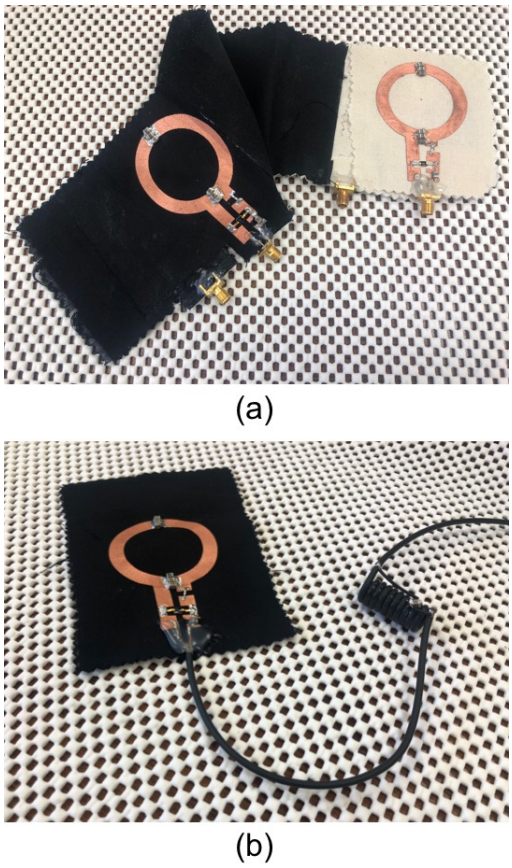

Figure 3.24: The electro-textile RF coils using laser cut technology (a) Electro-textile coil array (b) Electro-textile element with a common mode rejection balun/choke

The electro-textile is further designed specifically for neck area with ergonomic considerations. In order for the UCLA electro-textile coils to be perfectly fit for the neck, an actual human neck model is used. The human neck has a complex structure because of the different curvature in neck, upper shoulder, and lower head area. As a result, different part of the RF coils are actually in different planes and need to be designed and placed carefully to ensure a full imaging area coverage and maximize comfort level. For diagnosis of carotid artery disease a good general rule of thumb for landmarks is the angle of the mandible where the carotid bifurcation is located. In majority of patients clinically important carotid disease occur at the

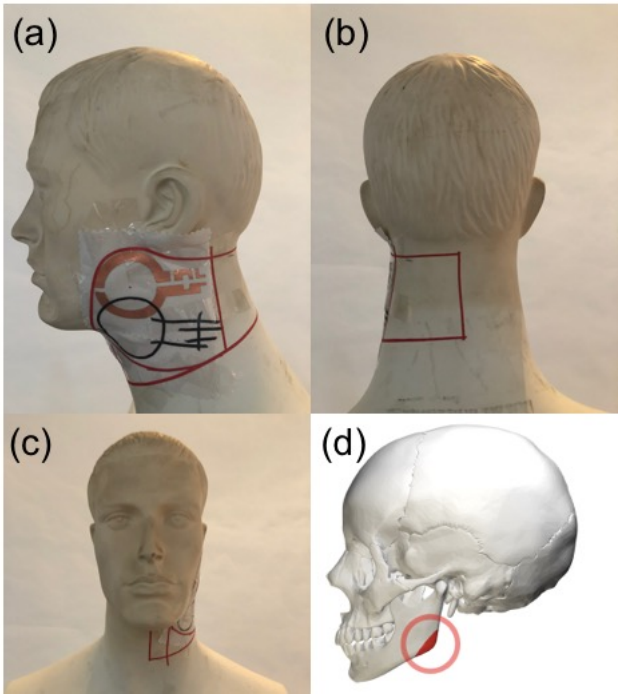

Figure 3.25: The electro-textile RF coils designed to image carotid arteries. The human model is used to find the appropriate shape and placement. (a) The side view of the model with electro-textile coils (b) The back view of the model with electro-textile coils (c) The front view of the model with electro-textile coils (d) The front view of the model with electro-textile coils with ordinary household background

bifurcation. The proximal portions of internal carotid arteries are also important for further evaluation and that means extending the field of view to just below the level of ears. This is roughly 4-5 cm higher than the angle of mandible. The mandible is shown in Fig. 3.25 (d). It is shown in Fig. 3.25 (a)(b) and (c) that the designed RF coil covers the targeted area.

It should also be noted that plastic paper is needed to scan the cadavers provided by UCLA Donated Body Program. More protection of the preamplifier is needed to prevent any potential hazards brought about by the paper. Scanning failures are found if the preamplifiers are not originally covered by a protection case. In Fig. 3.26 shows the UCLA electro-textile RF coil array and Siemens FLEX coil array covered

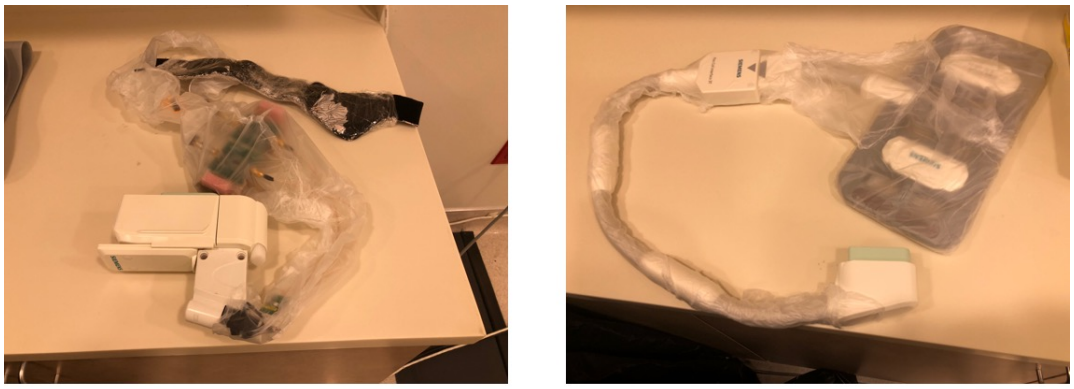

Figure 3.26: The UCLA electro-textile RF coil and Siemens FLEX coil are wrapped with plastic paper before cadaver measurement. (a) Electro-textile coil (b) Siemens FLEX coil

with plastic papers. A better protection is found in Fig. 3.27 using a case laser cut and glued together using acrylics.

Preamplifier is built using TL5500 for 3T MRI application. It is critical that the input of the pre-amplifier is noise matched instead of impedance matched to maximize the final SNR as discussed in [54]. The close up view of preamplifier is shown in Fig. 3.28 (a). The noise figure is measured using HP8970B noise figure meter and measurement setup is shown in Fig. 3.28 (b).

3.9 Electro-textile RF Coil System Level Performance and Characterization

In order to have a more accurate description of the RF coil array performances, UCLA Antenna Lab electro-textile RF coil array is integrated with the 3T MRI scanners. The images of a homogeneous phantom, a resolution phantom, and a beef phantom are acquired and shown in this chapter. The images are evaluated quantitatively and qualitatively to analyze the system performance. The UCLA

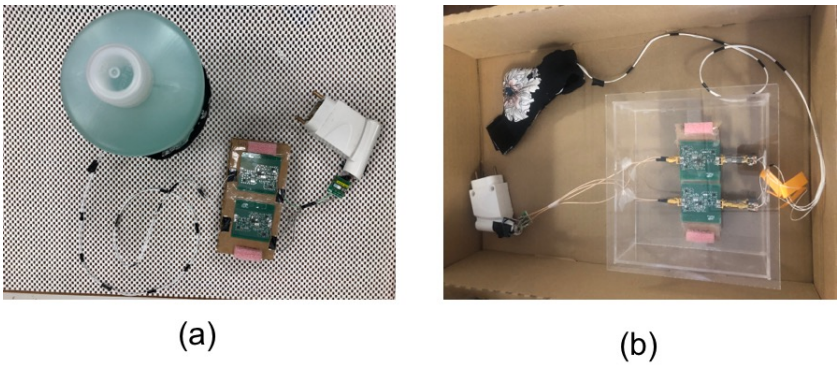

Figure 3.27: UCLA electro-textile array system integrated with preamplifier (a) coil array system (b) coil array system with protection to perform cadaver measurement.

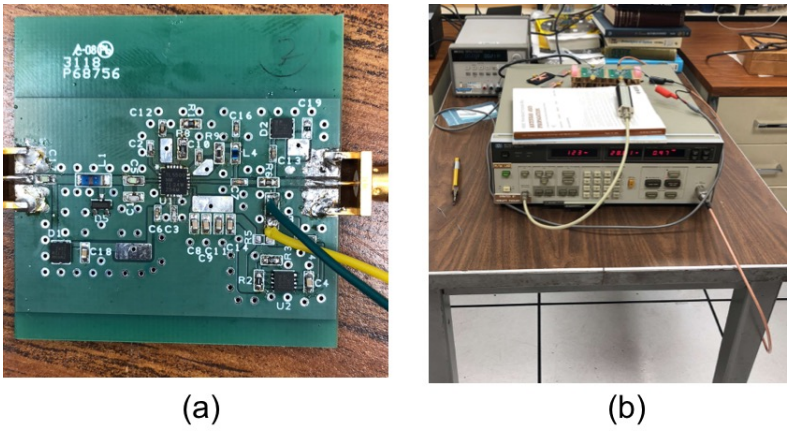

Figure 3.28: The preamplifier optimized to minimize noise figure (a) The close-up of the preamplifier (b) The measurement setup of the preamplifier noise figure.

Antenna Lab electro-textile coil array is further evaluated by comparing the SNR performance at different depths with conventional surface coil array in the same phantoms after back-to-back imaging trials.

The measurement setup is shown in Fig. 3.33. The phantom is placed in the same orientation as the neck when the patient is scanned. The electro-textile RF coil array with two elements is taped to the phantom with a 1 cm thick foam in between. It covers the effective image area of 8 cm in height and 5 cm in width, which translates to 4 cm above and below the angle of mandible for an average

patient, along with other structures near to it in the lateral direction.

The images are acquired at UCLA School of Medicine using a 3T scanner. A T1 weighted spin echo sequence is applied with the flip angle of 90 degree, TR=500 ms, TE=20 ms. The field of view (FOV) is 250 mm $\times$ 250 mm with the resolution 1 mm $\times$ 1 mm and the slice thickness of 5 mm. Trials are conducted back to back with UCLA Antenna Lab RF coil and conventional surface coil for each phantom. The image shown in Fig. 3.34 is the axial plane image of the homogeneous phantom. The orange ellipse denotes the coil to show its relative position with the phantom. The slice closest to the MRI scanner isocenter is selected. It can be seen that the signal close to the phantom surface is stronger than the other parts of the phantom. Additionally, the SNR near the surface is higher than that deeper in depth. The SNR of the UCLA electro-textile RF coil at 0.5 cm in depth is 4534. The SNR of the conventional surface coil at the same phantom depth is 182, after being tightly wrapped around the phantom. The SNR of the UCLA Antenna Lab coil has 14 dB increase from the conventional surface coil in this measurement setup. The SNR of electro-textile coil array at 3 cm in depth is 3 dB increase from the conventional surface coil. It should be further pointed out that the SNR of the UCLA electro-textile coil element is 37% of that of the UCLA copper coil element of the same size at the depth of 0.5 cm. This result agrees well with the relative SNR approximation of 40% by measuring the loaded quality factor discussed in Section 3.7. A review and comparison of the methods used to characterize the SNR of the MR images are described in [66]. The difference method is used in our analysis due to the higher accuracy comparing with other methods [66] in multi-channel scenarios and the potential use of parallel imaging cases.

The high resolution and contrast of the image can be achieved with the superior SNR performance that the system provides. The electro-textile MRI RF coil array is used to image a resolution phantom. The orange ellipse denotes the coil to show

its relative position with the phantom. The fine signature of the phantom is marked with a red rectangle. Three pairs of squares consisting of 4 × 4 hole matrix, with smallest hole dimension being 0.9 mm × 0.9 mm, can be clearly observed, although these small features are located at the larger depth. The pixel size is 0.5 mm × 0.5 mm. The rest of the measurement setups are the same as those used as the homogeneous phantom case. It shows that the performance by the UCLA electro-textile coil array is still reasonable at the larger depth.

The performance of the electro-textile RF coil array is further illustrated by imaging a cylinder phantom filled with beef. It has a different loading effect compared with the saline water based phantoms. The axial plane image of the beef phantom is shown in Fig. 3.36. The shape and details of the beef can be observed clearly. The parts of the beef phantom with fat (denoted with red arrows and circles in Fig. 3.36) are bright compared with the other tissues at the same depth. The details can still be observed if the overall brightness is tuned down. The same measurement setups are used as the homogeneous phantom case.

The SNR performance throughout the imaged phantom can be observed by using raw data acquired by the Siemens scanner. The SNR distribution by UCLA coil element and Siemens FLEX coil element is shown in Fig. 3.29 and Fig. 3.30 respectively. The SNR ratio is shown in Fig. 3.31.

It is critical that the Noise Correlation Matrix (NCM) of an RF coil array is evaluated. This figure of merit is critical for the potential use of parallel imaging, where g factor heavily depend on the small mutual coupling between the elements. The NCM reflects the mutual coupling between elements and is calculated in [41] In order for parallel imaging to be implemented with high quality, a rule of thumb is suggested in (3.6). It is suggested in [41] that the variation of on-diagonal real elements in the NCM is >35%. Additionally, the largest off-diagonal element is >25% of the largest on-diagonal element. The Noise Correlation Matrix (NCM)

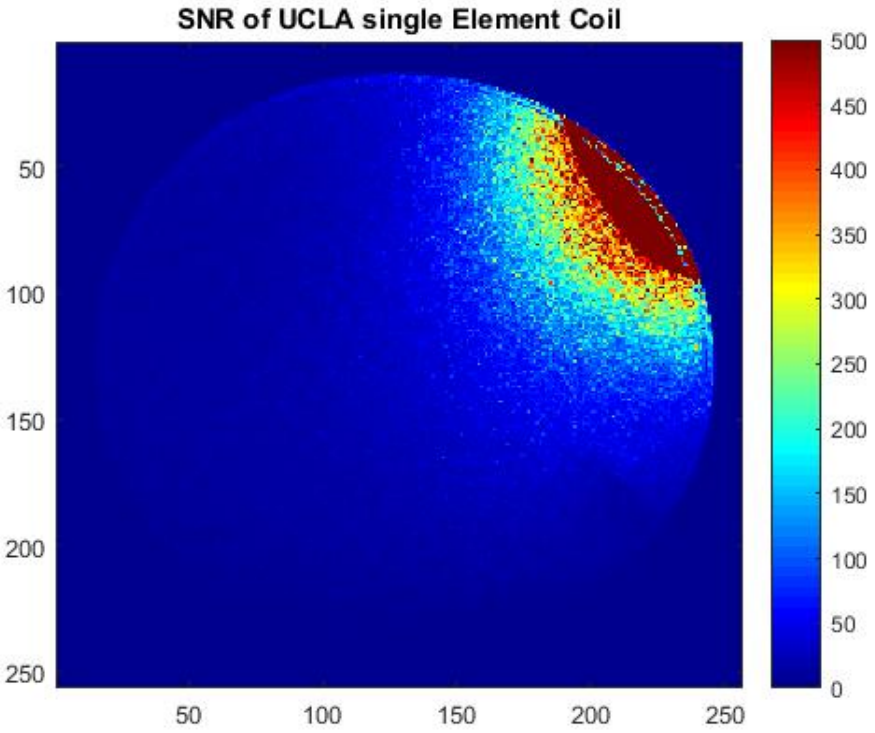

Figure 3.29: The SNR map of single element UCLA electro-textile RF coil. T1 spin echo sequence is used.

of the UCLA flexible coil array calculated based on the raw data acquired with Siemens 3T scanner. The transmission RF channel is turned off before acquiring noise data. According to the data the coil array satisfies the requirement to support high performance using parallel imaging schemes.

$$R_{ij} = \sum_{k=1}^{n} n_i(k) n_j^*(k) \tag{3.6}$$

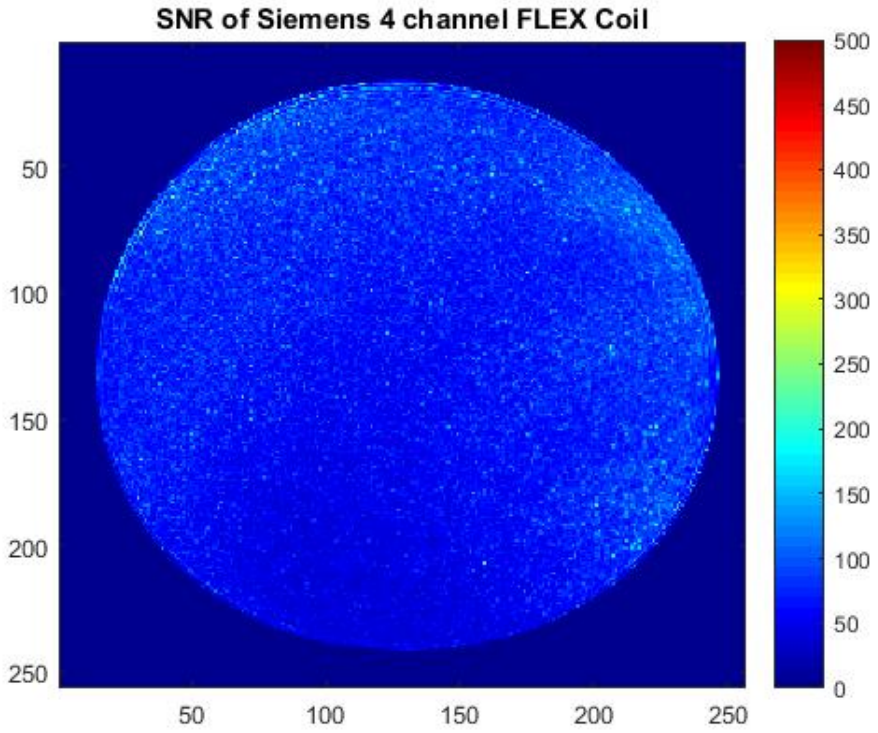

Figure 3.30: The SNR map of Siemens coil. T1 spin echo sequence is used. It is noted that the same scale is used as the previous figure

3.10 Cadaver Measurement using UCLA Electro-textile RF coil array

The high performance of the UCLA electro-textile RF coil array is further validated through cadaver measurement using Siemens 3T scanner at UCLA TRIC shown in Fig. 3.37 . The SNR by UCLA flexible coil at a specific ROI is 6.8 times higher than that of the Siemens coil using T1 weighted spin echo sequence, shown in Fig. 3.38. It can be seen clearly that the image quality by the UCLA flexible coil is much better than the that acquired by Siemens coil. The same observation can be applied to the images acquired using T2 weighted spin echo and GRE sequences shown in Fig. 3.39 and Fig. 3.40. It should be noted that a reduction of the absolute value SNR is found

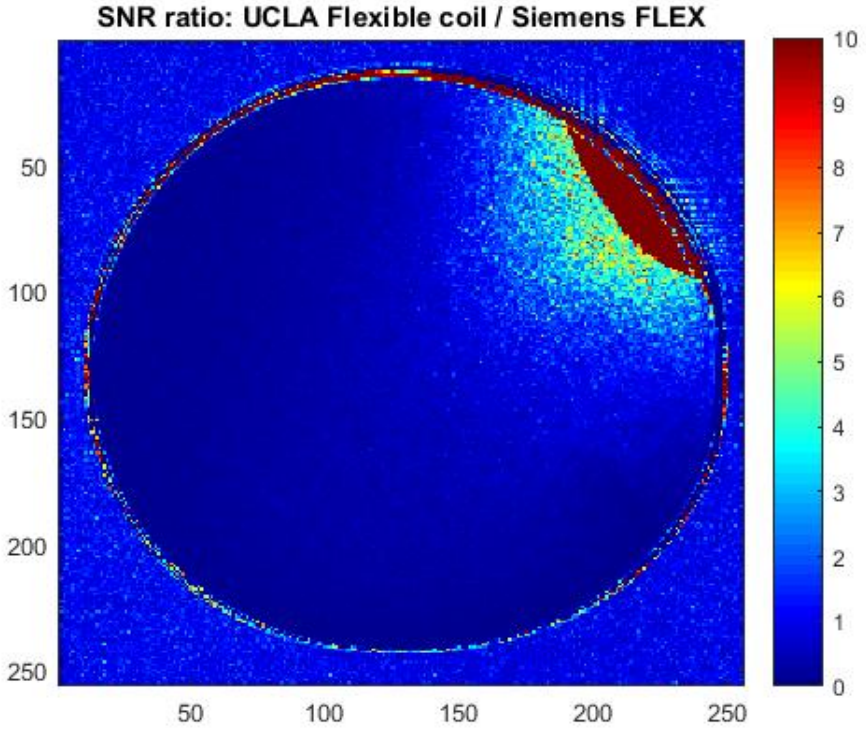

Figure 3.31: The SNR ratio map of single element UCLA electro-textile coil and 4-channel Siemens coil. T1 spin echo sequence is used. It can be seen that the ratio is over 10 for thickness of smaller than 1 cm from the imaging surface. The ratio is around 4 at the depth of 3 cm.

when imaging cadaver neck than saline water phantom. This is because saline water has more abundant hydrogen nuclei than cadaver neck area. The SNR improvement by the UCLA electro-textile over Siemens FLEX coil array is still obvious.

3.11 Neck RF Coil Design and Performance Summary

The results presented in the previous sections are mainly single element coil or RF coil on one side of the neck. In this section, the final design steps and results using the most updated 4-channel electro-textile RF coil are summarized using 4-channel RF coil with improved construction and configurations with better stability.

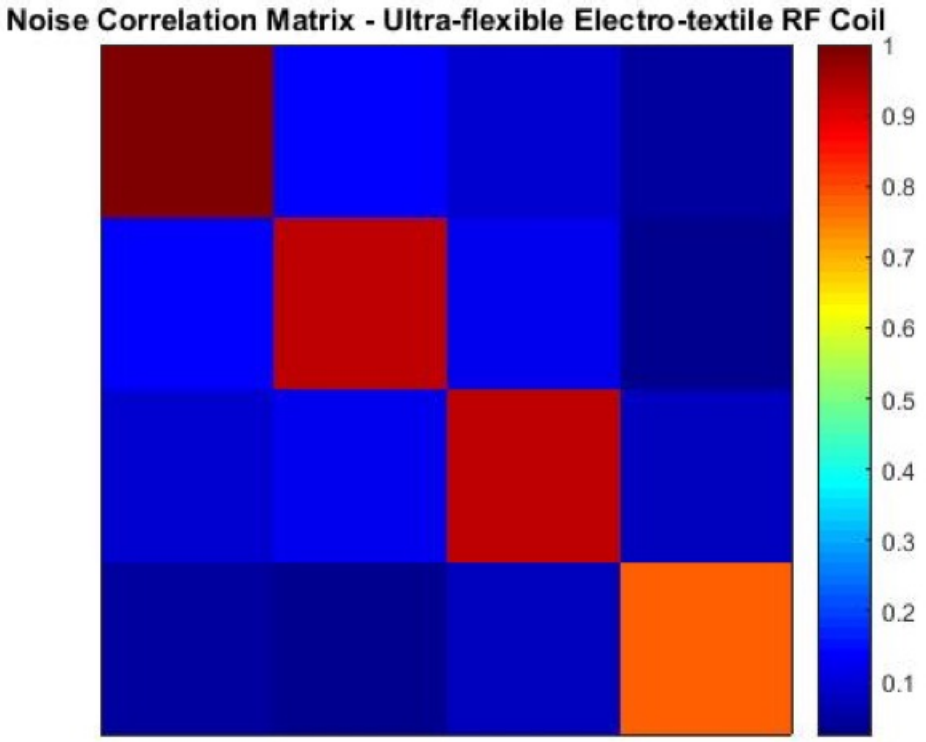

Figure 3.32: The Noise Correlation Matrix (NCM) of the UCLA flexible coil array calculated based on the raw data acquired with Siemens 3T scanner. The transmission RF channel is turned off before acquiring noise data. According to the data the coil array satisfies the requirement to guarantee high performance using parallel imaging schemes.

The results including the S-parameters, the magnetic field distribution (for parallel imaging potentially in the future), the phantom images and SNR, and the cadaver images and SNR will be summarized in this section.

3.11.1 E-textile characterization and coil design

We used a conductive cloth with superb conductivity at 123 MHz (3 Tesla). The design process involves four major steps. First, the e-textile effective conductivity of 4×10^6S/m at 123 MHz was found using a four-microstrip-line measurement method, where the conductive cloth surface roughness was considered. Second, High

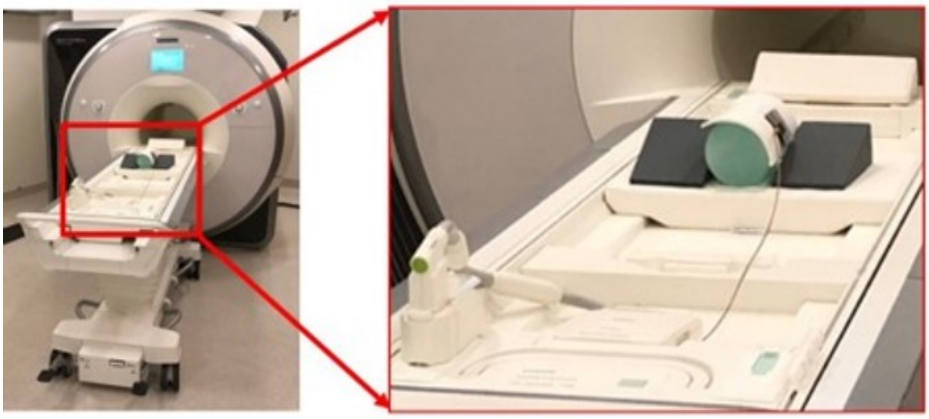

Figure 3.33: The UCLA electro-textile RF coil array is taped to the phantom with an 1 cm thick foam in between. The image is obtained at UCLA School of Medicine using 3T MRI scanner.

Frequency Electromagnetic Field Simulation Software (HFSS) was used incorporating the effective conductivity found in first step. Third, coil pattern based on the design in second step was fabricated using computerized laser cutting facility (Epilog Laser Helix) and was attached to cotton cloth using adhesive materials. The electrical components were soldered onto the pattern with controlled temperature. Finally, the coil elements were fine-tuned near a saline water phantom. The coil element diameter was 5 cm to target the neck tissues. The 4-channel RF array coil was designed and optimized with two overlapped elements on each side of the neck (Fig. 3.41a). It comfortably and closely wraps around the patient's neck (Fig. 3.41b). PIN diodes were used to detune the coil during the RF transmission phase. The preamplifier (TI TL5500) was noise-matched to achieve 0.5 dB Noise Figure (NF) and 28.5 dB gain.

3.11.2 MRI experiments

The ultra-flexible e-textile coil and a 4-channel standard surface coil (small flex coil, Siemens) were used to scan a water phantom (Fig. 3.42f) and the neck of an

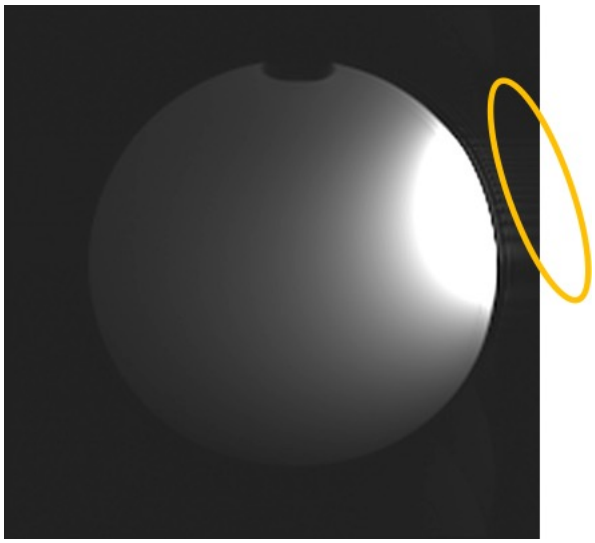

Figure 3.34: The axial plane image of the homogeneous cylindrical phantom shown in Fig. 3.21(b). The orange ellipse denotes the coil to show its relative position with the phantom. It can be seen that the signal close to the phantom surface is stronger than the other areas. Additionally the SNR of UCLA electro-textile coil is 4534 at 0.5 cm depth selecting a circular area of 40 mm^2 in the center of the targeted area. The SNR of the conventional surface coil is 182 at the same phantom depth, after being tightly wrapped around the phantom. The SNR of the UCLA electro-textile coil has 14 dB increase from the conventional surface coil in this measurement setup at the depth of 0.5 cm and an increase of 3 dB at the depth of 3 cm. The slice closest to the MRI scanner isocenter is selected. A T1 weighted spin echo sequence (90 degree flip angle) is used. The pixel size is 1 mm $\times$ 1 mm. The field of view (FOV) is 250 mm $\times$ 250 mm.

unembalmed cadaver at room temperature at 3T (Prisma, Siemens) (Fig. 3.43a, b). Biosafety approval was obtained for human cadaver research. The coil locations are indicated by the yellow ellipses. A T1-weighted spin-echo sequence was used for both phantom and cadaver, with $1 \times 1mm^2$ in-plane resolution, 0.8 mm slice thickness, and FOV=$320 \times 320mm^2$. For phantom scans: TR=573 ms, TE=20 ms. For cadaver scans: TR=309 ms, TE=11 ms.

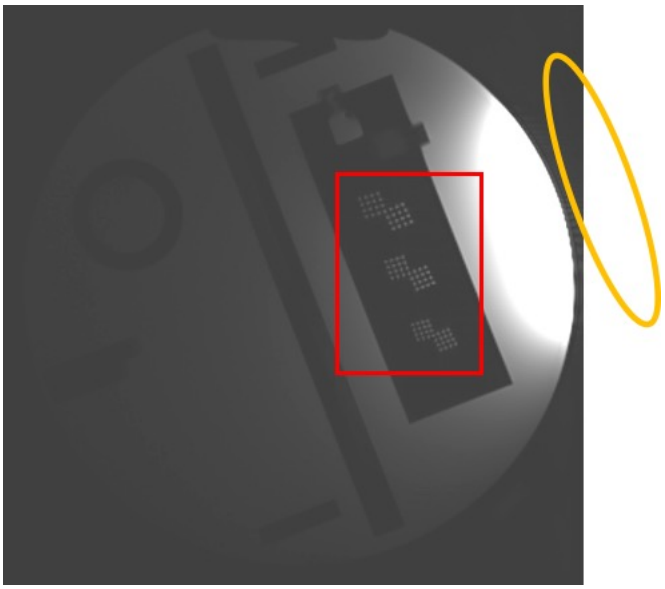

Figure 3.35: The axial plane image of the resolution phantom J1858 by J.M. Specialty parts. The orange ellipse denotes the coil to show its relative position with the phantom. The fine signatures of the phantom are marked with a red rectangle. Three sets of squares with smallest dots dimension to be 0.9 mm × 0.9 mm can be clearly observed although these small features are located at the larger depth. It shows that the SNR by the UCLA electro-textile coil array is still reasonable even when the interested structure is not at the optimal depth. The pixel size is 0.5 mm × 0.5 mm. The rest of the measurement setups are the same as those used as the previous image.

3.11.3 Simulation and bench testing

Satisfactory impedance matching was achieved at 123 MHz (Fig. 3.41c). The measured S_{21} <-15 dB between all coil elements, showing low mutual coupling. The simulated H_1- field (Fig. 3.41d) shows a deeper penetration depth in HFSS when it is conformal to the cylinder with a 10 cm-diameter.

3.11.4 Phantom imaging

The signal strength of e-textile coil near the surface is noticeably stronger than a standard surface coil (Fig. 3.42a, b). The SNR calculated using the difference method at the depths of 0.5 cm and 3 cm were 4.2 and 3.4 times (Fig. 3.44) higher

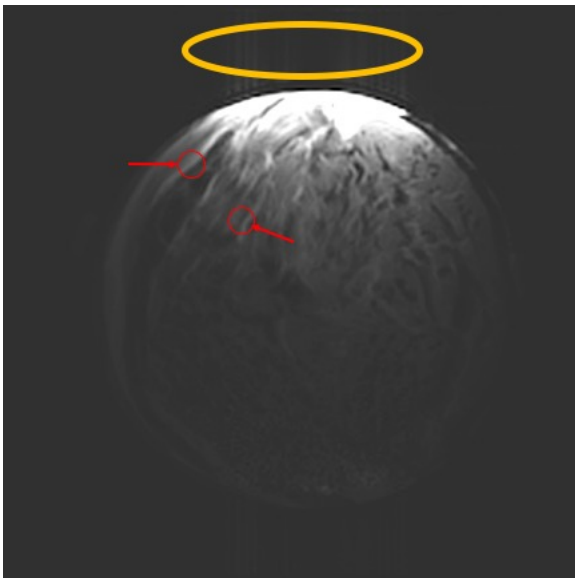

Figure 3.36: The axial plane image of the beef phantom. The orange ellipse denotes the coil to show its relative position with the phantom. The shape and details of the beef can be observed clearly. The parts of the phantom with fat are relatively bright compared with the other tissues at the same depth. The signal near the surface of the phantom are much brighter than the other areas. The details can still be observed if the overall brightness is tuned down. The same measurement setups are used as the homogeneous phantom case.

than the standard coil respectively at the indicated ROI (Fig. 3.42c, d). The noise correlation matrix shows that the minimum on-diagonal value is 77.6% of the maximum. The off-diagonal maximum is 13.4% of the on-diagonal maximum (Fig. 3.42e), indicating satisfactory coil array performance.

3.11.5 Human cadaver imaging

The signal strength near the surface is noticeably stronger than a standard surface coil (Fig. 3.43c, d). The SNR calculated using the difference method at the depths of 0.5 cm and 3 cm was 27 and 5.5 times (Fig. 3.44) higher than the standard coil respectively at the indicated ROI (Fig. 3.43e, f). An expert radiologist reported good depiction of vertebral artery and sternocleidomastoid muscle in the images.

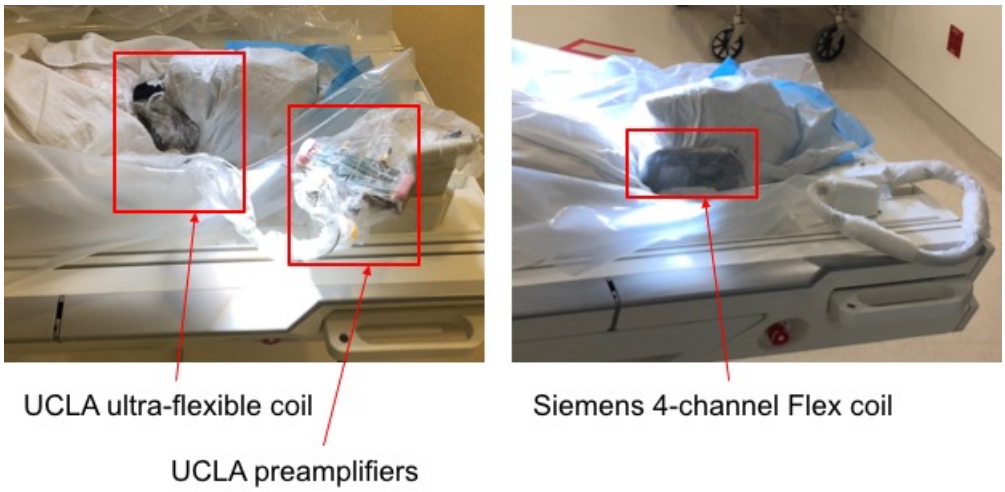

Figure 3.37: Cadaver measurement setup is shown in comparison with the the setup using Siemens FLEX 4-channel coil.

3.12 Conclusion

In this chapter, a comprehensive discussion of the design, fabrication and characterization of a electro-textile RF coil array platform is conducted. The new ultra-flexible electro-textile RF array coil shows substantial SNR advantage over a standard coil. The SNR in cadaver images at a depth of 0.5 cm from the coil was one order of magnitude higher than a standard coil. The cadaver images showed high-quality anatomical features in the neck. As the size and number of coil elements can be modified for different anatomies of interest, this technology is not limited to neck MRI. The electro-textile material can be readily applied to more areas including pediatric, joint, and extremity MRI, and MRI-guided interventions. Future work includes the in-vivo evaluation of the new coil for different diagnostic applications.

The major contribution is summarized as follows: (1) For the first time in the literature, flexible RF coil using electro-textile is shown to improve the SNR performance. A systematic approach is proposed starting from the design of single element RF coil using normal lithography method, followed by the design of electro-textile

Figure 3.38: The images acquired by UCLA flexible coil in comparison with the Siemens FLEX 4-channel coil. The SNR of the same region of interest by the UCLA coil is 6.8 higher than the Siemens coil after back-to-back trial. A T1 weighted spin echo standard sequence is used.

element and finalized by the electro-textile array.

(2) Effective method to characterize the effective conductivity of the electro-textile materials using 4 microstripline method is implemented at frequency around 120 MHz. This method dis-embed the effect of connectors and is shown to have accurate characterization of the electro-textile pattern using either embroidered conductive thread pattern and laser cut conductive cloth.

(3) A complete characterization and design procedure for electro-textile MRI RF coil is proposed and implemented. The coil element characterization can be performed using water phantom and making sure S_{11} is below -15 dB at the targeted resonant frequency. Quality factor ratio measurement is used to roughly estimate the coil performance. The S_{21} of the coil array is measured to show low mutual coupling between the elements. The system level characterization include SNR map, noise

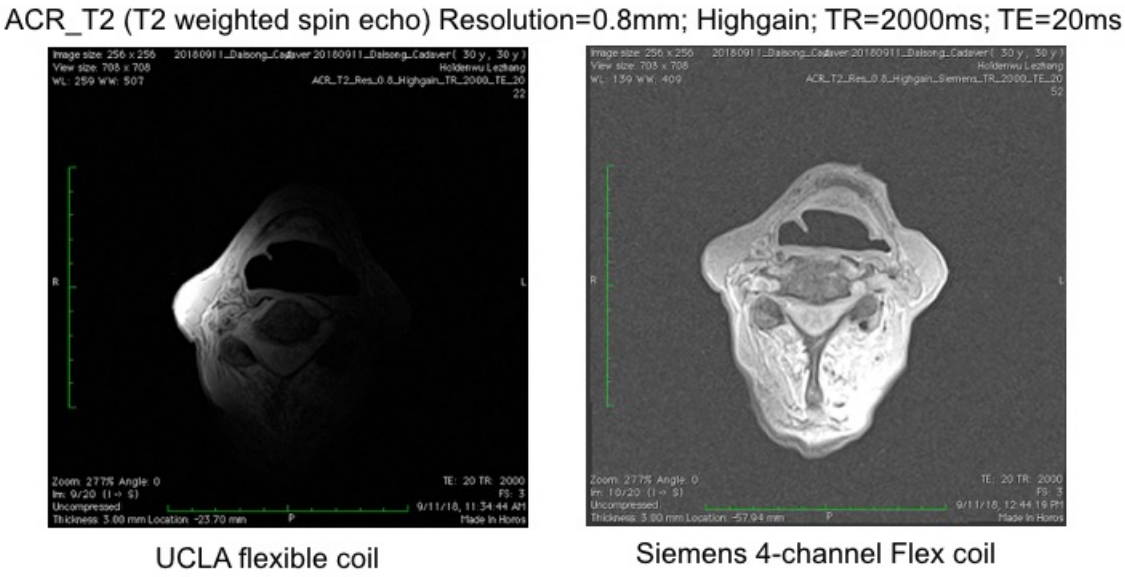

Figure 3.39: The images acquired by UCLA flexible coil in comparison with the Siemens FLEX 4-channel coil. A T2 weighted spin echo standard sequence is used.

correlation matrix and real cadaver or human measurement. The noise correlation matrix is critical not only for SNR using conventional sequences but also critical for the image quality of the parallel imaging.

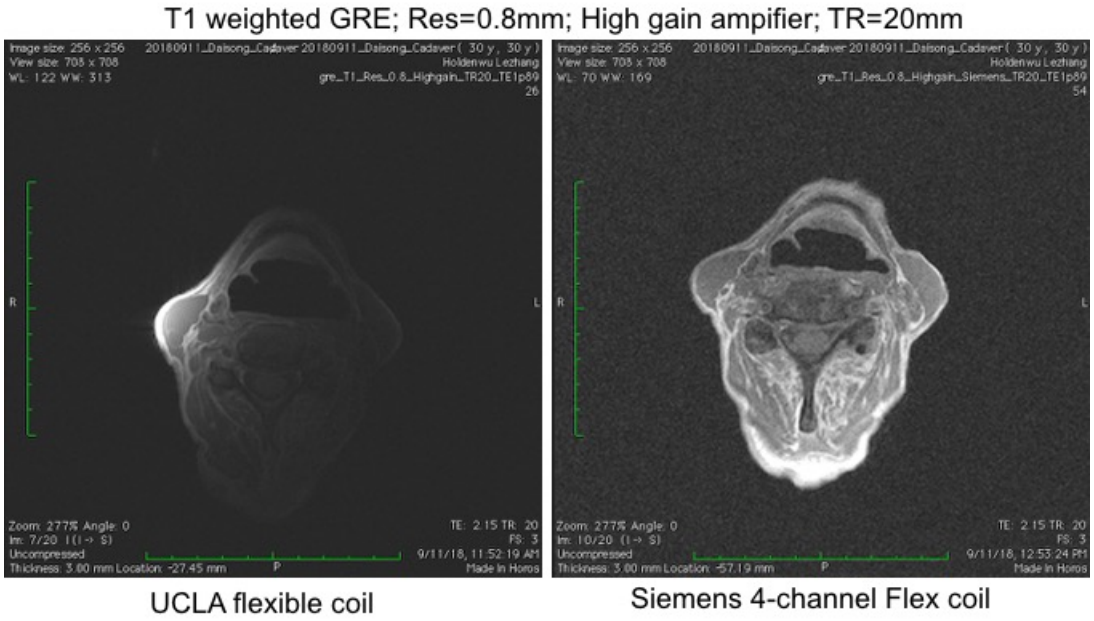

Figure 3.40: The images acquired by UCLA flexible coil in comparison with the Siemens FLEX 4-channel coil. A T1 weighted GRE standard sequence is used.

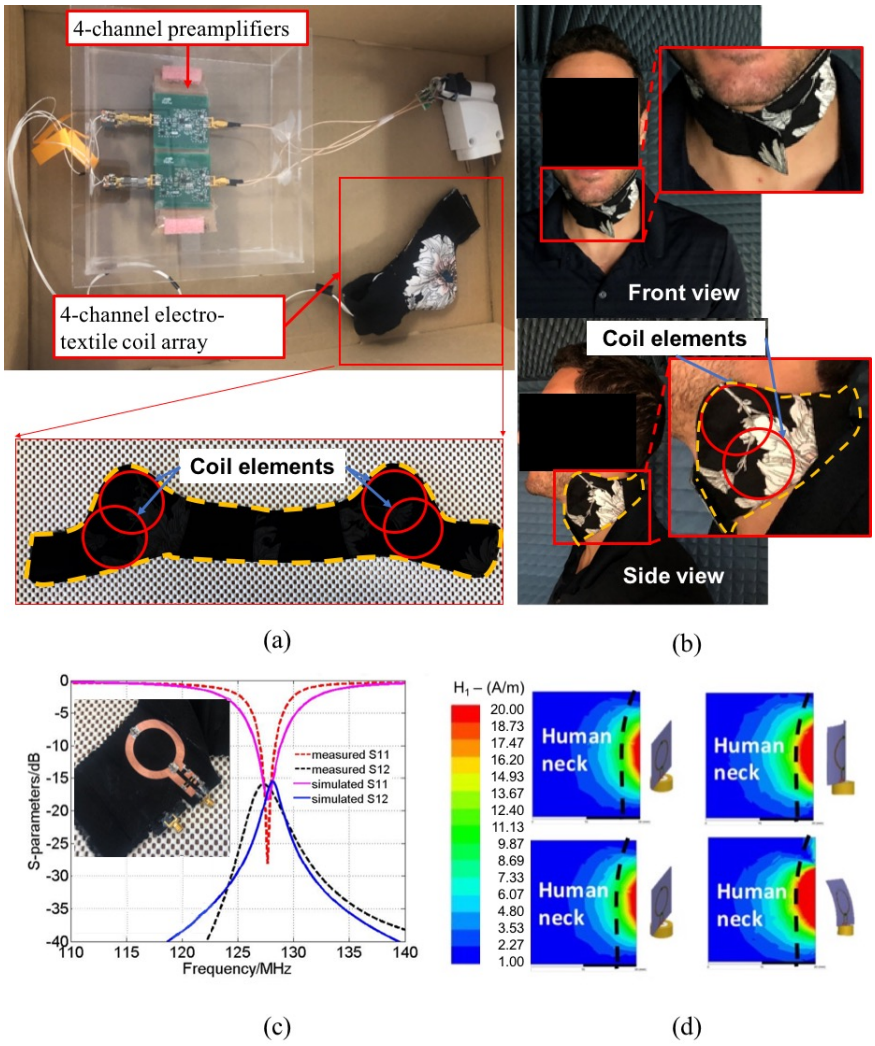

Figure 3.41: Ultra-flexible electro-textile RF coil array (a) The 4-channel e-textile coil array includes 4 elements and preamplifiers. In the close-up figure, the coil array contains 2 elements on each side. (b) The model wears the e-textile coil around the neck.

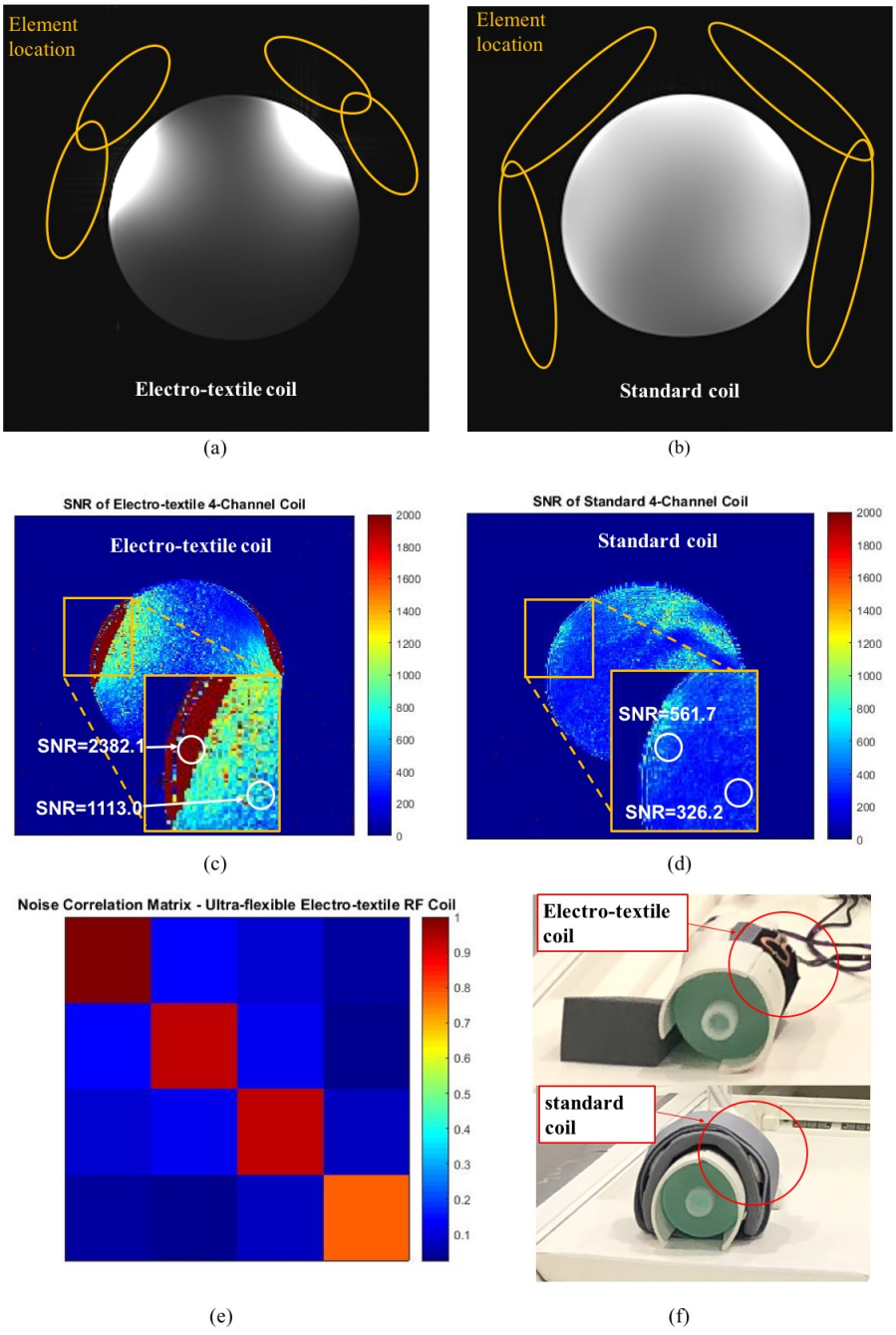

Figure 3.42: The electro-textile RF coil performance on a water phantom (a) Image acquired using the 4-channel electro-textile coil array. (b) Image acquired using a 4-channel standard coil array. (c) The SNR map of the phantom image for the ultra-flexible electro-textile coil (d) The SNR map of the phantom image for the standard coil. (e) The Noise Correlation Matrix (NCM) of the electro-textile coil wrapped around the phantom. (f) The scanning setup of the ultra-flexible electro-textile coil array and standard coil array.

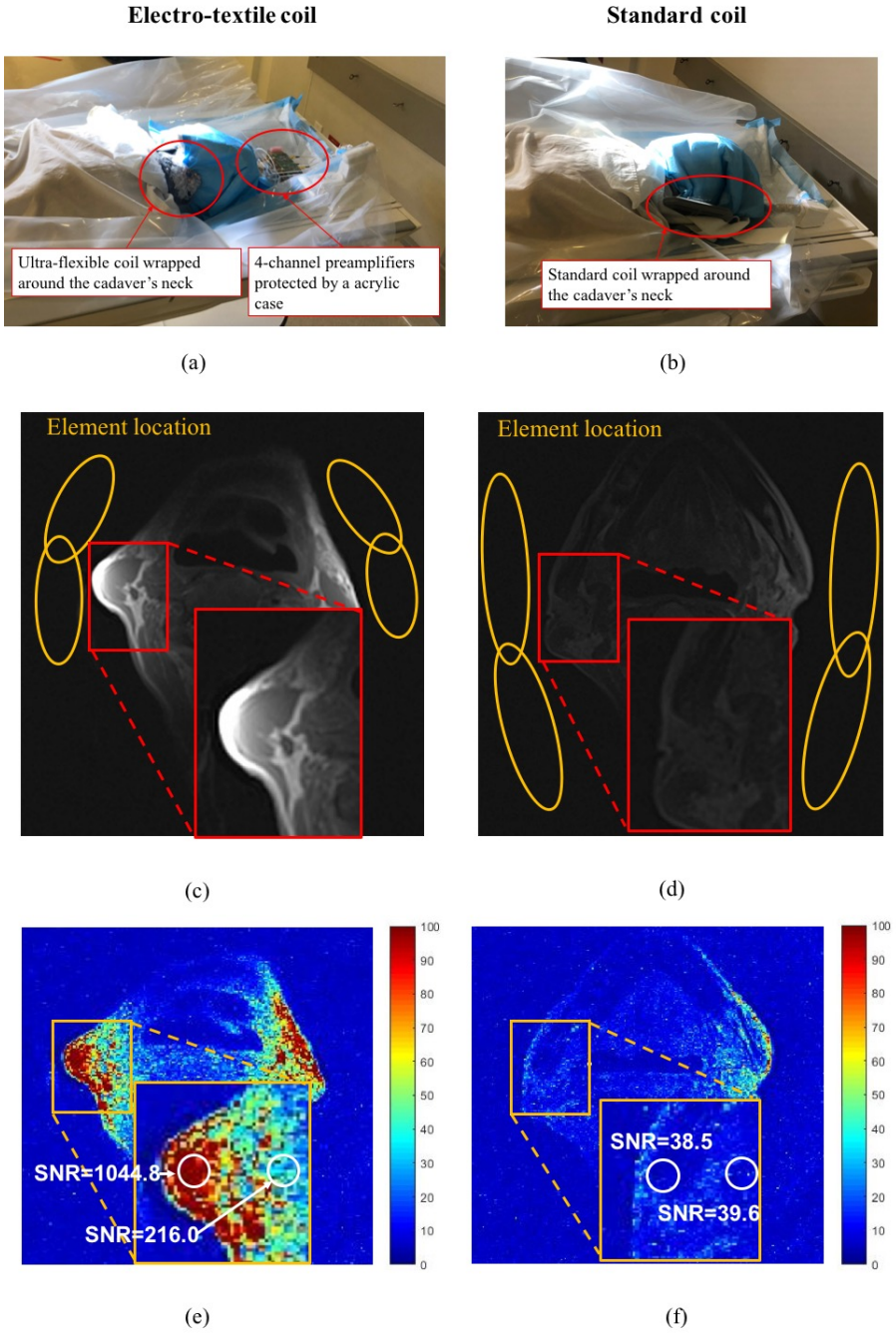

Figure 3.43: The electro-textile coil performance for cadaver neck MRI in comparison with a standard surface coil. (a) The scanning setup of the electro-textile coil array. (b) The scanning setup of the standard coil array. (c) An image of the neck using electro-textile coil. (d) An image of the neck using standard coil. (e) The SNR map of the neck using the electro-textile coil. (f) The SNR map of the neck using a standard coil.

Depth	Water phantom		SNR ratio	Cadaver		SNR ratio
	E-textile coil SNR	Standard coil SNR		E-textile coil SNR	Standard coil SNR	
0.5 cm	2382.1	561.7	4.2	1044.8	38.5	27
3 cm	1113.0	326.2	3.4	216.0	39.6	5.5

Figure 3.44: Signal-to-noise ratio (SNR) comparison between the ultra-flexible e-textile and standard coils when imaging phantom and cadaver at the depths of 0.5 cm and 3 cm from the surface of imaging area. The e-textile coil achieved multi-fold improvement in SNR compared to a standard coil.

CHAPTER 4

Novel Ultra-Wideband Antenna Design Potentially Integrated with Electro-textiles

In this chapter, a novel topology of top-cross-loop(TCL) will be proposed to increase the bandwidth of the original UWB planar monopole antenna. We designed, characterized and measured to confirm the good performance in both frequency domain and time domain. The system fidelity figure (SFF) is used to quantitatively characterize the performance of the UWB antenna with TCL in the time domain. The simple single-layer structure of the UWB planar monopole with TCL makes it a good candidate for the integration with electro-textiles. The simulated and measured S-parameter performance of the UWB antenna as an initial performance evaluation shows its potential to be used in wide frequency bandwidth.

4.1 Motivations and challenges

In 2002, Ultra-Wideband (UWB) began to draw the attention of numerous researchers because the Federal Communication Commission (FCC) allocated 3.1 GHz to 10.6 GHz for short-range communication. Since then, other areas around the globe have generated regulations for UWB, including Europe, China, Japan, Korea and Singapore [67]. Despite the huge academic interest in UWB, worries have been expressed on the current situation of UWB in [68] partly due to the fact that UWB is competing against Wi-Fi (IEEE802.11) for indoor short range high throughput

communication and also because of standardization gridlock [69]. However, niche markets have been found in various fields especially the millitary [70] and the bio-medical application. Additionally, the UWB technology has large potential in the short-range and high-throughput communication once industries begin to develop a coherent method and work in collaboration for greater good. UWB communication systems possess advantages: robustness against multi-path and jamming, comparatively low power consumption, and high data rate capability (typically 100 Mbps) over short range. These characteristics, among others, make UWB systems promising solutions for the prevalent applications mentioned above.

The qualified UWB units in recent development usually require several characteristics. First of all, low-profile is desired to fit the needs of portable devices. Secondly, omnidirectional radiation in the azimuth plane is also required for devices communicating with several targets at the same time. Lastly, a constant phase center throughout the frequency is desired for impulse radio systems. The monopole antennas meets all these requirements stated above. Conventional monopole antennas, however, suffer from the volumetric disadvantage and are not easy to fabricate for the mass production. As a result, research focus is on the evolution of planar monopole antennas.

In [71], a novel tab monopole antenna is proposed to achieve more than 50% S_{11} bandwidth at the center frequency of 2.6 GHz. Besides the mentioned planar category, a volumetric UWB mono-cone antenna with new topology in [72] has bandwidth from 3.06 GHz towards over 12 GHz. The new topology increases its bandwidth substantially by employing a top-cross-plate. Some other design examples include [73] [74] [75].

Inspired by the simple element shape of the tab antenna proposed in [71] and the new topology introduced in [72], a novel topology of Top-Cross-Loop (TCL) is proposed for the CPW-fed Ultra-wideband (UWB) planar monopole antenna. A

prototype is designed, fabricated and measured to confirm that it has the novel characteristics required by mobile UWB devices. TCL helps to increase the bandwidth by 1.71 GHz compared with the antenna of the same dimension without TCL. The satisfactory omnidirectional radiation pattern in the azimuth plane is achieved in the proposed design using TCL. Additionally, the quantitative analysis - the system fidelity factor (SFF) - in the time domain is also used to characterize its novel performance. The topology is convenient for the mass production because it is single-layer and easy to fabricate.

The proposed TCL topology can potentially be applied to the planar monopole antennas with shapes other than triangular. The fabricated prototype doesn't intend to beat all the other planar UWB antennas in bandwidth. It serves as an additional method to further increase bandwidth. For example, the new topology of TCL may potentially be applied to elliptic-card shaped element utilized in [76].

Meanwhile, the printed slot antenna that is another type of the planar antenna also catches the attention of the researchers as a compact broadband antenna. Various methods have been used to improve its bandwidth. A tulip-loop UWB antenna is proposed in [77] and [78] with bandwidth of 83% in X-band targeted for linear array application. Although our novel monopole antenna with TCL share similarities in appearance with the tulip antenna, the performance, radiation mechanism and design strategy of the two are different.

The tulip antenna does not cover much of the frequencies in the FCC specified bandwidth in the lower end, that are actually preferred frequencies in many countries [79]. Our novel monopole antenna with TCL on the other hand covers the lower end of UWB bands.

Since the main radiator of tulip-loop antenna is the loop antenna, the design starts with the outer dimension of the loop with the size of $\lambda_g/2$. The proposed antenna with TCL however does not have this requirement for TCL size. In final

design, the outer dimension of TCL is different from the size requirement specified in [78]. The triangular shaped radiator is regarded as the main radiator and its dimension determines the dominant resonant frequency. As a result, the dimension of the triangular shaped radiator is determined before the size of TCL. In our analysis, several parameters including the TCL thickness and the distance between the TCL and the radiating element are co-designed to achieve the compact size of 30 mm$\times$55 mm and 91% bandwidth with the center frequency at 6.29 GHz. It is measured that 1.71 GHz of bandwidth is obtained using the TCL. The radiation pattern exhibits the good characteristics throughout the frequency with the low cross-polarization level.

4.2 A Novel topology of UWB antenna

4.2.1 Design of UWB antenna with the novel topology

The proposed antenna is shown in Fig. 4.1. TCL connecting two portions of CPW ground above the triangular shaped main radiator serves as capacitive loading between the main radiator and the ground. It helps to increase bandwidth especially at low frequencies. Design parameters of top view and side view are in Fig. 4.2 and Fig. 4.3 respectively, along with the coordinate system used in this paper. The table I and table II lists all the values of parameters in Fig. 4.2 and Fig. 4.3. The antenna is etched on Rogers 5880 and connected to 50Ω edge mount SMA port shown in Fig. 4.1, and the SMA detailed specifications can be found in [80]. As shown in Fig. 4.1, CPW feeding method facilitates multi-modes and helps to increase bandwidth. Additionally, single layer layout is in favor for mass production because of simplicity and cost reduction.The length of triangle side pointing up right (or up left) is about quarter wave length of the dominant resonant frequency, which is around 5.21 GHz in the design without TCL, which can be seen in Fig. 4.10.

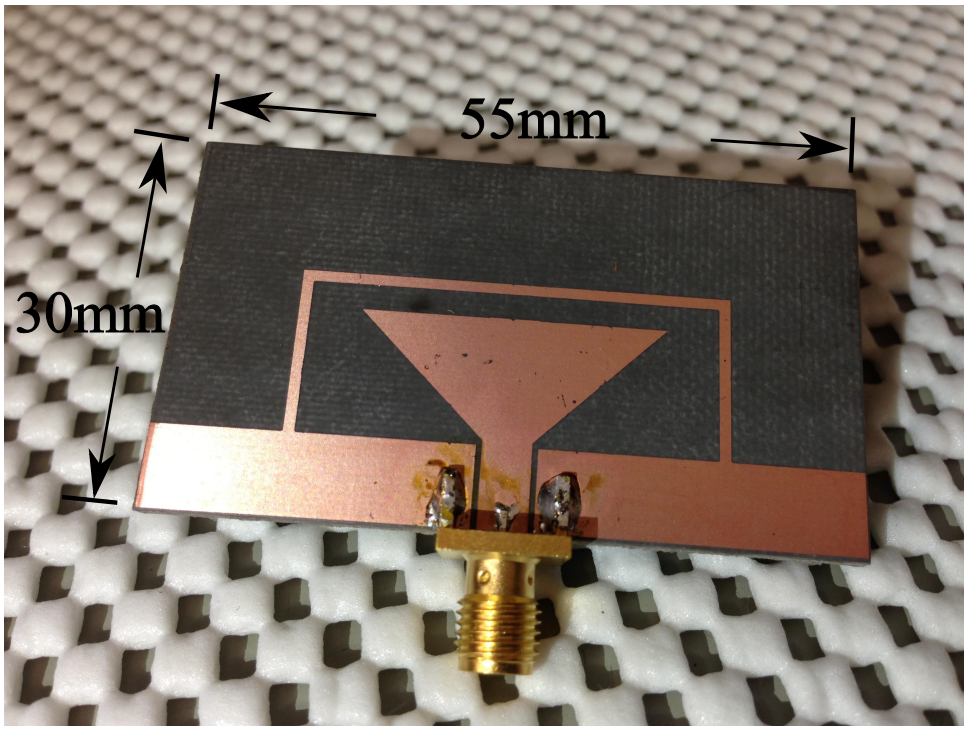

Figure 4.1: Close view of the fabricated antenna.

During the design process, w_t and g are the first two parameters determined to fix the characteristic impedance of 50Ω assuming CPW is lossless. Initial values of different parameters are chosen to examine antenna property preliminarily. The h_1, h, L_1 and α are swept to find the optimal performance. w_1 and w_2 are then swept along with the above three parameters to get optimal values. As is found in [72] that smaller thicknesses of the four legs help to expand bandwidth, a similar trend is also true for our proposed antenna. We find 1mm is appropriate considering fabrication accuracy. More detailed discussions can be found in the parametric study in Section 4.2.2.

4.2.2 The effect of the key parameters

The effect of key parameters are critical for the antenna design that we proposed. As a result, a parametric study is conducted in this section to further understand

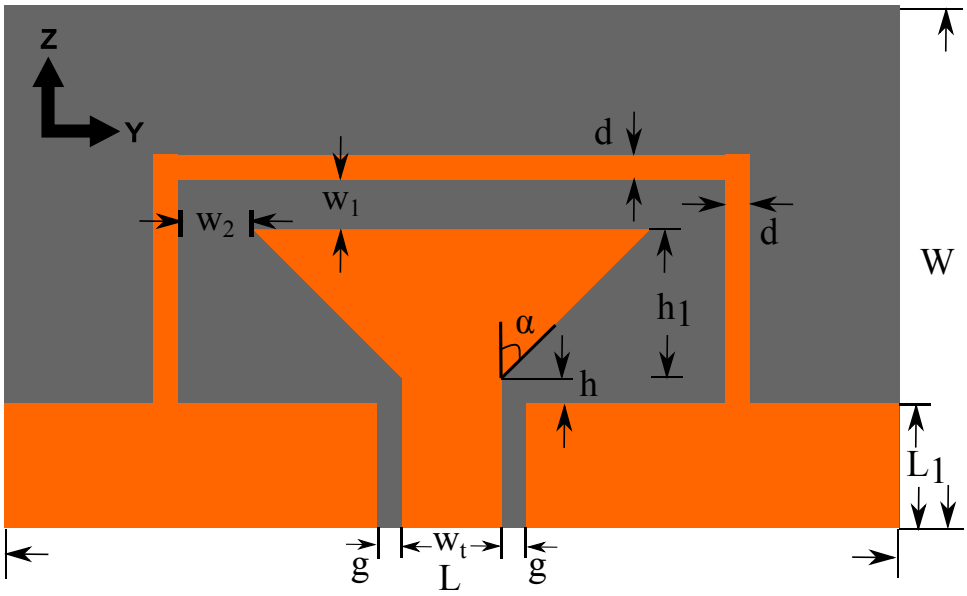

Figure 4.2: Top view of the proposed antenna.

Figure 4.3: Side view of the proposed antenna.

Table 4.1: Parameter Values of the Proposed Antenna with Top View

parameter	L	W	w_t	g	L_1	d
Value/mm	55	30	4	0.33	6.5	1
parameter	h	h_1	α	w_1	w_2	
Value/mm	0.3	10	46°	2	2	

Table 4.2: Parameter Values of the Proposed Antenna with Side View

parameter	H	ϵ_r	tanδ	H_1
Value	1.575mm	2.33	0.0009	1.55 μm

their effects. Only one parameter will be swept in each following section with the values of the others fixed as listed in Table 4.2.

4.2.2.1 Effect of Triangle Angle

One of the key parameters is the triangle angle α that contributes to the wide bandwidth of the antenna. As seen in Fig. 4.4, the bandwidth is largest when α=46° especially at upper frequencies.

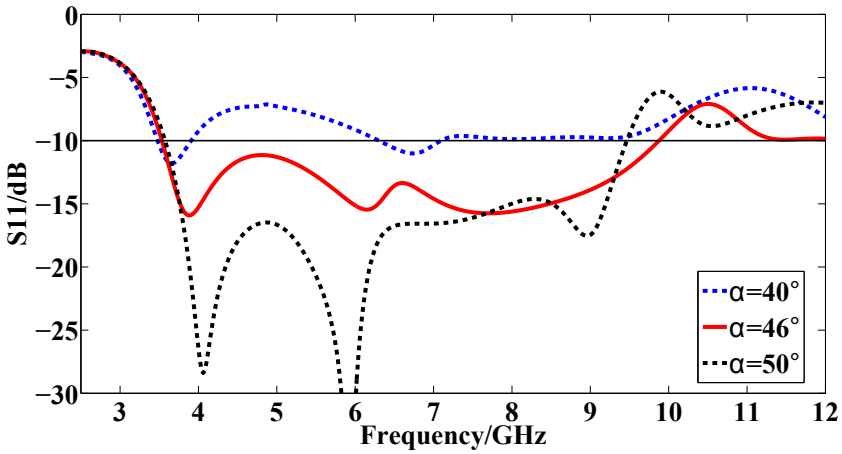

Figure 4.4: The effect of Triangle Angle α.

4.2.2.2 Effect of Feeding Length

Another important parameter is the feeding length L_1. It is shown in Fig. 4.5 that feeding length influences reflection coefficient in both lower and higher frequencies. 6.5 mm is chosen to balance performance in both frequency ends, as well as antenna size and radiation interference by the transmission line.

4.2.2.3 Effect of Gap Width

Gap width ratio is defined as the ratio of the TCL inner length and the triangular monopole length in z direction. This parameter helps to set the gap width between triangular monopole and TCL. It is shown in Fig. 4.6 that gap width ratio has some effect on first resonant frequency thus changing the reflection coefficient at

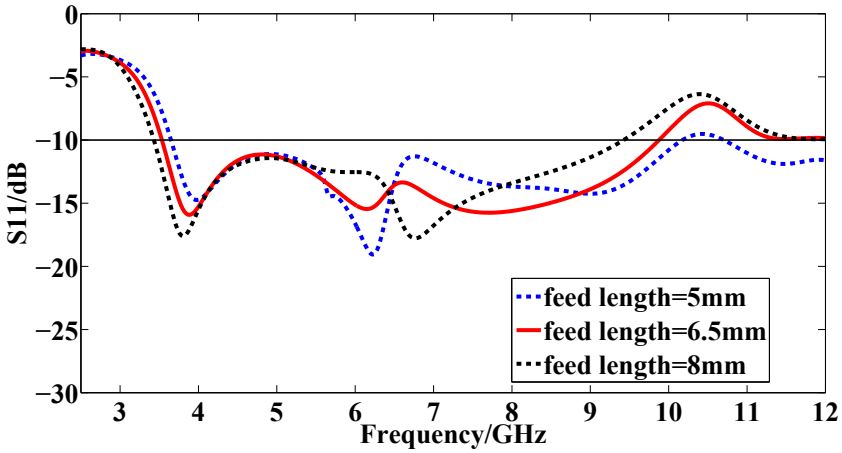

Figure 4.5: The effect of feed length L_1.

lower frequency. This is within what is expected because smaller gap means higher parasitic capacitance between main radiator triangle and TCL, which has larger impact especially at low frequencies. Since the main purpose of this section is to gain insight into the role each critical parameter plays, gap ratio of 1.2 is chosen and additional improvement may be made with smaller gap ratio.

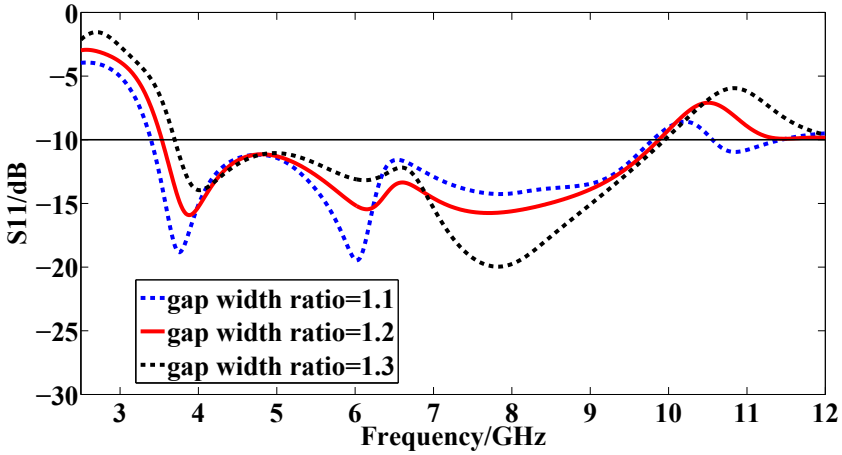

Figure 4.6: The effect of gap width.

4.2.2.4 Effect of Transition Length

The effect of transition length h is not significant for reflection coefficient bandwidth as is shown in Fig. 4.7, except for minor influence on middle frequency around 5 GHz. 0.3 mm is selected to have higher isolation between radiation and transition part compared with transition length of 0.1 mm, and to have lower reflection around around 5 GHz compared with transition length of 0.5 mm.

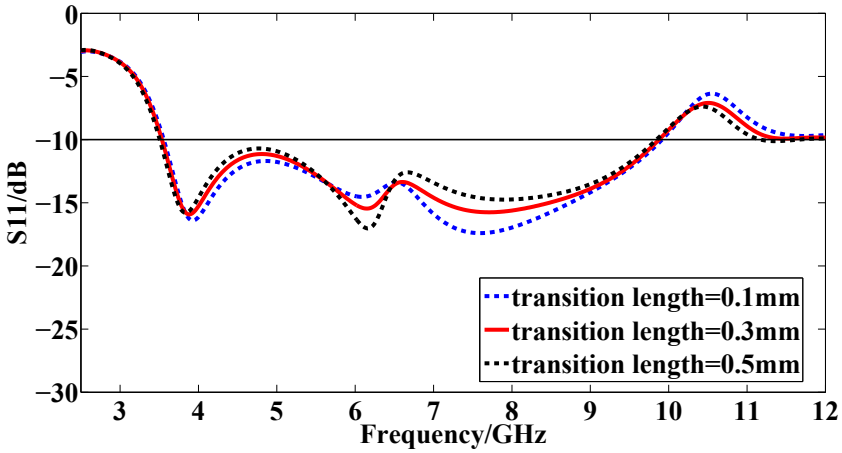

Figure 4.7: The effect of transition length h.

4.2.2.5 Effect of Loop Width

It is observed in Fig. 4.8 that the increase of loop width slightly helps to reduce S_{11} at the higher frequencies but at the same time has less preferred performance in the middle frequency near 5 GHz. Since the error for fabrication process we use is about 5 mil ($0.127mm$), we choose loop width of 1 mm to guarantee controllable and excellent performance.

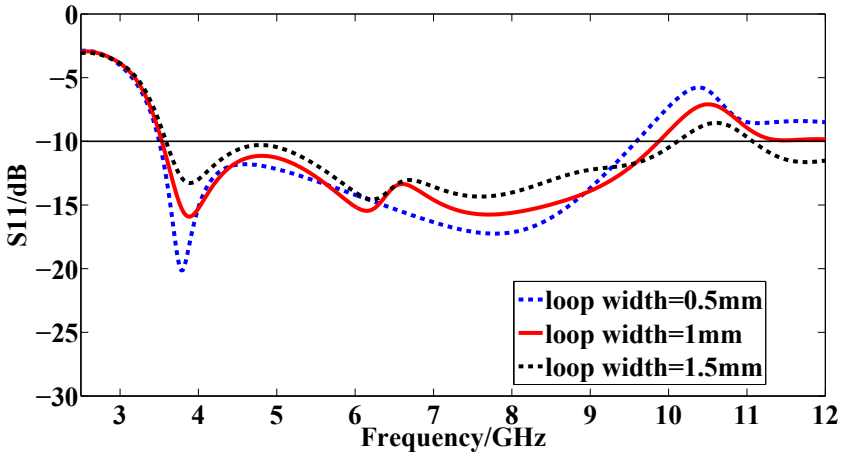

Figure 4.8: The effect of loop width.

4.2.3 Performance of UWB antenna with the novel topology

The proposed antenna is analyzed, fabricated and measured at UCLA Antenna Research, Analysis and Measurement Lab (ARAM). High Frequency Structure Simulator (HFSS) is used for simulation. The performance of the fabricated antenna in the frequency and the time domain are measured in comparison with the simulation results. Additionally, an antenna without TCL is also fabricated and measured for comparison. In the frequency domain, the performance parameters such as reflection coefficient, radiation pattern, current distribution will be shown. In the time domain, system fidelity factor (SFF) will be used to characterize the low dispersive characteristic of the antenna.

4.2.3.1 Frequency Domain Behavior

The S_{11} of the fabricated antenna was measured with the radiation absorption material placed below the back side to prevent possible radiation interference caused by reflection from the ground. The antenna of the same size without the TCL in Fig. 4.9 has the bandwidth from 4.44 GHz to 8.44 GHz as shown in Fig. 4.10. The

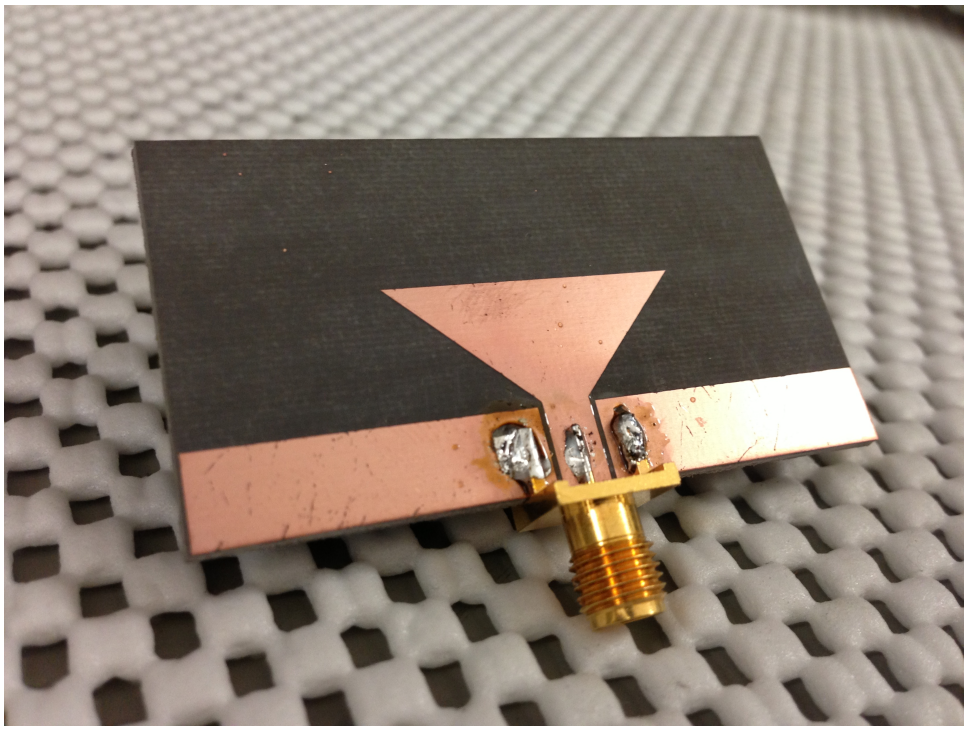

Figure 4.9: Antenna of the same dimension but without TCL.

measured S_{11} bandwidth of the antenna with the TCL was from 3.43 GHz to 9.14 GHz as shown in Fig. 4.10, 1.01 GHz increase at the lower frequencies and 0.7 GHz increased at the higher frequencies. Although the benefit for the lower frequency is more significant, it is still worthy of further study to uncover the reasons behind the bandwidth increase for higher frequencies. It can be further observed that the number of resonant frequencies increased from 3 to 5, with one additional at lower frequencies and the other at higher frequencies. Alternatively, this implied the implementation of the TCL creates two additional resonant frequencies. By comparing the simulated and the measured performance of the antenna with the loop, we can see that a good agreement was achieved in terms of bandwidth and first resonant frequency.

The simulated and the measured radiation pattern of the proposed antenna with the TCL in the x-y and the y-z plane at 4 GHz, 8 GHz and 11 GHz is presented

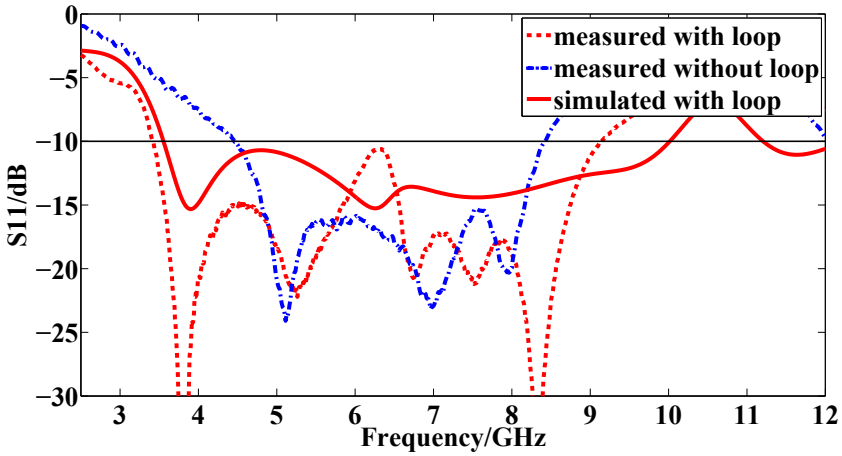

Figure 4.10: S_{11} comparison with and without TCL.

in Fig. 4.11 and Fig. 4.12. These three frequencies were at the edge of the S_{11} bandwidth to represent the worst scenarios according to the simulation results in our parametric studies shown in section III. As is shown in Fig. 4.11 and Fig. 4.12, the radiation pattern at 4GHz was similar to the antenna presented in [72]. It radiated omnidirectionally and was vertically polarized in the x-y plane with the cross-polarization field at least 10 dB lower than the co-polarization. The maximum total gain at 4 GHz was simulated to be 1.25 dB. The radiation pattern at 8 GHz had two main lobes in the y-z plane with about 80° departing from each other. This feature makes it good a candidate as a short-range communication port that may be potentially installed at elevated positions to communicate dual targets downwards, which finds wide application scenarios in indoor athletics and medical area. However, at 11 GHz, the radiation pattern and the polarization status were different from other frequencies. It was observed that it was not strictly omnidirectional in the x-y plane. Although in most directions the antenna was linearly polarized in the x-y plane, the cross-polarization field level was comparable with the co-polarization field at certain angles. It was also shown that more lobes were created in the y-z plane at 11 GHz and possessed a change of maximum direction compared with 8

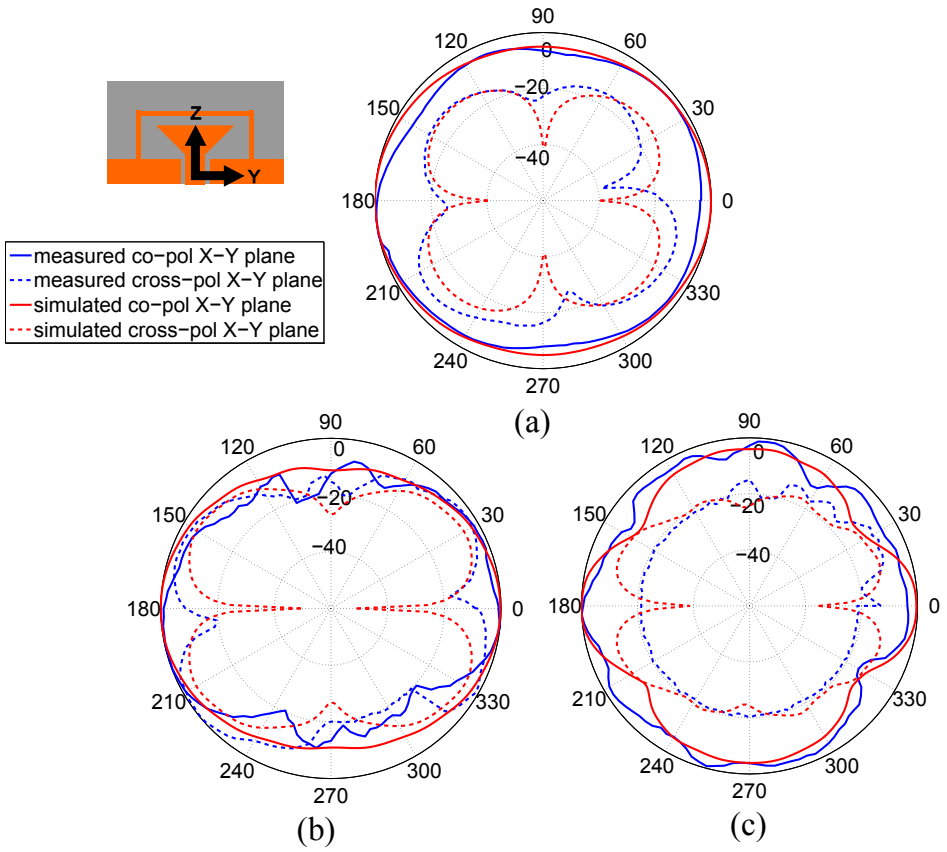

Figure 4.11: Measured and Simulated radiation pattern in X-Y plane: (a) 4 GHz (b) 8 GHz (c) 11 GHz.

GHz. The total gain were simulated to be 3.92 dB and 7.32 dB at 8 GHz and 11 GHz respectively.

The current distribution is given in Fig. 4.13 with the input power of 1W at three different frequencies to provide insights into antenna operation. As can be seen from Fig. 4.13a, a large amount of current was concentrated on lower portion of triangle radiator, two sides of TCL and its surrounding area in ground plane of CPW, which was similar to the current distribution described in [72]. At middle and higher frequencies (8 GHz and 11 GHz), more currents flowed on the side edges of the triangle radiator and onto the top edge. The currents on the top edge is coupled to TCL. These characteristics suggested that the TCL played an important

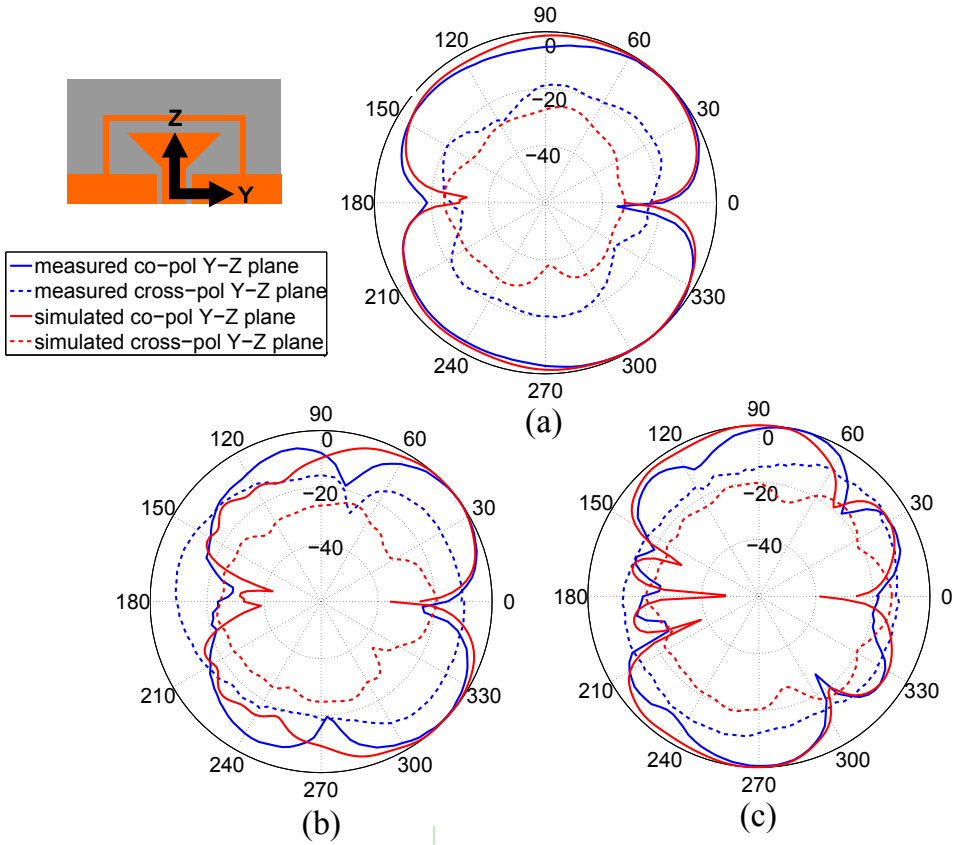

Figure 4.12: Measured and Simulated radiation pattern in Y-Z plane: (a) 4 GHz (b) 8 GHz (c) 11 GHz.

role for the antenna operation throughout the frequencies. The characteristics of the currents also shed light on the explanation of its bandwidth improvement in both the higher and the lower frequency ends.

Since the proposed antenna can potentially be a candidate in the communication systems near or on the human body, the variations of radiation characteristics near or on human body were also studied and measured. As can be seen in Fig. 4.14 the large bandwidth characteristic was still preserved when antenna was placed near or on the human forehead. There is no large change of reflection coefficient when antenna was placed near the human head. The bandwidth increases hugely, however, when our antenna was placed on the human head. This is reasonable because the human

head is the lossy loading at the operational frequencies of our antenna. When placed on a human head, the antenna system had smaller quality factor, which resulted in the increase of the S_{11} bandwidth. The radiation characteristics near human head were also simulated and shown in Fig. 4.15. The important radiation signature was preserved while the radiation peak occurred in the x direction away from the human head. This is also expected because part of the radiation power in -x direction is absorbed by the human head.

4.2.3.2 Time Domain Behavior

The time domain behavior is critical for UWB antennas. Two identical antennas were placed 30 cm away from each other, with one for transmission (Tx) and the other for reception (Rx). Two antenna arrangement scenarios were considered: face to face and side by side [81]. 5th derivative of Gaussian function in [82] [83] was used to generate UWB signal from 3.1 GHz to 10.6 GHz. In order to get receiving signal in the time domain, the transfer function in the frequency domain was obtained as shown in (4.1)

$$R_x(t) = IFFT\left(FFT\left(T_x\right) \times S_{21}\right) \tag{4.1}$$

Where S_{21} was the transfer function for the antenna system; IFFT and FFT stands for the Inverse Fast Fourier Transform and the Fast Fourier Transform. When the separation distance was 30 cm ($10\lambda_0$ at high frequency), getting transfer function directly from HFSS was time consuming. As a substitution, a method was introduced in [81] as follows. We assumed that the channel was free space. The two antennas had the identical gain, the reflection coefficient and there is no polarization loss between the two antennas. So Friis transmission equation can be reduced to:

$$|S_{21}| = \left|\frac{V_{Rx}}{V_{Tx}}\right| = \left(1 - |S_{11}|^2\right) \frac{\lambda}{4\pi r} G_A \tag{4.2}$$

$$\angle S_{21}(\omega) = 2\Phi_{Tx} - \frac{\pi}{2} - kr \tag{4.3}$$

It is noted that in HFSS, Φ_{T_s} is the angle of the transmitted far field parameter rE, so the phase of S_{21} can be calculated accordingly. The magnitude of S_{21} can also be calculated with (4.2). Similarly, we can measure the phase and the magnitude of S_{21} with a vector network analyzer (VNA). The simulated and measured S_{21} in magnitude and phase in the azimuthal plane in the x (face to face) and the y (side by side) directions are shown in Fig. 4.16(a)(b) and Fig. 4.17(a)(b). The linearity of the phase throughout the operating frequency is critical for UWB antenna performance to guarantee its non-dispersive characteristic. The phase linearity was preserved throughout the frequencies, although the measured phase deviated from the simulation value at certain frequencies. It was observed in Fig. 4.16 and Fig. 4.17 that the simulated and measured S_{21} agreed well in terms of both the magnitude and the phase. The magnitude dips and the phase non-linearities are found in the two frequency regions. The linearity in the y direction was more severe. This was caused by the sudden drop of the antenna gain in these frequencies. The reasons behind it may be explained by the current cancellation by the TCL in these frequencies.

After getting the S_{21}, the FFT technique using Matlab was applied to recover the input signal with certain delay. The result in Fig. 4.16(c) and Fig. 4.17(c) was obtained by sampling input signal at 24×10^9 points/s, which was higher than twice the highest frequency of interest. It was observed that the received signal agreed with the transmitted signals well in both scenarios (face-to-face and side-by-side) in the simulation and the measurement. The distortion was mainly caused by the

nonlinearity of the S_{21} phase and the non-uniformity of the S_{21} magnitude. They can be characterized by the SFF [81] and calculated using the equations from (4.4) to (4.6).

$$r_x(t) = \frac{R_x(t)}{\left[\int_{-\infty}^{+\infty} |R_x(t)|^2 \, dt\right]^{1/2}} \tag{4.4}$$

$$t_x(t) = \frac{T_x(t)}{\left[\int_{-\infty}^{+\infty} |T_x(t)|^2 \, dt\right]^{1/2}} \tag{4.5}$$

$$SFF = max \int_{-\infty}^{+\infty} t_x(t) \, r_x(t+\tau) \, dt \tag{4.6}$$

The SFF effectively compared the similarity between the two signals and took into consideration the performance throughout the frequencies for both of the antennas. One of the major advantages of this parameter compared with the other methods of similar purpose was that it was easy to be measured. Both the transmitted and received signals were normalized from (4.4) and (4.5). The cross correlation of these two normalized signals were performed in the time domain in 4.6 and the maximum value of this correlation was obtained when both pulses overlap. In general SFF of over 0.5 is regarded as acceptable as discussed in [81]. The simulated SFF are 0.81 and 0.76 in the x and the y direction respectively, higher than the measured SFF of 0.68 and 0.65 in the corresponding directions. The degradation of measured results compared with the simulation may be caused by non-ideal channel situation such as the polarization mismatch and the noise. In summary both the simulated and the measured SFF were above 0.65 in the tested directions.

4.3 Flexible antennas for communication systems

The study of the effective conductivity for electro-textile patterns is not limited to the application of MRI RF coil design. This method can be applied in the UWB antenna design. It will expedite and simplify the design process of the electro-textile antennas. The UWB antenna is a perfect example demonstrating the antenna design with the proposed characterization method. The UWB systems can be widely used in many applications including body-centric network, the medical, military, entertainment and athlete field. The state of art is briefly talked about in Section 1.3.

A systematic characterization method for the electro-textiles throughout the UWB frequencies is missing in the literature. Although the UWB antenna is designed in [44], no systematic characterization of the effective conductivity is provided that can be used for rapid design. In [4], the effective conductivity above 6 GHz is not studied. A systematic approach to characterize the effective conductivity for different environmental humidity is given in [84]. Applying the method in Chapter 3, it is extracted that the effective conductivity from 3.1 GHz to 10.6 GHz is around 10^5 S/m using the conductive cloth pure copper polyester taffeta fabric. It features low DC surface resistance of $0.05\Omega/\square$.

The electro-textile UWB planar monopole with TCL is simulated in HFSS using the same dimensions of the copper antenna. It is fabricated using the conductive cloth shown in Fig. 4.18. The S-parameter of the electro-textile UWB is compared with copper UWB with and without TCL in Fig. 4.19. It can be observed that the UWB antenna performance at frequencies lower than 6 GHz and higher than 8 GHz is preserved. The frequency range is even extended from 4.44 GHz to 3.2 GHz at lower frequency end. There is one missing resonant frequency from 6 GHz to 8 GHz. The reason behind it remains to be unveiled. It should be noted, however, the UWB frequency band specified by different government agencies usually use part of

the frequency 3.1 GHz - 10.6 GHz instead of continuous bands. This electro-textile antenna structure is a promising candidate for high data rate UWB communications.

In order to study the effect of human body adjacent to the electro-textile UWB antenna, water phantom (Siemens, Germany Erlangan) is used to measure the S_{11} performance. The UWB is taped on the cylindrical water phantom along its curvature. It is observed in Fig. 4.20 that S_{11} performance of the electro-textile UWB antenna near phantom is degraded. The major resonances however is still preserved with observable shifts towards lower frequencies. The simulated and measured S_{11} of the UWB antenna with TCL using copper and electro-textile material is in Fig. 4.21. The simulated S_{11} of the UWB antenna with TCL does not capture all the resonances shown in measured values. The overall frequency bandwidth is well predicted by the simulation.

As a conclusion, the novel single UWB antenna structure of Top-Cross-Loop (TCL) is proposed, fabricated and measured to confirm its effectiveness. It is demonstrated that electro-textile UWB antenna preserves the wide bandwidth features of the novel design in both lower and higher frequency ends.

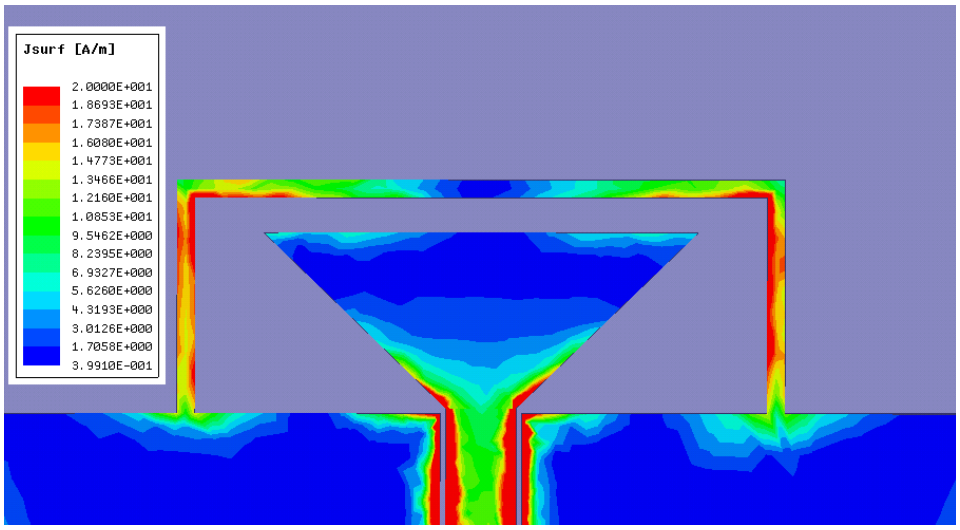

(a)

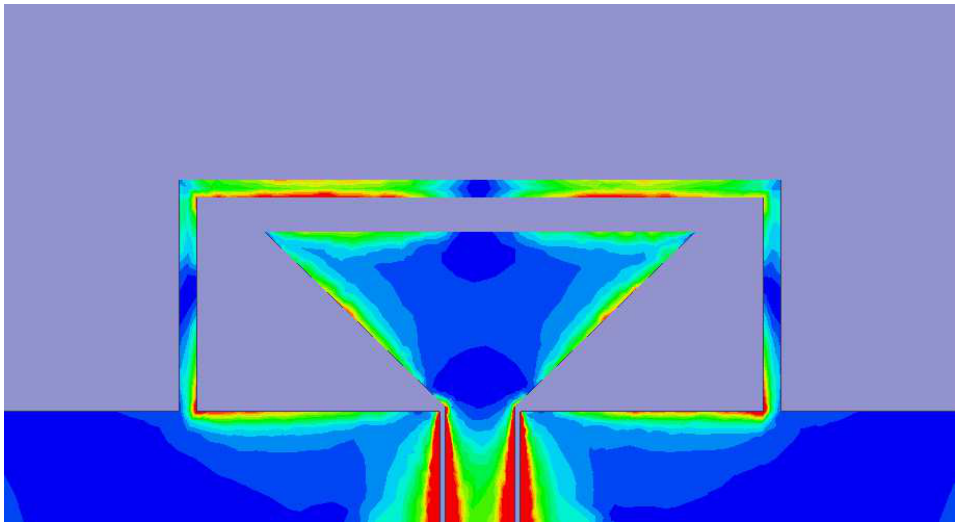

(b)

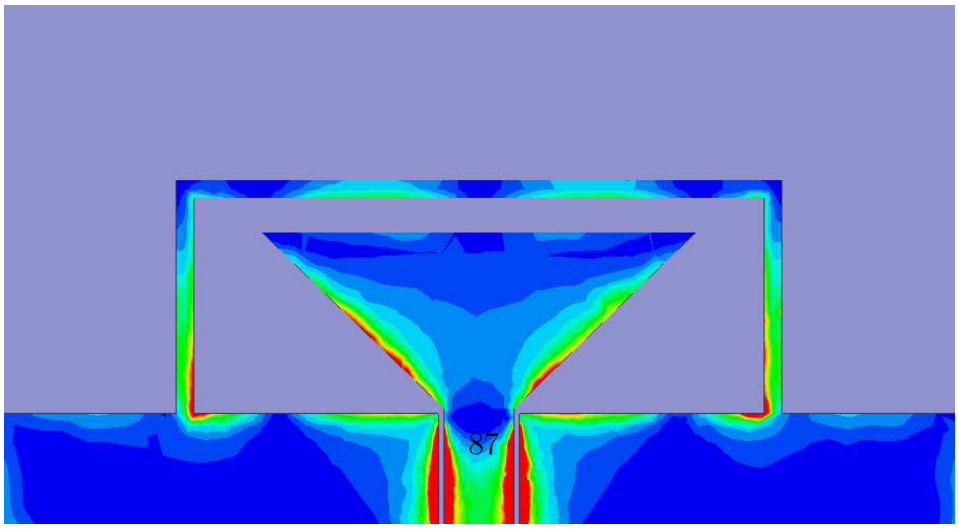

(c)

Figure 4.13: Current distribution of the antenna at: (a) 4 GHz (b) 8 GHz (c) 11 GHz.

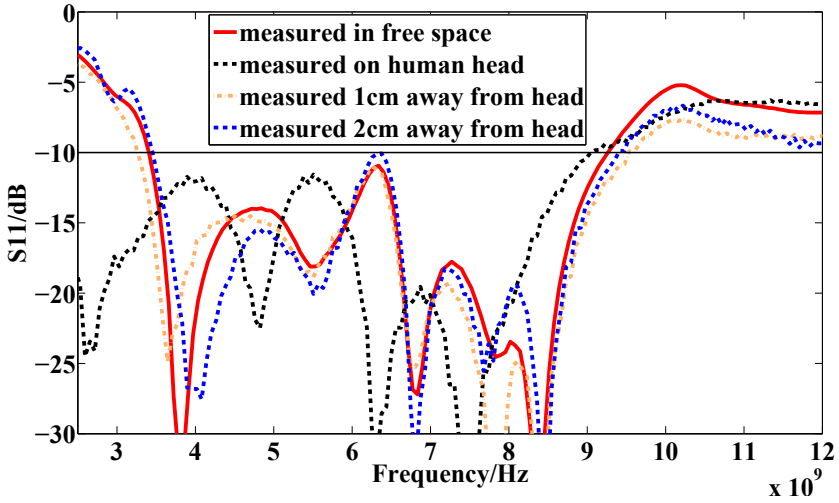

Figure 4.14: Measured S_{11} comparison near human head.

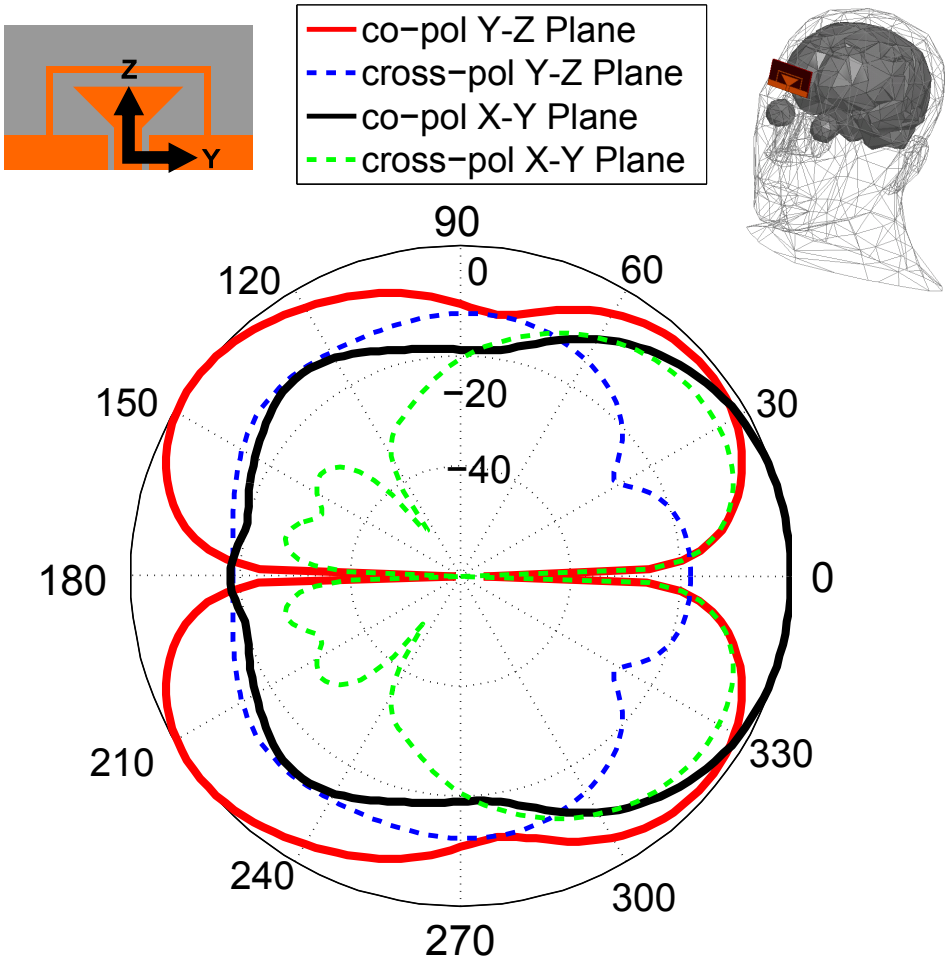

Figure 4.15: Radiation pattern near human head at 4 GHz.

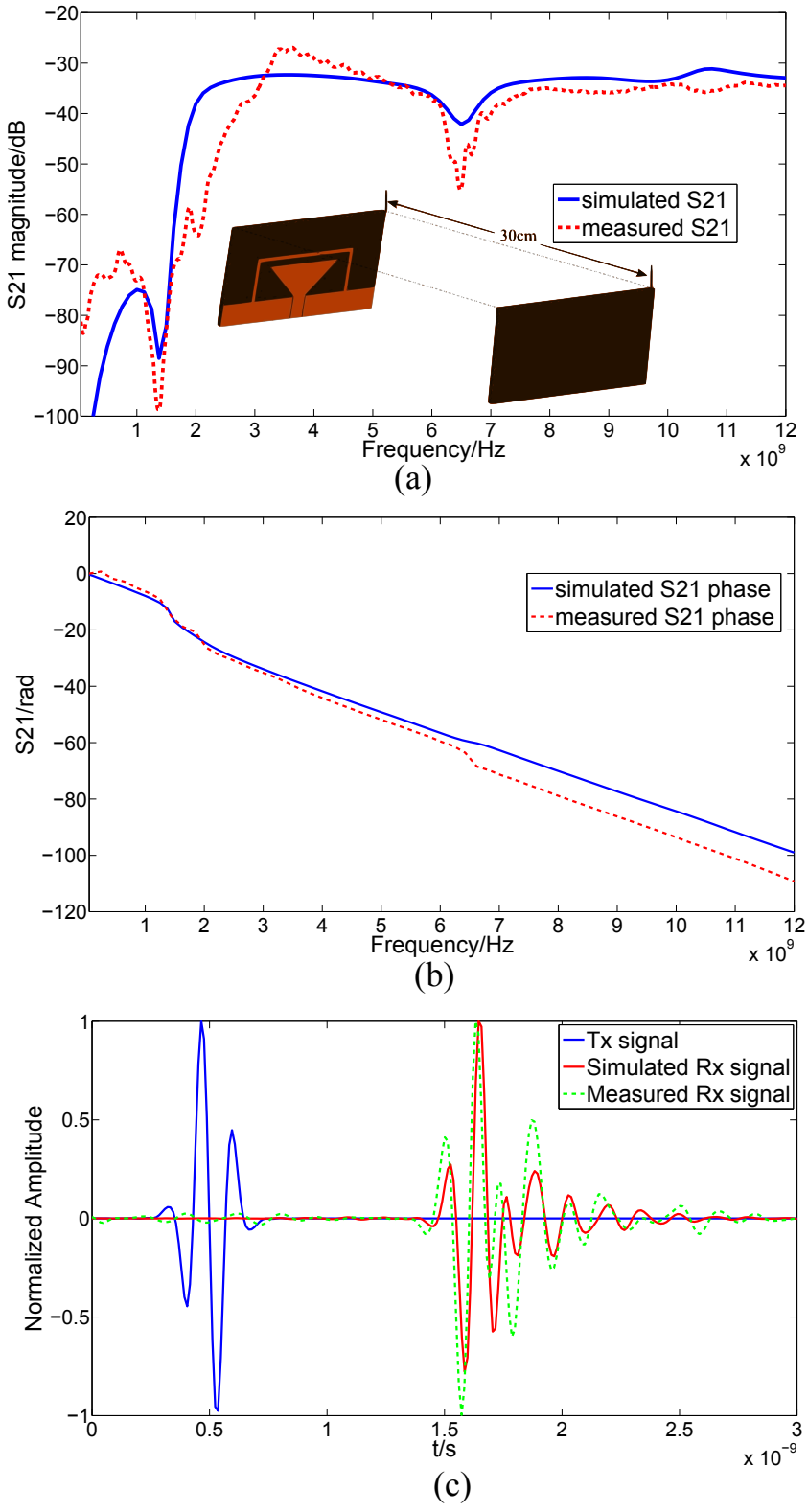

Figure 4.16: X-direction measured and simulated time domain behavior: (a) S_{21} magnitude (b) S_{21} phase (c) signal in time domain.

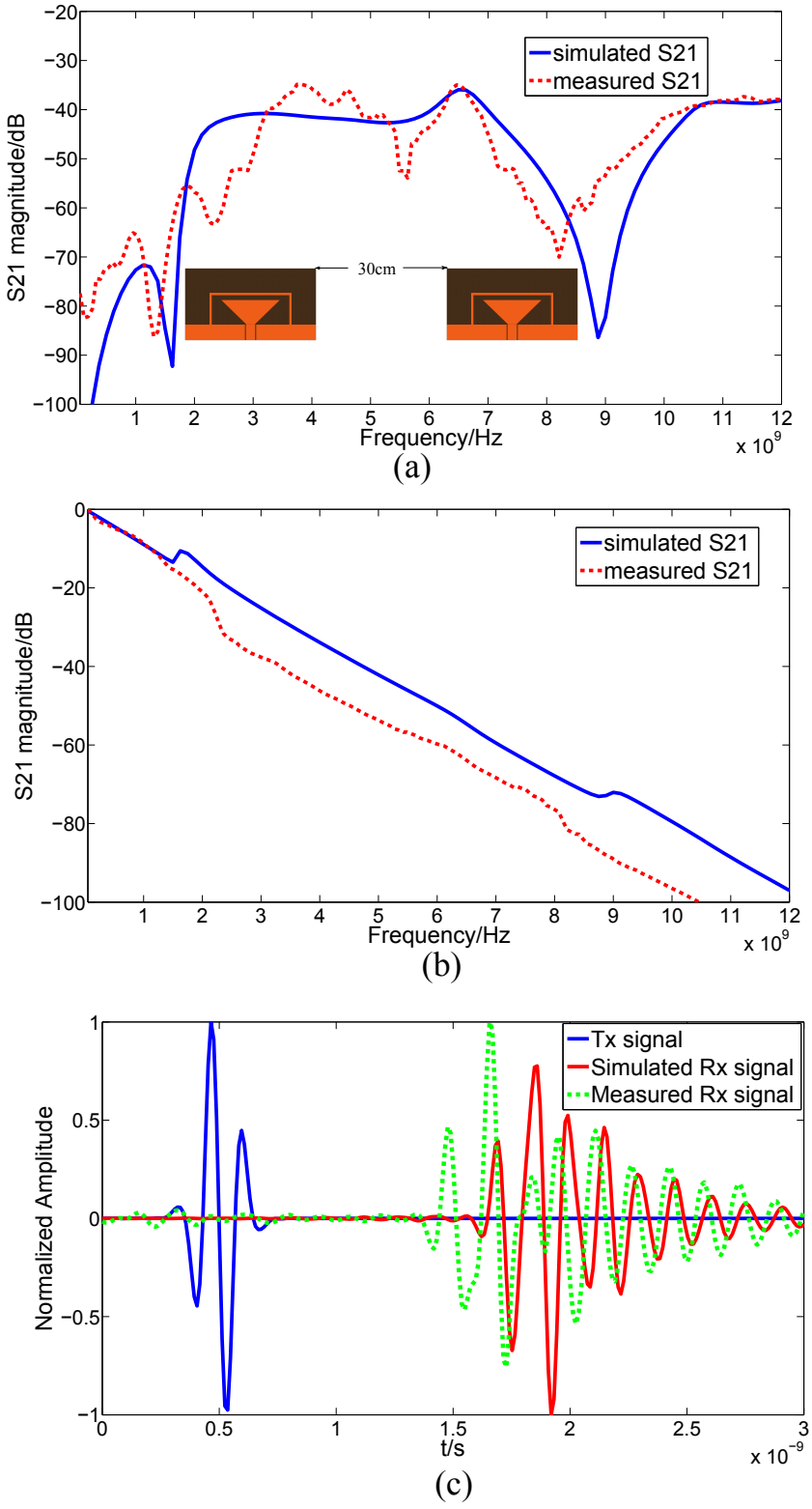

Figure 4.17: Y-direction measured and simulated time domain behavior: (a) S_{21} magnitude (b) S_{21} phase (c) signal in time domain.

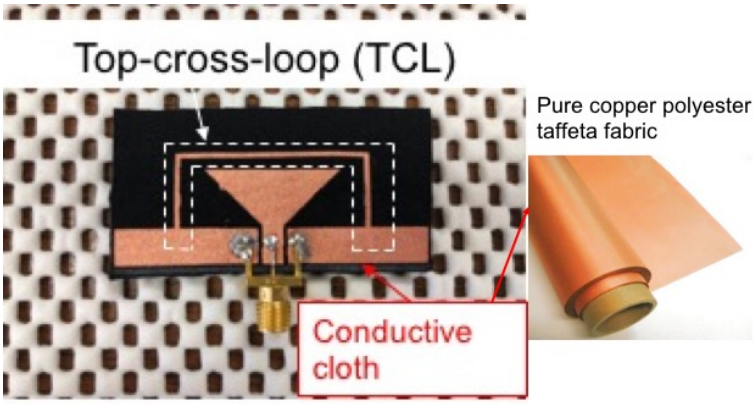

Figure 4.18: The top view of the electro-textile UWB antenna with Top-cross-loop (TCL).

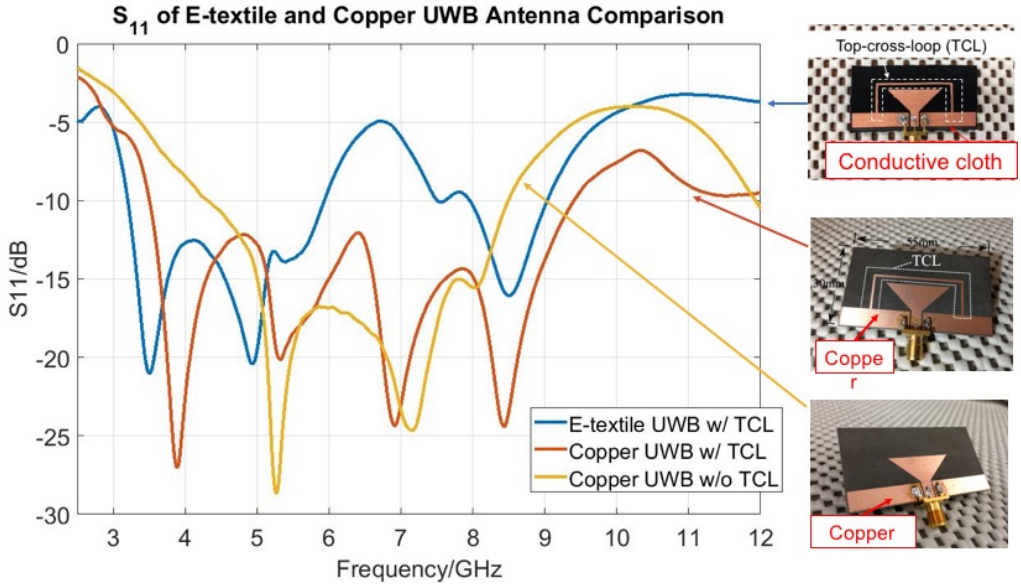

Figure 4.19: S_{11} of the electro-textile and copper UWB antenna comparison. The electro-textile UWB antenna with TCL shows good performance in both the lower and higher ends of the operating frequency. The resonance in the mid band is missing and remains to be studied.

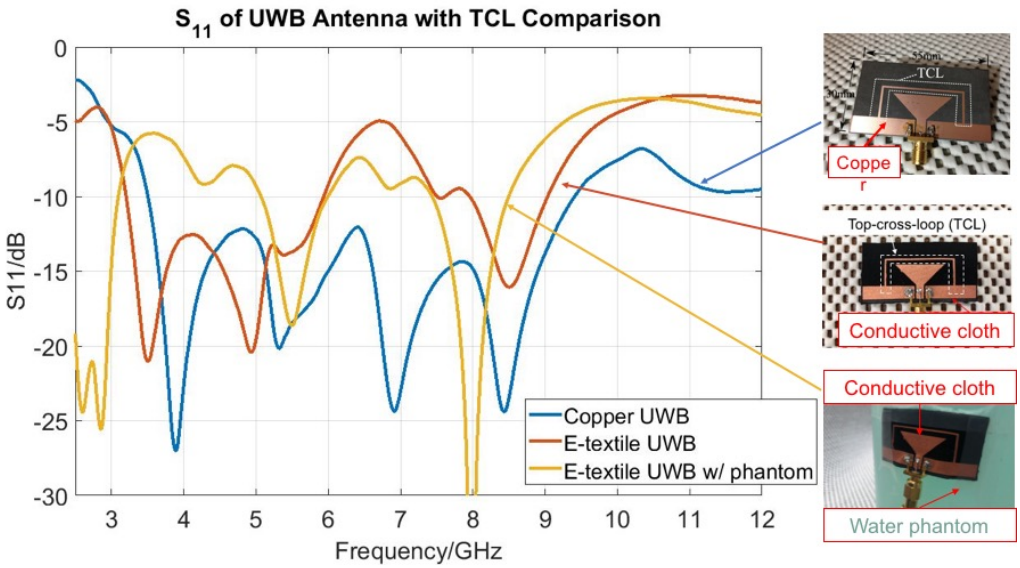

Figure 4.20: S_{11} of the UWB antenna with TCL using copper and electro-textile material. The S_{11} performance of the electro-textile UWB antenna near phantom is degraded. The major resonances however is still preserved with observable shifts towards lower frequencies.

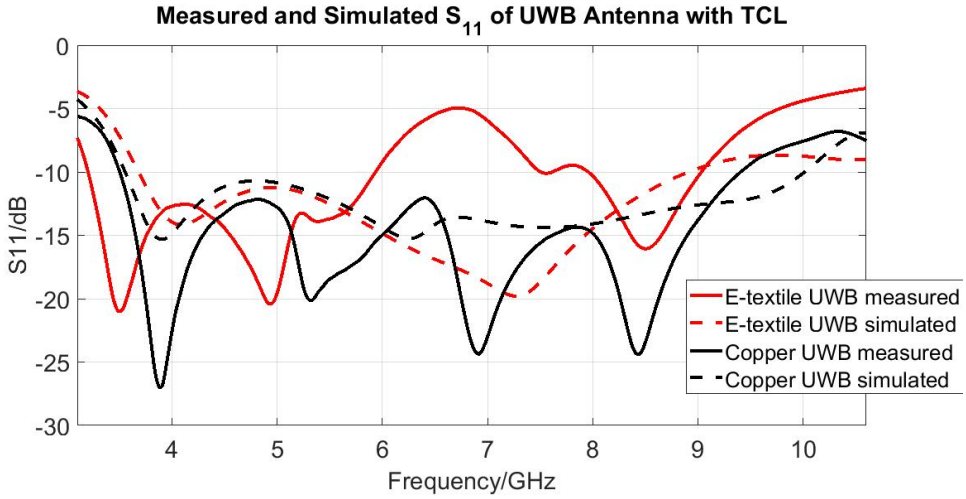

Figure 4.21: The simulated and measured S_{11} of the UWB antenna with TCL using copper and electro-textile material. The simulated S_{11} of the UWB antenna with TCL does not capture all the resonances shown in measured values. The overall frequency bandwidth is well predicted by the simulation.

CHAPTER 5

Electro-textile Patch Antenna Modeling, Design and Characterization

In this chapter, an accurate modeling method for electro-textile patch antenna is introduced, complementing the method to extract the effective conductivity of electro-textile patterns introduced in Chapter 3. In particular, three major aspects of the electro-textile complex structure is considered, including two parallel conductive layer, meander interspersing areas with high and low conductivities, and thread residues on the radiating edges. This method is further verified by designing and characterizing both regular patch and E-shape patch antennas using electro-textiles.

5.1 Introduction

The embroidered textile as a promising pathway towards the wearable communications [85] and sensing [85] applications have drawn an increasing attention. The seamless integration of electronics with ordinary clothes features versatile application contexts and are favorable especially in medical and military applications. One of the major difficulties in embroidered antenna design is the accurate modeling that leads to systematic design and optimization. The major reason is that the embroidered electro-textile antennas have complex small structures that are not well studied and as a result it expands the design cycle and leads to non-optimal designs.

In order to accurately characterize the embroidery-based antenna, several impor-

tant features need to be carefully considered. First, the conductive and dielectric material properties need to be characterized. Second, embroidered antennas generally have double-sided nature since the conductive threads form surfaces on both top and bottom of the fabric. The threads are aligned in a preferred direction and are not in perfect contact with each other along their full lengths. Finally, the embroidery pattern is not as uniform as the conventional conductive materials, especially on the bottom layer. The thread residues defined by the fabrication process also affect the structure on edges significantly. Owing to these limitations, it is not easy to define an electromagnetic model that accurately describes the properties of the embroidered antenna while maintaining a clear link with the structure of the prototype.

The methodology of material characterization and modeling strategies have been presented for embroidered textile rectangular patch antennas. A flowchart that illustrates the modeling procedures is shown in Fig. 5.1, with details discussed in the following sections. Additionally, a study on the effects of stitch density towards the accurate modeling of of embroidered textile antennas is presented since that is a critical parameter determining the material cost and fabrication time.

5.2 Material Characterization

The study of electro-textile antennas starts with the detailed characterization of the material. The accurate description of the substrate permittivity is the key to the accurate tuning of the patch antenna resonant frequency. The determination of the effective conductivity is critical for the prediction of radiation efficiency and the input impedance.

The methods to determining the substrate permittivity varies. In this paper the method of patch antenna resonant frequency matching method is utilized. We

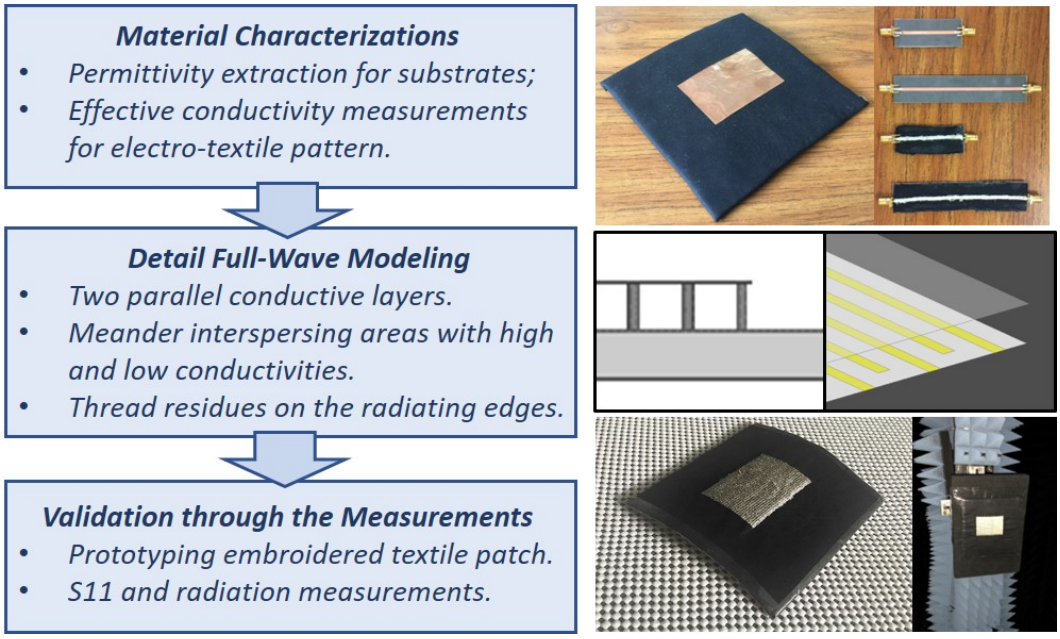

Figure 5.1: A flowchart illustrating the modeling procedures for the embroidery-based textile rectangular patch antenna.

first constructed the patch antenna using copper foil with known thickness and conductivity, and measured the resonant frequency. A full-wave simulation is then conducted in HFSS to match the measured resonant frequency by sweeping the permittivity of the substrate. Adhesive back felt fabric is used as the substrate material, and its dielectric constant is determined to be 1.2. The loss tangent is specified as 0.01.

The conductivity of the electro-textile pattern embroidered using computerized embroidery machine is not obvious even if the linear conductivity of the electro-textile threads are given. The effective conductivity depends on the stitch type, density and the measurement direction because the electro-textile patterns are anisotropic. The full wave simulation of embroidered structure is difficult because the detailed structure of embroidery are not easy to model. The effective conductivity of the electro-textile pattern can be characterized with a four-micro-strip line method proposed in [4]. The method constructs four micro-strip lines with different lengths:

two copper lines with copper on the top and bottom with two different lengths, two electro-textile lines with electro-textile pattern on the top and copper on the bottom, with the same lengths as the copper lines. The magnitude of the S_{21} are measured for each of the four cases. By assuming that the dielectric and radiation loss are the same among copper and electro-textile lines, the effective conductivity of the electro-textile pattern can be determined by comparing with the known copper conductivity. Additionally, the effect of the connectors are also canceled out during this process. For electro-textile pattern embroidered with Syscom Ag100D using running stitches, 0.8mm distance between the adjacent lines, and 5 stitch/cm, the effectivity conductivity is around 4.1×10^6 S/m around 2.5 GHz.

5.3 Full-Wave Detail Modeling

The double-sided nature of the embroidery pattern is modeled by two parallel conductive layers separated by a distance of 3mm, which is selected based on measuring the embroidery pattern produced by the same embroidery machine. To emulate the interconnection between the two parallel layers, they are connected by a 10×15 conductive cylinder-array with diameter of 0.5 mm that distributed over the surfaces.

In order to model the nonuniform conductivity distribution over the surface, a similar approach as proposed in [86] is used. The embroidered conductive surface is modeled by interspersing good conductive areas that emulate the threads with lower conductivity areas to provide a model for the higher resistance paths between adjacent threads. The conductive areas that models the embroidery thread form a meander pattern aligned in the stitching direction and distributed across the surface. The high-conductivity areas are formed by a series of rectangular strips with width of 1.5mm and conductivity assigned as 4.1×10^6 S/m. The high-conductivity strips

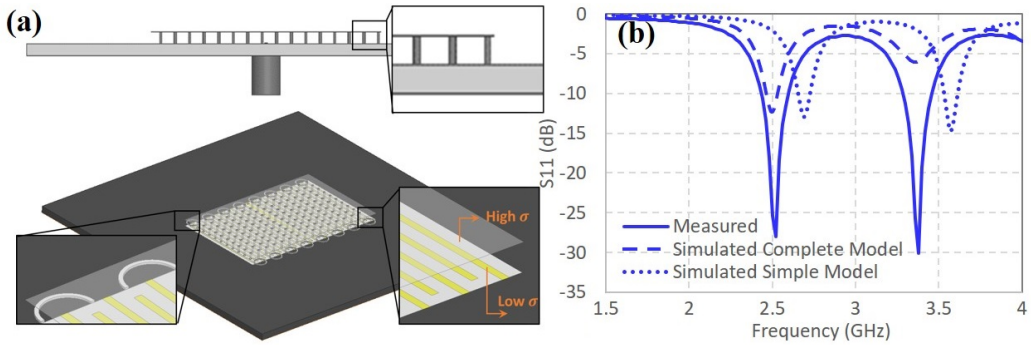

Figure 5.2: (a) A detailed full-wave model that accounts for the double-sided embroidery nature of the electro-textile patch antenna. (b) The simulation S_{11} with the complete and simple models are compared.

are connected end-to-end, while the gaps are filled by areas with low-conductivity assigned as 100 S/m.

With conductive patterns fabricated by embroidery machine, a significant amount of thread residues are observed along the edges, owing to the additional thread that the sewing machine takes when it is routed to change direction between two adjacent stitches. It is found that the thread residues that irregularly distributed along the two radiating edges of the rectangular patch affect resonant frequency to a certain extent. In order to model this effect in a simplified manner, two 8 element ring-arrays are assigned along the two radiating edges, with diameter of 3mm for each of the ring elements.

5.4 Verification by Measurements

As the final step of the study, the material characterization results and the modeling strategies are validated by prototyping embroidered textile patch antenna and conducting measurements. The embroidery pattern is sewed by the Brother SE425 embroidery machine, with dimensions of 46mm $\times$ 72mm. The prototype is fabricated by attaching the embroidered rectangular patch on top of a 3mm felt fabric

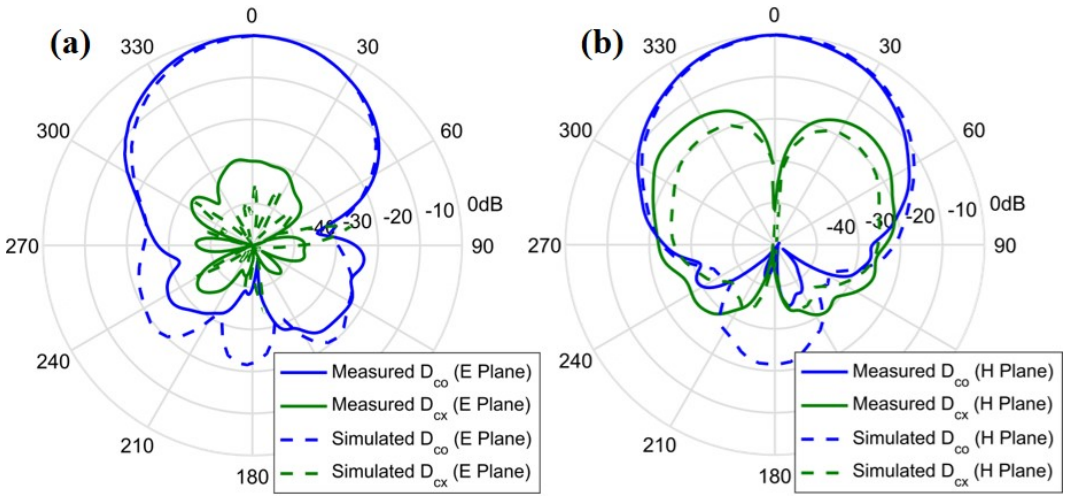

Figure 5.3: The radiation patterns in E plane and H plane of the prototyped embroidery textile patch antenna are measured in spherical near-field chamber as shown in (a) and (b), respectively.

substrate and copper foil on bottom as the ground plane. The measured S_{11} is compared with full-wave simulation in HFSS with simple model (uniform conductive surface) and complete model (with detailed discussed in Section III), as shown in Fig. 5.4 (b). It is shown that the detailed modeling strategies we propose are more effective than the simple model in terms of accurate prediction of the resonant frequencies for the first two resonant modes of embroidery patch antenna. The radiation pattern of the prototype are measured in both E and H planes in the UCLA spherical near-field chamber, and the results shown in Fig. 5.5 demonstrate good agreement between simulations and measurements for both co-pol and cross-pol radiations.

5.5 Variation of Full-Wave Modeling on Stitch Density

In order to accurately characterize the embroidery-based antenna, a detailed full-wave model is introduced in [4]. The double-sided nature of embroidery pattern is modeled by two parallel conductive layers separated by a distance of d. The

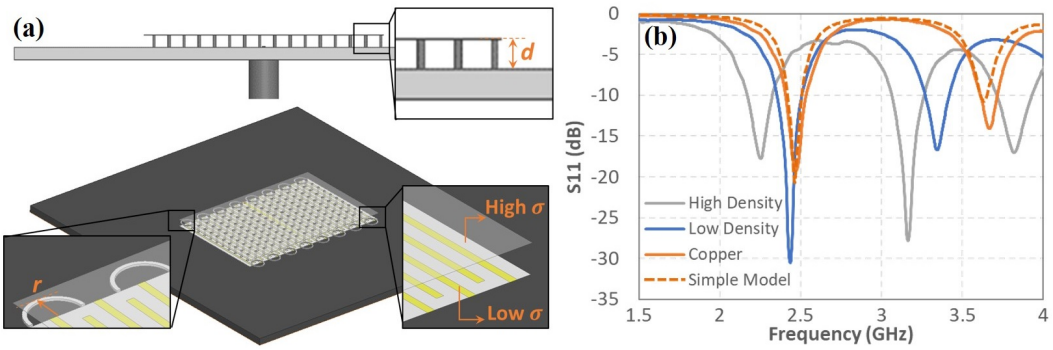

Figure 5.4: (a) A detailed full-wave model that accounts for the double-sided embroidery nature of the electro-textile patch antenna. (b) The simulation S_{11} with the complete and simple models are compared.

Table 5.1: The detailed full-wave model parameters for high and low stitch densities.

Density	Double Layer Thickness d	Thread Residue Torus r	Meander Low Conductivity σ
1250 line/m	0.5 mm	1.2 mm	50 S/m
3750 line/m	3.0 mm	3.2 mm	200 S/m

threads are aligned in a preferred direction and are not in perfect contact with each other along their full lengths. Therefore, the embroidered conductive surface is modeled by interspersing good conductive areas that emulate the threads with lower conductivity areas to provide a model for the higher resistance paths between adjacent threads. Finally, the thread residues defined by the fabrication process affect the structure on edges significantly. In order to model this effect in a simple manner, torus-arrays are assigned along the two radiating edges, with radius of r for each of the torus elements.

The stitch density of the embroidery pattern is a critical parameter in designing and fabricating electro-textile patch antennas. The effect of stitch density should be properly reflected by the detail full-wave model parameters, e.g. the double-layer thickness d, the torus radius r, and the interspersing high-low conductivities σ_h and

σ_l. Two cases of stitch densities (1250 line/m and 3750 line/m) are studied to compare the variations in full-wave modeling parameters. The prototypes with different stitch densities are fabricated, and S_{11} for each case is measured and compared with the detailed full-wave models to find the proper parameters, as listed in Tab. 5.1.

The radiation pattern of the prototypes are measured in the UCLA spherical near-field chamber. The results shown in Fig. 5.5 demonstrate good agreement between simulations and measurements for both co-pol and cross-pol radiations for antennas embroidered with low and high stitch densities.

5.6 Verification by E-Shaped Patch Antenna

As the final step of the study, an E-shaped patch antenna with low stitch density is built and tested to validate the modeling strategies and stitch density study. As shown in Fig. 5.6, the detailed full-wave modeling strategy with parameters listed in Tab. 5.1 are used to generate the simulated S_{11} results and compared to measurements. The simulations with detailed modeling shows better agreement to measurement than the result for simple model.

5.7 Conclusion

In this chapter, an accurate modeling method is presented to assist the embroidered microstrip patch antenna design. With this method, along with the electro-textile characterization method presented in Chapter 3, a systermatic and fast design and prototyping procedure is shown. In step 1, material is characterized. The effective conductivity is measured using the 4 microstrip line metod. The permittivity and loss tangent of the substrate materials is found by matching the simulation and measurement results. Be noted that the patch antenna in this step in fabricated

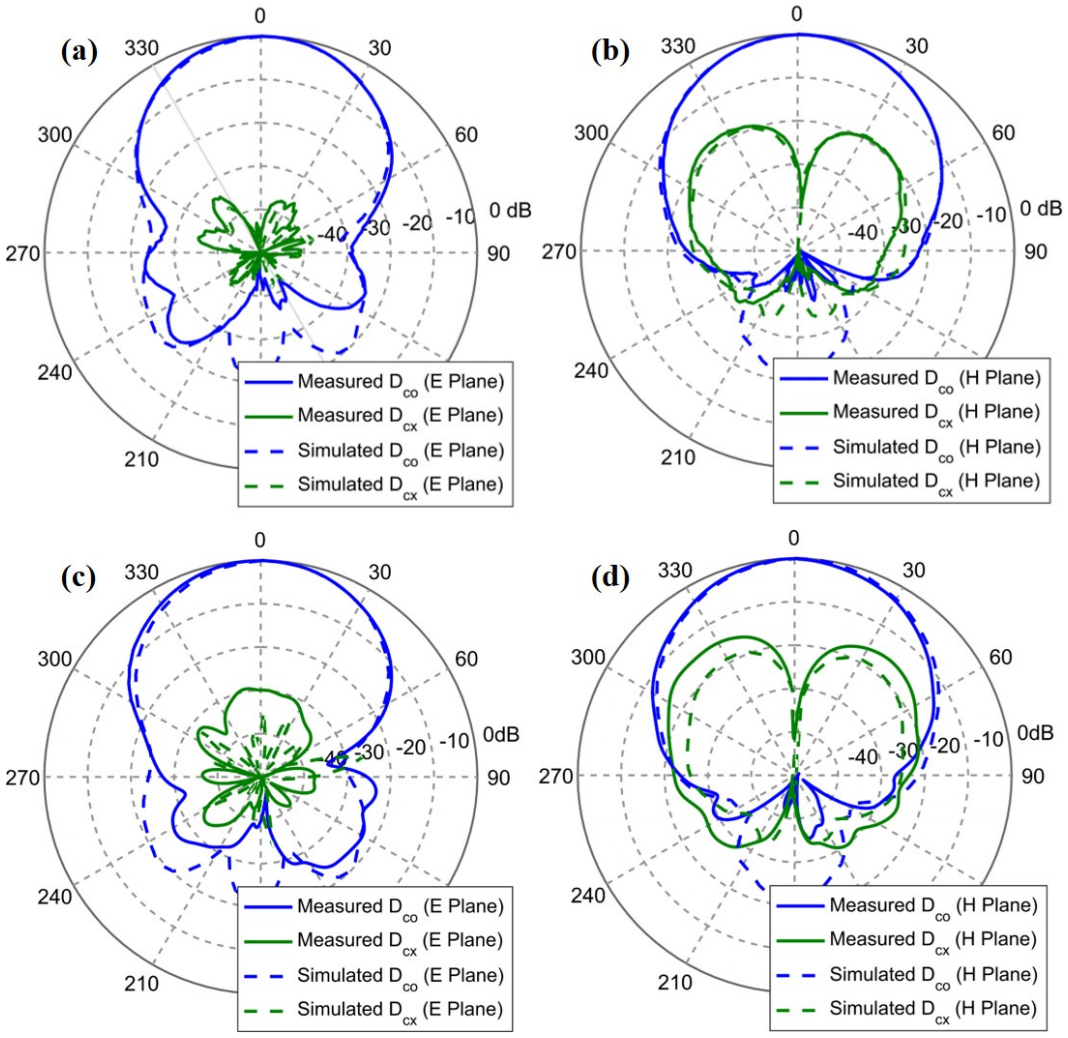

Figure 5.5: The measured radiation pattern for embroidery patch antennas with low stitch density in (a) and (b), and high stitch density in (c) and (d).

using copper sheet and flexible substrate to eliminate the effect of electro-textile pattern. In step 2, a detailed full-wave modeling is determined. 3 major aspects of the electro-textile complex structure is considered, including two parallel conductive layer, meander interspersing areas with high and low conductivities, and thread residues on the radiating edges. Be noted that the parameters of the detailed model depends on the stitching density, the conductive thread type, and stitch type. In step 3, microstrip patch antenna of different types can be designed based on the detailed

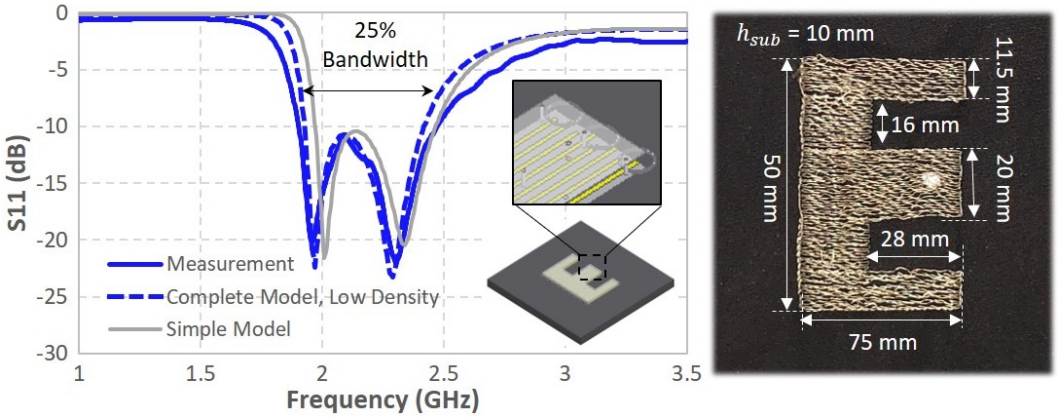

Figure 5.6: An E-shaped embroidery patch antenna with low stitch density is built and measured to validate the stitch density study.

model by step 1 and 2. For microstrip patch antennas with variations of conductive thread stitching densities, a simplified procedure can be implemented. A patch antenna can be designed using the original parameters and perform a fine tuning of the accurate model after measurement. A study on the effects of stitch density towards the accurate simulation of embroidery-based patch antennas is also presented. It is found that the patch antenna with lower density shows a closer match with patch antennas made with copper. The full wave model can be used to accurately model the performance of the patch antenna. It is further verified through the design, fabrication and measurement of embroidered E-shape patch antenna. It is noted that a circuit model to capture the characteristics of the embroidered patch antenna using Particle Swarm Optimization (PSO) is also developed but not presented here and can be found in [85]. In summary, embroidered patch antenna is accurately modeled using full-wave modeling, properly designed by using a systematic and fast design procedure, and further verified and studied through different cases.

CHAPTER 6

Conclusion

This chapter concludes the previous chapters and forecast future work. In this dissertation, electro-textiles are shown achieve high performance antenna designs in MRI and wireless communication systems at frequencies of 120 MHz - 10.6 GHz. A systematic approach is developed to guide the material selection, characterization, design, fabrication, and antenna performance measurement.

The new ultra-flexible electro-textile RF array coil shows substantial SNR advantage over a conventional coil. The SNR in cadaver images at a depth of 0.5 cm from the coil was one order of magnitude higher than a standard coil. The cadaver images showed high-quality anatomical features in the neck. As the size and number of coil elements can be modified for different anatomies of interest, this technology is not limited to neck MRI. The electro-textile material can be readily applied to more areas including pediatric, joint, and extremity MRI, and MRI-guided interventions. Future work includes the in-vivo evaluation of the new coil for different diagnostic applications.

Much emphasis is put on the discussion of its application in RF coil platform. The major contribution is summarized as follows:

(1) For the first time in the literature, flexible RF coil using electro-textile is shown to improve the SNR performance. A systematic approach is proposed starting from the design of single element RF coil using normal lithography method, followed by the design of electro-textile element and finalized by the electro-textile array.

(2) Effective method to characterize the effective conductivity of the electro-textile materials using 4 microstripline method is implemented at frequency around 120 MHz. This method dis-embed the effect of connectors and is shown to have accurate characterization of the electro-textile pattern using either embroidered conductive thread pattern and laser cut conductive cloth.

(3) A complete characterization and design procedure for electro-textile MRI RF coil is proposed and implemented. The coil element characterization can be performed using water phantom and making sure S_11 is below -15 dB at the targeted resonant frequency. Quality factor ratio measurement is used to roughly estimate the coil performance. The S_21 of the coil array is measured to show low mutual coupling between the elements. The system level characterization include SNR map, noise correlation matrix and real cadaver or human measurement. The noise correlation matrix is critical not only for SNR using conventional sequences but also critical for the image quality of the parallel imaging.

The second part of the dissertation covers electro-textile antenna designs in communications system. A novel UWB planar monopole antenna with Top-Cross-Loop (TCL) and patch antennas are discussed at 3.1 -10.6 GHz and around 2.4 GHz. Both types of the antenna starts with the characterization of the effective conductivity of the electro-textiles introduced in Chapter 3. An accurate modeling method is presented to assist the embroidered microstrip patch antenna design. With this method, a systematic and fast design and prototyping procedure is presented. In step 1, material is characterized. The effective conductivity is measured using the 4 microstrip line metod. The permittivity and loss tangent of the substrate materials is found by matching the simulation and measurement results. Be noted that the patch antenna in this step is fabricated using copper sheet and flexible substrate to eliminate the effect of electro-textile pattern. In step 2, a detailed full-wave modeling is determined. Three major aspects of the electro-textile complex structure

is considered, including two parallel conductive layer, meander interspersing areas with high and low conductivities, and thread residues on the radiating edges. It is noted that the parameters of the detailed model depend on the stitching density, the conductive thread type, and stitch type. In step 3, microstrip patch antenna of different types can be designed based on the detailed modeling in step 1 and 2. For microstrip patch antennas with variations of conductive thread stitching densities, a simplified procedure can be implemented. A patch antenna can be designed using the original parameters and perform a fine-tuning of the accurate model after measurement. A study on the effects of stitch density towards the accurate simulation of embroidery-based patch antennas is also presented. It is found that the patch antenna with lower density shows a closer match with patch antennas made with copper. The full wave model can be used to accurately model the performance of the patch antenna. It is further verified through the design, fabrication and measurement of embroidered E-shape patch antenna. It is noted that a circuit model to capture the characteristics of the embroidered patch antenna using Particle Swarm Optimization (PSO) is also developed but not presented here and can be found in [85]. In summary, embroidered patch antenna is accurately modeled using full-wave modeling, properly designed by using a systematic and fast design procedure, and further verified and studied for different patch antenna types and stitch densities.

The future work has mainly three areas:

The first part of the further increase the SNR advantage of the electro-textile RF coil using circular polarized (CP) coil design and meta-materials. The utilization of CP coil design can increase the SNR by 3 dB potentially. The use of meta-material by eliminating the noise from side of the coil thus can potentially increase SNR by 3 dB as well. This is particularly useful for knee imaging because in most case only one side of joints is of interest in the imaging. The current RF coils find it

difficult to remove the effect of the joint of the other leg because two anatomies are adjacent to each other. The use of meta-material [66] with large permeability as a reflector eliminates the noise source from one side. These two techniques combined can potentially increase the SNR by 6 dB in total.

The second aspect of the future work is focused on the application of the electro-textile RF coil platform on different anatomical structures. For different clinical applications, coil design needs to be modified and optimized. The element size, the number of coil element and the arrangements of the element needs to be changed accordingly. The electro-textile RF coil design for animal applications at lower or higher static magnetic field, in other words, at different frequencies can also be designed to tailor for specific applications.

The third part of the future work include the proposal of design curves for electro-textile patch antennas and extend the recipes to other types of antennas. It is noticed that only the planar monopole type UWB antenna and patch antennas are studied in this dissertation. It is critical to find out types of antennas suitable for electro-textile materials. With the development of more advanced electro-textile material, the limitation of the low conductivity will be minimized. The electro-textile is expected to be used in more antenna types and applications.

REFERENCES

[1] Machnet, "Carotids Coil."

[2] MAYO Foundation, "Carotid Artery Disease."

[3] S. S. Lobodzinski and M. Laks, "New material for implantable cardiac leads," *Journal of electrocardiology*, vol. 42, pp. 566–573, Nov. 2009.

[4] Z. Wang, "Electronic Textile Antennas and Radio Frequency Circuits for Body-Worn Applications," *Ph.D. Thesis*, 2014.

[5] Z. Wang, L. Z. Lee, D. Psychoudakis, and J. L. Volakis, "Embroidered Multiband Body-Worn Antenna for GSM/PCS/WLAN Communications," *IEEE Transactions on Antennas and Propagation*, vol. 62, no. 6, pp. 3321–3329, 2014.

[6] K. Koski, A. Vena, and L. Sydänheimo, "Design and implementation of electrotextile ground planes for wearable UHF RFID patch tag antennas," *IEEE Antennas and Propagation Magazine*, 2013.

[7] D. Zhang and Y. Rahmat-Samii, "Electro-textiles as potential candidate of flexible MRI RF coil for stroke prevention," in *2017 United States National Committee of URSI National Radio Science Meeting (USNC-URSI NRSM)*, pp. 1–2, IEEE, 2017.

[8] H. Lee, J. Tak, and J. Choi, "Wearable Antenna Integrated into Military Berets for Indoor/Outdoor Positioning System," *IEEE Antennas and Wireless Propagation Letters*, pp. 1–1, 2017.

[9] M. Stoppa and A. Chiolerio, "Wearable Electronics and Smart Textiles: A Critical Review," *Sensors*, vol. 14, pp. 11957–11992, July 2014.

[10] "Flexible Electronics Market Size Growth — Industry Forecast Report 2024," pp. 1–3, May 2017.

[11] K. Dhwaj, H. Lee, L. Jiang, and T. Itoh, "Transmission-line equivalent and microstrip structure for planar möbius loop resonator," in *Microwave Symposium (IMS), 2015 IEEE MTT-S International*, pp. 1–3, IEEE, 2015.

[12] K. Dhwaj, X. Li, L. J. Jiang, and T. Itoh, "Low-profile diplexing filter/antenna based on common radiating cavity with quasi-elliptic response," *IEEE Antennas and Wireless Propagation Letters*, vol. 17, no. 10, pp. 1783–1787, 2018.

[13] K. Dhwaj, L. Jiang, and T. Itoh, "Dual-band filtering antenna with novel transmission zero characteristics," *IEEE Antennas and Wireless Propagation Letters*, 2018.

[14] Y. Hu and T. S. Fisher, "Suggested standards for reporting power and energy density in supercapacitor research," *Bulletin of Materials Science*, vol. 41, p. 124, Sept. 2018.

[15] J. Budhu, Y. Rahmat-Samii, R. E. Hodges, D. C. Hofmann, D. F. Ruffatto, and K. C. Carpenter, "Three-Dimensionally Printed, Shaped, Engineered Material Inhomogeneous Lens Antennas for Next-Generation Spaceborne Weather Radar Systems," *IEEE Antennas and Wireless Propagation Letters*, vol. 17, no. 11, pp. 2080–2084.

[16] J. Budhu and Y. Rahmat-Samii, "Understanding the appearance of specular reflection in offset fed reflectarray antennas," in *2011 IEEE Antennas and Propagation Society International Symposium and USNC/URSI National Radio Science Meeting*, pp. 97–100, IEEE.

[17] J. Hong, W. Yan, Y. Ma, D. Zhang, and X. Yang, "Experimental investigation on the vibration tuning of a shell with a shape memory alloy ring," *Smart Materials and Structures*, vol. 24, p. 105007, Oct. 2015.

[18] W. Yan, K. Shaposhnikov, P. Yu, Y. Ma, and J. Hong, "Experimental Investigation and Numerical Analysis on Influence of Foundation Excitation on the Dynamics of the Rotor System," *ASME Turbo Expo 2015: Turbine Technical Conference and Exposition*, pp. V07AT30A008–V07AT30A008, June 2015.

[19] Y. Ma, Z. Liang, D. Zhang, W. Yan, and J. Hong, "Experimental Investigation on Dynamical Response of an Overhung Rotor due to Sudden Unbalance," *ASME Turbo Expo 2015: Turbine Technical Conference and Exposition*, pp. V07BT32A009–V07BT32A009, June 2015.

[20] S. Khan, L. Lorenzelli, and R. S. Dahiya, "Technologies for Printing Sensors and Electronics Over Large Flexible Substrates: A Review," *IEEE Sensors Journal*, vol. 15, no. 6, pp. 3164–3185, 2015.

[21] K. Dhwaj, L. J. Jiang, and T. Itoh, "Microstrip diplexer with low channel-frequency ratio," in *Microwave Conference (APMC), 2016 Asia-Pacific*, pp. 1–4, IEEE, 2016.

[22] K. Dhwaj, J. M. Kovitz, R. Al-Hadi, and T. Itoh, "Compact dual-band filtering antenna based on capacitor loaded patch radiator," in *Microwave Conference (APMC), 2017 IEEE Asia Pacific*, pp. 1188–1191, IEEE, 2017.

[23] J. Zhong, A. Kiourti, T. Sebastian, Y. Bayram, and J. L. Volakis, "Conformal Load-Bearing Spiral Antenna on Conductive Textile Threads," *IEEE Antennas and Wireless Propagation Letters*, vol. 16, pp. 230–233, 2017.

[24] X. Li, M. Memarian, and T. Itoh, "A New Cavity Resonance Assisted by Anisotropic Metasurfaces," *IEEE Transactions on Microwave Theory and Techniques*, vol. 66, no. 7, pp. 3224–3233.

[25] K. Dhwaj, X. Li, L. J. Jiang, and T. Itoh, "Low-Profile Diplexing Filter/Antenna Based on Common Radiating Cavity With Quasi-Elliptic Response," *IEEE Antennas and Wireless Propagation Letters*, vol. 17, no. 10, pp. 1783–1787.

[26] X. Li, K. Dhwaj, and T. Itoh, "Single-Layer Slow-Wave Substrate Integrated Waveguide with Enhanced Capacitance," in *2018 IEEE/MTT-S International Microwave Symposium - IMS 2018*, pp. 316–318, IEEE.

[27] X. Li, M. Memarian, and T. Itoh, "A new resonance in a circular waveguide cavity assisted by anisotropic metasurfaces," in *2017 IEEE/MTT-S International Microwave Symposium - IMS 2017*, pp. 1801–1803, IEEE.

[28] K. Koski and L. Sydänheimo, "Fundamental characteristics of electro-textiles in wearable UHF RFID patch antennas for body-centric sensing systems," *IEEE Transactions on Antennas and Propagation*, vol. 62, no. 12, pp. 6454–6462, 2014.

[29] A. Kiourti, C. Lee, and J. L. Volakis, "Fabrication of Textile Antennas and Circuits With 0.1 mm Precision," *IEEE Antennas and Wireless Propagation Letters*, vol. 15, pp. 151–153, 2016.

[30] K. Dhwaj, J. Kovitz, H. Tian, L. Jiang, and T. Itoh, "Half-mode cavity based planar filtering antenna with controllable transmission zeroes," *IEEE Antennas and Wireless Propagation Letters*, 2018.

[31] K. Dhwaj, H. Tian, and T. Itoh, "Low-profile dual-band filtering antenna using common planar cavity," *IEEE Antennas and Wireless Propagation Letters*, pp. 1–1, 2018.

[32] K. Dhwaj, X. Li, Z. Shen, and S. Qin, "Cavity Resonators Do the Trick: A Packaged Substrate Integrated Waveguide, Dual-Band Filter," *IEEE Microwave Magazine*, vol. 17, no. 1, pp. 58–64.

[33] X. Li, H. Lee, T. I. M. C. APMC, . Asia, and 2015, "Studies of realizing low side lobe levels of composite right/left-handed SIW leaky-wave antennas - IEEE Conference Publication," *ieeexplore.ieee.org*.

[34] Y. Y. Wenzhong Yan, Angela L. Gao, A. Mehta, and 2018, "Towards Autonomous Printable Robotics: Design and Prototyping of the Mechanical Logic," *International Symposium on Experimental Robotics (ISER)*.

[35] K. Dhwaj, S. Qin, L. J. Jiang, and T. Itoh, "Tunable transmission zeroes bandpass filter with external quality factor control," in *Microwave Conference (APMC), 2016 Asia-Pacific*, pp. 1–4, IEEE, 2016.

[36] Y. Ouyang and W. J. Chappell, "High frequency properties of electro-textiles for wearable antenna applications," *IEEE Transactions on Antennas and Propagation*, vol. 56, no. 2, pp. 381–389, 2008.

[37] A. Mehdipour, A.-R. Sebak, C. W. Trueman, I. D. Rosca, and S. V. Hoa, "Reinforced Continuous Carbon-Fiber Composites Using Multi-Wall Carbon Nanotubes for Wideband Antenna Applications," *IEEE Transactions on Antennas and Propagation*, vol. 58, no. 7, pp. 2451–2456, 2010.

[38] Y. Li, R. Torah, S. Beeby, and J. Tudor, "An all-inkjet printed flexible capacitor on a textile using a new poly(4-vinylphenol) dielectric ink for wearable applications," in *2012 IEEE Sensors*, pp. 1–4, IEEE, 2012.

[39] W. G. Whittow, A. Chauraya, J. C. Vardaxoglou, Y. Li, R. Torah, K. Yang, S. Beeby, and J. Tudor, "Inkjet-Printed Microstrip Patch Antennas Realized on Textile for Wearable Applications," *IEEE Antennas and Wireless Propagation Letters*, vol. 13, pp. 71–74, 2014.

[40] J. A. Malko, E. C. McClees, I. F. Braun, P. C. Davis, and J. C. Hoffman, "A flexible mercury-filled surface coil for MR imaging.," *American Journal of Neuroradiology*, vol. 7, pp. 246–247, Mar. 1986.

[41] J. R. Corea, A. M. Flynn, B. Lechêne, G. Scott, G. D. Reed, P. J. Shin, M. Lustig, and A. C. Arias, "Screen-printed flexible MRI receive coils," *Nature Communications*, vol. 7, pp. 10839–11, Mar. 2016.

[42] D. Mager, A. Peter, L. Del Tin, and E. Fischer, "An MRI receiver coil produced by inkjet printing directly on to a flexible substrate," *IEEE Transactions on Medical Imaging*, 2010.

[43] K. P. Pruessmann, M. Wyss, A. Manoliu, J. Hodler, G. Andreisek, and N. Mamisch-Saupe, "MR imaging of healthy knees in varying degrees of flexion using a stretchable coil array provides comparable image quality compared to a standard knee coil array," *European Journal of Radiology*, vol. 85, pp. 518–523, Mar. 2016.

[44] M. Klemm and G. Troester, "Textile UWB antennas for wireless body area networks," *IEEE Transactions on Antennas and ...*, 2006.

[45] Z. Wang, K. Karathanasis, and J. L. Volakis, "Axial ratio reduced ultra wideband slot spiral on hybrid impedance surfaces," *Journal of Electromagnetic Waves and Applications*, Feb. 2015.

[46] T. Castel, S. Lemey, P. Van Torre, C. Oestges, and H. Rogier, "Four-Element Ultrawideband Textile Cross Array for Dual-Spatial and Dual-Polarization Diversity," *IEEE Antennas and Wireless Propagation Letters*, vol. 16, pp. 481–484, 2017.

[47] R. B. V. B. Simorangkir, Y. Yang, L. Matekovits, and K. P. Esselle, "Dual-Band Dual-Mode Textile Antenna on PDMS Substrate for Body-Centric Communications," *IEEE Antennas and Wireless Propagation Letters*, vol. 16, pp. 677–680, 2016.

[48] F.-X. Liu, Z. Xu, D. C. Ranasinghe, and C. Fumeaux, "Textile Folded Half-Mode Substrate-Integrated Cavity Antenna," *IEEE Antennas and Wireless Propagation Letters*, vol. 15, pp. 1693–1697, 2016.

[49] D. G. Nishimura, *Principles of magnetic resonance imaging* . Electrical Engineering Department, Stanford University: Stanford University, 1.1 ed., 2010.

[50] Z.-P. Liang and P. C. Lauterbur, *Principles of Magnetic Resonance Imaging: A Signal Processing Perspective*. Wiley-IEEE Press, 2000.

[51] J. M. Jin, "Electromagnetics in magnetic resonance imaging," *IEEE Antennas and Propagation Magazine*, vol. 40, no. 6, pp. 7–22, 1998.

[52] J. Jin, *Electromagnetic Analysis and Design in Magnetic Resonance Imaging*. Department of Electrical and Computer Engineering, University of Illinois at Urbana-Champaign Urbana, Illinois: CRC Press, 1998.

[53] M. R. Bendall, *Surface coil technology*. Magnetic Resonance Imaging, 1988.

[54] P. B. Roemer, W. A. Edelstein, C. E. Hayes, S. P. Souza, and O. M. Mueller, "The NMR phased array," *Magnetic Resonance in Medicine*, vol. 16, pp. 192–225, Nov. 1990.

[55] W. A. Edelstein, G. H. Glover, C. J. Hardy, and R. W. Redington, "The intrinsic signal-to-noise ratio in NMR imaging," *Magnetic Resonance in Medicine*, vol. 3, pp. 604–618, Aug. 1986.

[56] J. R. Corea, P. B. Lechene, M. Lustig, and A. C. Arias, "Materials and methods for higher performance screen-printed flexible MRI receive coils," *Magnetic Resonance in Medicine*, vol. 16, pp. 1–9, Sept. 2016.

[57] A. H. Association, "Impact of Stroke," 2005.

[58] "Carotid Artery Disease and Stroke."

[59] C. Yuan, M. Oikawa, Z. Miller, and T. Hatsukami, "MRI of carotid atherosclerosis," *Journal of Nuclear Cardiology*, vol. 15, pp. 266–275, Mar. 2008.

[60] D. Zhang and Y. Rahmat-Samii, "An ergonomie design for 3Tesla MRI neck coil," in *2016 IEEE International Symposium on Antennas and Propagation & USNC/URSI National Radio Science Meeting*, pp. 463–464, IEEE, 2016.

[61] S. A. Materials, "Liberator 40, Syscom Advanced Material," Apr. 2017.

[62] R. K. Shawl, B. R. Longj, and D. H. Werner, "The characterization of conductive textile materials intended for radio frequency applications," *IEEE Antennas and Propagation Magazine*, vol. 49, no. 3, pp. 28–40, 2007.

[63] R. E. Collin, "Foundations for microwave engineering," 2007.

[64] S. P. Morgan Jr., "Effect of Surface Roughness on Eddy Current Losses at Microwave Frequencies," *Journal of applied physics*, vol. 20, pp. 352–362, Apr. 1949.

[65] M. V. Lukic and D. S. Filipovic, "Modeling of 3-D Surface Roughness Effects With Application to u-Coaxial Lines," *IEEE Transactions on Microwave Theory and Techniques*, vol. 55, no. 3, pp. 518–525, 2007.

[66] O. Dietrich, J. G. Raya, S. B. Reeder, M. F. Reiser, and S. O. Schoenberg, "Measurement of signal-to-noise ratios in MR images: Influence of multichannel coils, parallel imaging, and reconstruction filters," *Journal of Magnetic Resonance Imaging*, vol. 26, pp. 375–385, Aug. 2007.

[67] T. Zwick, W. Wiesbeck, J. Timmermann, and G. Adamiuk, Ultra-wideband RF System Engineering. Cambridge University Press.

[68] P. A. Catherwood and W. G. Scanlon, "Ultrawideband Communications—An Idea Whose Time has Still Yet to Come? [Wireless Corner]," *IEEE Antennas and Propagation Magazine*, vol. 57, no. 2, pp. 38–43, 2015.

[69] S. Wood and R. Aiello, *Essentials of UWB*. Cambridge: Cambridge University Press, 2009.

[70] Alereon, "UWB Applications in Military."

[71] J. M. Johnson and Y. Rahmat-Samii, "The tab monopole," *IEEE Transactions on Antennas and Propagation*, vol. 45, no. 1, pp. 187–188, 1997.

[72] M. Koohestani, J. F. Zurcher, A. A. Moreira, and A. K. Skrivervik, "A Novel, Low-Profile, Vertically-Polarized UWB Antenna for WBAN," *IEEE Transactions on Antennas and Propagation*, vol. 62, no. 4, pp. 1888–1894, 2014.

[73] M. Hedayati, M. J. Kazemi, R. S. R. Microwave, , and 2011, "Design and implementation of a multi triangular microstrip resonator passband filter based on mixed coupling - IEEE Conference Publication," *ieeexplore.ieee.org*.

[74] G. Askari, M. Kamarei, and M. Hedayati, "UWB sixport aanalysis and design in mm-wave for 5G applications," in *2017 Progress In Electromagnetics Research Symposium - Spring (PIERS)*, pp. 1190–1194, IEEE.

[75] A. B. Yakovlev, M. Hedayati, M. G. Silveirinha, and G. W. Hanson, "Local thickness-dependent permittivity model for nonlocal bounded wire-medium structures," *Physical Review B*, vol. 94, p. 155442, Oct. 2016.

[76] K. Bahadori and Y. Rahmat-Samii, "A Miniaturized Elliptic-Card UWB Antenna With WLAN Band Rejection for Wireless Communications," *IEEE Transactions on Antennas and Propagation*, vol. 55, no. 11, pp. 3326–3332, 2007.

[77] F. M. Tanyer-Tigrek, D. P. Tran, I. E. Lager, and L. P. Ligthart, "Wideband tulip-loop antenna," in *2009 3rd European Conference on Antennas and Propagation*, pp. 1446–1449, IEEE, 2009.

[78] F. M. Tanyer-Tigrek, I. E. Lager, and L. P. Ligthart, "A CPW-Fed Printed Loop Antenna for Ultra-Wideband Applications, and its Linear-Array Performance," *IEEE Antennas and Propagation Magazine*, vol. 52, no. 4, pp. 31–40, 2010.

[79] T. Zwick and W. Wiesbeck, "Ultra-wideband RF System Engineering," 2013.

[80] emerson, "SMA 50, end launch Jack receptacle round contact," tech. rep.

[81] "System Fidelity Factor: A New Method for Comparing UWB Antennas," *IEEE Transactions on Antennas and Propagation*, vol. 59, no. 7, pp. 2502–2512, 2011.

[82] N. Pires, A. A. Moreira, A. K. Skrivervik, and M. Koohestani, "Time-domain performance of patch-loaded band-reject UWB antenna," *Electronics Letters*, vol. 49, pp. 385–386, Mar. 2013.

[83] H. Sheng, P. Orlik, A. M. Haimovich, L. J. Cimini, and J. Zhang, "On the spectral and power requirements for ultra-wideband transmission," in *IEEE International Conference on Communications*, pp. 738–742, IEEE.

[84] F. Declercq, I. Couckuyt, H. Rogier, and T. Dhaene, "Environmental High Frequency Characterization of Fabrics Based on a Novel Surrogate Modelling Antenna Technique," *IEEE Transactions on Antennas and Propagation*, vol. 61, pp. 5200–5213, Sept. 2013.

[85] D. Zhang and Y. Rahmat-Samii, "Integration of electro-textile RF coil array with magnetic resonance imaging (MRI) system: Design strategies and characterization methods," in *2018 International Workshop on Antenna Technology (iWAT)*, pp. 1–3, IEEE.

[86] T. Dias, S. Zhang, T. Acti, R. Seager, Y. Vardaxoglou, W. Whittow, and A. Chauraya, "Effect of the fabrication parameters on the performance of embroidered antennas," *IET Microwaves, Antennas {& Propagation*, vol. 7, pp. 1174–1181, Nov. 2013.